Single molecule spectroscopic studies of acid-base bifunctional thin-film catalysts

by

Abdulhafiz Onimisi Usman

B.Eng., Ahmadu Bello University, 2012
M.Sc., King Fahd University of Petroleum and Minerals, 2017

AN ABSTRACT OF A DISSERTATION

submitted in partial fulfillment of the requirements for the degree

DOCTOR OF PHILOSOPHY

Tim Taylor Department of Chemical Engineering
Carl R. Ice College of Engineering

KANSAS STATE UNIVERSITY
Manhattan, Kansas

2022

Abstract

This dissertation describes the use of single molecule spectroscopy to study the distribution of active sites on silica-supported cesium catalysts and amine-functionalized silica films with acid-base gradients. These catalysts are important for the common C-C coupling aldol condensation reactions. This work also demonstrates the use of single molecule (SM) methods to study the relationship between the distribution of acidity on catalytic surfaces and chemical reactivity. In the first project, a dual-color ratiometric SM method was used to study the acidity distributions on Mg-Zr-Cs/SiO_2 catalyst films with different cesium loading using C-SNARF-1 as a pH-sensitive probe. The dye was found to be an effective indicator of local activity between pH 3 and pH 6.2. Single molecule emission data were collected from the catalyst films as a function of cesium content for films ranging from 0 to 20% cesium. The histograms of the emission ratios obtained for each film revealed a broad distribution of acidic properties particularly on films with high cesium loading. In the second project, a gradient silica film incorporating an amine gradient was synthesized. The formation and composition of the amine gradients were verified using spectroscopic ellipsometry, water contact angle, and XPS measurements. SM methods were used to probe the local acidity distribution on these gradients. Nile Red, typically used as a solvatochromic probe, was used to detect changes in the acid-base properties of the films. The single molecule data revealed a broad bimodal distribution of Nile Red spectra that varied along the gradient. This study provided data relevant to the use of aminosilane-modified silica catalysts in bifunctional cooperative chemical catalysis. In the final project, the SM study of the aldol condensation of Nile Red dye incorporating an aldehyde moiety with silica-bound acetophenone was introduced. The reactions were carried out on different sections of a bifunctional gradient film and the preliminary results show a link between activity distribution and chemical reactivity.

Single-molecule spectroscopic studies of acid-base bifunctional thin-film catalysts

by

Abdulhafiz Onimisi Usman

B.Eng., Ahmadu Bello University, 2012
M.Sc., King Fahd University of Petroleum and Minerals, 2017

A DISSERTATION

submitted in partial fulfillment of the requirements for the degree

DOCTOR OF PHILOSOPHY

Tim Taylor Department of Chemical Engineering
Carl R. Ice College of Engineering

KANSAS STATE UNIVERSITY
Manhattan, Kansas

2022

Approved by:

Co-Major Professor
Dr. Keith L. Hohn

Approved by:

Co-Major Professor
Dr. Daniel A. Higgins

Copyright

Abstract

This dissertation describes the use of single molecule spectroscopy to study the distribution of active sites on silica-supported cesium catalysts and amine-functionalized silica films with acid-base gradients. These catalysts are important for the common C-C coupling aldol condensation reactions. This work also demonstrates the use of single molecule (SM) methods to study the relationship between the distribution of acidity on catalytic surfaces and chemical reactivity. In the first project, a dual-color ratiometric SM method was used to study the acidity distributions on Mg-Zr-Cs/SiO_2 catalyst films with different cesium loading using C-SNARF-1 as a pH-sensitive probe. The dye was found to be an effective indicator of local acidity between pH 3 and pH 6.2. Single molecule emission data were collected from the catalyst films as a function of cesium content for films ranging from 0 to 20% cesium. The histograms of the emission ratios obtained for each film revealed a broad distribution of acidic properties particularly on films with high cesium loading. In the second project, a gradient silica film incorporating an amine gradient was synthesized. The formation and composition of the amine gradients were verified using spectroscopic ellipsometry, water contact angle, and XPS measurements. SM methods were used to probe the local acidity distribution on these gradients. Nile Red, typically used as a solvatochromic probe, was used to detect changes in the acid-base properties of the films. The single molecule data revealed a broad bimodal distribution of Nile Red spectra that varied along the gradient. This study provided data relevant to the use of aminosilane-modified silica catalysts in bifunctional cooperative chemical catalysis. In the final project, the SM study of the aldol condensation of Nile Red dye incorporating an aldehyde moiety with silica-bound acetophenone was introduced. The reactions were carried out on different sections of a bifunctional gradient film and the preliminary results show a link between acidity distribution and chemical reactivity.

Table of Contents

List of Figures

List of Acronyms and Definitions

AFM	Atomic force microscopy
APTMOS	(3-Aminopropyl)trimethoxysilane
ATR	Attenuated Total Reflection
BE	Binding Energy
CCD	Charge-coupled device
C-SNARF-1	2(or 4)-[10-(dimethylamino)-3-oxo-3H-benzo[c]xanthene-7-yl]
DCLP	Dichroic long pass filter
FCC	Fluid catalytic cracking
FTIR	Fourier-transform infrared spectroscopy
IWDC	Infusion-withdrawal dip coating
NA	Numerical aperture
NASCA	Nanometer Accuracy by Stochastic Chemical reActions microscopy
NR	Nile Red
PALM	Photoactivated localization microscopy
PDMS	Polydimethylsiloxane
PEG	Polyethylene glycol
PSF	Point spread function
PTMOS	Phenyltrimethoxysilane

PVD	Physical vapor deposition
SBA-15	Santa Barbara Amorphous-15
SEM	Scanning electron microscopy
SM	Single molecule
SMFS	Single molecule fluorescence spectroscopy
TEM	Transmission electron microscopy
TEOS	Tetraethyl orthosilicate
TIRF	Total Internal Reflection Fluorescence
TMOS	Tetramethyl orthosilicate
TPD	Temperature-programmed desorption
WCA	Water contact angle
XPS	X-ray photoelectron spectroscopy
XRD	X-ray diffraction

Acknowledgements

I would like to express my gratitude to my major professor and research advisor Dr.Keith Hohn for his constant guidance and support throughout my studies at Kansas State University. He helped me become a more competent and independent researcher.

I would like to thank my co-major professor, Dr. Daniel Higgins, for his guidance and direction throughout my Ph.D. He introduced me to fluorescence spectroscopic methods and patiently guided me on data collection and analysis.

I am deeply grateful to Dr. Placidus Amama for being my mentor and for providing feedback and suggestions on my research I highly appreciated the critical corrections and recommendations given by Dr. John Schlup as part of my dissertation committee.

I acknowledge the help of former and current members of Dr. Hohn's, Dr. Higgins' and Dr. Takashi Ito's research groups including Dr. Leonardo Garro-Mena, Dr. Judith Bautista, Dr. Herman Coceancigh, and Hamid Rashidi. They made my stay in Manhattan much better and patiently explained new concepts to me.

I am grateful to the faculty and staff of the chemical engineering department at Kansas State University for welcoming me, giving me an excellent education, and being supportive throughout my stay. I thank David Threewit and Jim Hodgson for helping me with the laboratory equipment and making the glass flasks and tubes used in this work.

I gratefully acknowledge the support of the US National Science Foundation for the financial support that made possible all the research work I have done.

Finally, I would like to thank all my friends and family for being supportive, encouraging, and patient with me during this chapter of my life.

Dedication

This work is dedicated to my loving parents Usman A. Umar and Mariam F. Ahmed.

Chapter 1 - General Introduction

1.1 Biomass Processing

The US Department of Energy (DOE) and US Department of Agriculture (USDA) estimated that 365 million dry tons of biomass, produced at $60 per ton, were used in the US in 2017. This is projected to increase to about 1.2 billion tons per year in 2050, enough to produce 21 billion gallons of advanced biofuels each year at a projected biomass cost of $80 per ton. This can potentially replace 30% of current petrol consumption in the US. To achieve this milestone, it is necessary to increase the research in biofuels and bio co-products production.[1–3]

The chemical processing of biomass is an attractive option for producing biofuels because the lignocellulosic biomass feedstock is mostly available as waste or a non-food crop.[4–7] Biomass can be converted to sugars by acid hydrolysis. These sugars can be dehydrated to yield furanic compounds. Aldol condensation of these furanic compounds with other ketones or themselves leads to the formation of C_{13}-C_{15} adducts that yield diesel fuels upon hydrogenation and/or hydrodeoxygenation.[6,8–10] These reactions are mostly catalyzed using base catalysts[8] such as alkali oxides and hydrotalcites,[6] or bifunctional catalysts incorporating both basic and acidic sites. The acidic and basic functional groups act cooperatively to increase the rate of the aldol reactions.[11] Understanding the different ways of interaction between the two groups is key to designing better catalysts, and this has prompted more study.

1.2 The aldol condensation reaction

Aldol condensation is the formation of α, β unsaturated compounds by the reaction of enolates of carbonyl compounds with aldehydes or ketones. These reactions can be carried out in the vapor phase or organic liquid phases. An aldol condensation reaction can be catalyzed by both acids and bases, with basic catalysts being the more common choice.[4] Carbonyl compounds can

act as both electrophiles and nucleophiles in the reactions, and one of the compounds must have an α-hydrogen for aldol condensation to occur.

The mechanism of the self-aldol condensation of acetone over a base is shown in Figure 1.1. The first step involves the abstraction of a proton from the alpha carbon of one of the acetone molecules by a base to form a carbonium intermediate followed by a C-C bond formation, then a proton equilibration. The final steps of hydroxide elimination and C=C bond formation are preceded by a second enolization step. [12]

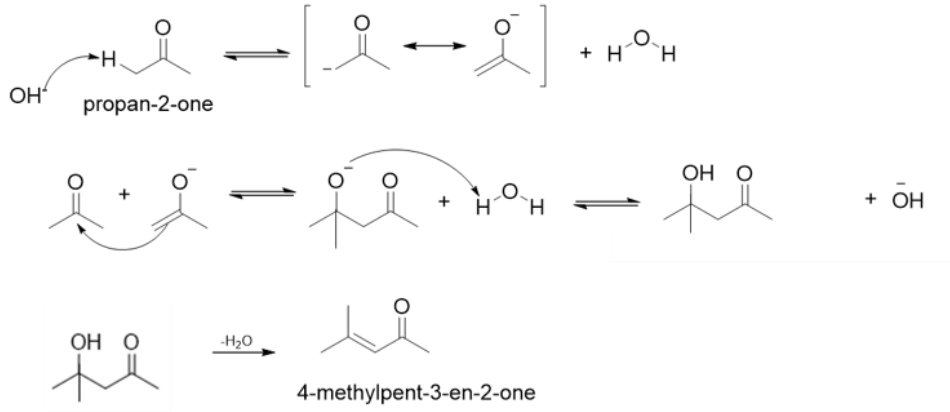

Figure 1.1 Base-catalyzed self-condensation of acetone

The mechanism of the self-aldol condensation of acetone over an acidic catalyst is shown in Figure 1.2. First, there is an acid-catalyzed formation of an enol followed by the attack of the protonated carbonyl group of the other acetone molecule by the enol. In the final step, there is proton transfer and dehydration to form the product.[13]

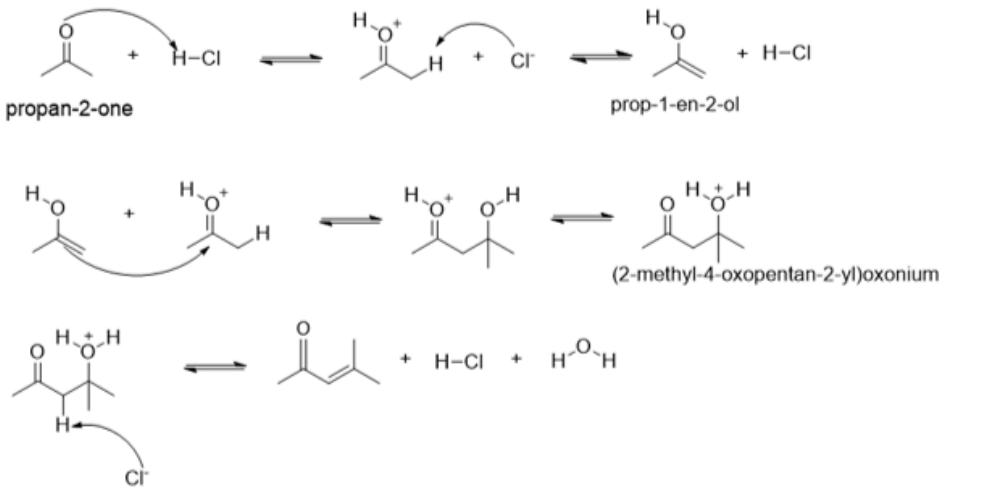

Figure 1.2 Acid-catalyzed self-condensation of acetone

1.3 Bulk basic and acid-base bifunctional catalysts for aldol condensation reactions

Mixed-oxide catalysts have been used extensively for the aldol condensation reactions in biomass processing. The aldol condensation of furfural with acetone has been catalyzed using mixed oxide catalysts such as Mg/Zr,[7,9,14] Al-Mg, Ca-Zr,[7] and, Mg-Zr mixed oxide catalysts combined with carbon nanofibers and high surface area graphite.[14]

Another category of catalysts used for aldol condensation reactions is silica-supported catalysts, where the large BET surface area and pore sizes contribute to their high activity and thermal stability.[15] The condensation of methyl propionate with formaldehyde catalyzed by Zr-Fe-Cs/SBA-15[16] and La-Cs/SBA-15[17] has been widely studied[16,17]. Here, cesium is the major source of the basic character of the catalysts, and its loading determines the catalytic activity.[18] Similar experiments have been successfully carried out using microporous silica as the catalyst support[16]. The activities of these basic catalysts for aldol condensation reactions and their selectivity to the

α, β-unsaturated products were shown to be highly dependent on the number of medium-strength basic sites present. Cesium dopings between 11-15 wt.% were also found to be optimal for the majority of the aldol condensation reactions reported.[16–18]

Cooperative catalysis using acid-base bifunctional catalysts can increase the product yields of coupling reactions such as aldol condensation and Knoevenagel reactions.[16,19–22] When a catalyst with both acidic and basic sites is used, the functional groups can each activate the two carbonyl compounds separately increasing the reactivity of both, or they can sequentially activate one of the carbonyl compounds, increasing its reactivity.[11,19,23] Mesoporous silica catalysts incorporating acidic and basic organic functional groups are among the most common acid-base catalysts used to study cooperative catalysis. The aldol condensation of 4-nitrobenzaldehyde with acetone catalyzed by mesoporous silica containing carboxylic acid and amine functional groups produced more of the addition and condensation products than when mesoporous catalysts containing only either the carboxylic or amine functional groups were used, and when their individual rates were combined.[19] In another study of the same reaction, acidic functional groups of different strengths were immobilized on a silica surface with amine groups,[23] and the catalytic activities were found to decrease with increasing acidic strength of the functional groups.[19,23]

Silanols, which can act as Bronsted acids, also provide acidic character in a catalyst for an aldol condensation when they are spatially separated from amine groups on amine-functionalized silica catalysts.[24] A common reaction mechanism suggests that reaction rates increase because the basic groups activate the ketone by the formation of an enamine while the acidic groups activate the aldehyde.[24]

Studies have confirmed that these bifunctional catalysts work best when weak acids are paired with primary amines.[24] Weak acids are better because when they are immobilized on

surfaces together with bases, there is an equilibrium that lies in the direction of free acid and base sites, rather than neutralized ion pairs seen in strong acid-base catalysts.[23] The cooperativity of amines and silanols in aldol condensation reactions also depends on the linker length of the aminosilane.[25]

Hydrotalcites are another common class of basic catalysts employed for aldol condensation reactions. Hydrated hydrotalcites have been used for the condensation of benzaldehyde with acetone,[26] the self-condensation of acetone,[22] and the condensation of citral with acetone.[26] Roelofs et al.[22] suggested that the disorganization of the layered structure of the hydrotalcites due to hydration increases the basic strength of some of the sites which increases its overall activity for condensation reactions.[26]

1.4 Chemical Gradients

Gradient films are surfaces with gradually changing chemical properties. This change in chemical property induces a gradual change in a measurable physical quantity.[27–30] In broad terms, gradients can be made using a bottom-up approach (by attaching a thin film to a surface in a progressive manner) or top-down (by gradually modifying the topmost surface layer of a substrate).[28] Gradient catalyst films enable high-throughput and combinatorial experiments. Combinatorial experiments are important because we can check rapidly the influence of film thickness or functional groups on the material properties. It saves time, conserves material, and reduces sample-to-sample variation.[31,32] They can also help to mimic and understand naturally occurring gradients.

Some of the techniques used to deposit chemical gradients include diffusion, printing (contact and inkjet), desorption, advancing solution by controlling reaction time, irradiation, and physically controlled polymerization.[27,28] Microcontact printing was used to create gradients of

perfluorinated thiols and hexadecanethiols on a gold-coated silicon wafer in a study.[33] They confirmed the deposition of a gradient with gradually changing surface energy using ellipsometry, water contact angle, and XPS mapping.[33] Khire and coworkers[34] created chemical gradients using directional vapor phase deposition by placing a solution of decyltrichlorosilane in mineral oil next to a surface functionalized with a thiol-terminated self-assembled monolayer (SAM). Silane molecules diffused across the base layer to form a concentration gradient that was replicated on the surface.[34] Other reported methods for synthesizing gradient films include the deposition of poly(ethylene)glycol (PEG) surface gradients by using a gel-diffusion method,[35] the formation of plasma polymer vertical gradients using plasma deposition methods in a plasma reactor,[36] and the deposition of aminosilane chemical gradients on a silicon wafer using controlled-rate infusion (CRI) to create chemical gradients on silicon wafers using aminosilanes.[37]

1.5 Single Molecule Fluorescence Spectroscopy (SMFS)

The detection of single enzymes by spectroscopic methods was discovered in the 1960s[38] and the technique has since been used to detect single molecules in various media by the application of various microscopic approaches including near-field optical scanning microscopy (NSOM), confocal, total internal reflection fluorescence (TIRF) and wide-field epifluorescence microscopies.[39–43] Generally, for successful detection of single molecules, small excitation volumes and substrates/solvents incorporating minimal fluorescent impurities are used.[41,43,44] Single molecule measurements can be used to study chemical reactivity, dynamics, DNA conformation, enzyme kinetics, and heterogeneous catalysis and nanocrystals,[40,44] and they can help correlate experimental observation and theory.[41]

Fluorescent probes or dyes are commonly used as indicators in single molecule experiments. The selection of the right probe is the most important factor to obtain quality

information from single molecule studies. Some common types of probes include solvatochromic, pH, rigidochromic, and anisotropy probes.[45,46] These probes can either be loaded during the sol-gel synthesis of materials, or they can be loaded onto the material after its synthesis. Fluorescent molecules can have many interactions with their local environment such as protonation and tautomerization. Fluorescent probes can give information on the surface chemistry of silica-based materials, polarity and apparent pH of various microenvironments, catalyst homogeneity, and the accessibility of the catalyst active sites to reactants.[44,45]

The Higgins group has conducted numerous studies for probing the microenvironments of thin films using single molecule methods.[47] Thin silica films with macroscopic polarity gradients created by using an infusion-withdrawal dip-coating method have been characterized using fluorescence spectroscopy studies.[48] They demonstrated that the thin film environments of organically modified silicate films prepared using different precursor materials and methods were markedly different.[49] In one of their papers, they characterized the distribution of acid sites in thin films of aluminosilicate solid catalysts with C-SNARF-1 as the probe.[50] C-SNARF-1 was also used to study the local microenvironment of mesoporous Al-Si systems at very low pH using the dual-color single molecule method. The dye was found to be an effective pH probe between pH 1 and 5, and the single molecule results showed that the acidity of aluminosilicate films increased with increasing alumina content.[50]

1.6 Single molecule fluorescence spectroscopy for catalysis

The activity of a heterogeneous catalyst is largely dependent on its nanoscale composition. Hence, rather than correlate the performance of catalysts with the bulk properties such as total acidity or basicity, it would be better to study the composition of catalysts at the nanoscale and correlate this to the activity of local sites.[51–53] This technique has been used to follow the progress

of reactions and to measure the catalytic turnover frequencies of individual sites. This was found to be useful in distinguishing the sites responsible for catalyst deactivation from active sites.[54–56] Single-molecule methods have good spatial and temporal resolutions, sufficient to probe single molecule sites. This method can achieve nanometer spatial resolutions and milli-microseconds temporal resolutions[12,50]

Single-molecule spectroscopic studies of single active sites can be carried out by using strongly fluorescent probe molecules or fluorogenic reactions.[57] For instance, ratiometric dyes such as (5′ and 6′)-carboxy-10-(dimethylamino)-3-hydroxyspiro[7H-benzo[c]xanthene-7,1′(3H)-isobenzofuran]-3′-one (C.SNARF-1) and fluorescein show a change in their fluorescence emission properties in the presence of H^+ ions and have been employed to study the Bronsted acidobasicity distributions of heterogeneous catalysts.[58]

Numerous studies demonstrating the use of single molecule methods in heterogeneous catalysis have been reported.[53,57,59–62] For instance, the redox catalysis of gold nanoparticles in solution was investigated by reducing non-fluorescent resazurin to fluorescent resorufin by NH_2O.[52] The analysis of the single molecule results from this reaction, which was carried out using a wide-field microscope, revealed three distinct catalytic steps in the reaction and enabled the calculation of the reaction rate constants.[52] By using a dual-dye staining technique, Weckhuysen, et al., developed a Bronsted acidity map for fluid catalytic cracking (FCC) zeolite catalysts used to catalyze the oligomerization of thiophenes.[63] The same group also studied the reactivity of the various FCC catalysts for a fluorogenic liquid phase styrene oligomerization reaction carried out using a confocal microscope, revealing new insights into the relationship between acidity and severity of catalyst deactivation.[64] Decan et al. in 2014,[65] studied the 1,3-dipolar azide-alkyne cycloaddition catalyzed by Cu(I) nanoparticles using a wide-field microscope, and they found that

the catalysis occurs directly at the surface of the Cu nanoparticles.[65] In another work, the photocatalytic activity of anatase TiO_2 was studied using redox-responsive fluorogenic dyes. From the room temperature wide field imaging and kinetic studies of emitted fluorescence, they determined the best crystal facet for the reaction.[66] Furthermore, Roeffaers et al.[67] used the single molecule technique to study the self-condensation of two furfuryl alcohol molecules over zeolite crystals, where they were able to monitor the catalytic reactions in single zeolite crystals and distinguish between the reactants and products using a wide field microscope.[67]

In these studies, nanometer spatial resolutions were achieved by recording the point spread function (PSF) of individual probe molecules and locating the center by fitting it to a Gaussian distribution.[54] We can theoretically design better catalysts if we can develop a better and more quantitative understanding of the relationship between the surface characteristics of heterogeneous catalysts and catalytic activity under ambient conditions instead of at low pressures or ultra-high vacuum conditions.[60] Single-molecule experiment results are usually supplemented or verified by using ensemble measurements such as atomic force microscopy (AFM), scanning electron microscopy (SEM) and extended x-ray absorption fine structure (EXAFS).[54]

1.7 Objectives and Motivation of the present work.

The objectives of this work were to synthesize acid-base bifunctional aldol condensation catalysts as thin films – with gradients in composition, to characterize the local acidity on these catalysts using single molecule spectroscopy, and to correlate this local acidity with catalyst activity for a probe aldol reaction at the single molecule level. This work was motivated by the need to better understand the nature of the catalysts used for the important aldol condensation reactions. Characterizing the properties of these catalysts at nanometer length scales will help develop more active and selective aldol condensation catalysts. Also, the use of catalysts films with gradients in

functionalities will help speed up the screening process for new catalysts, save materials, and allow for direct comparison of different catalyst configurations with less sample–to–sample variation.

Chapter 2 - Preparation and characterization of catalyst films

2.1 The sol-gel method

The sol-gel process can be broadly defined as the transition of a precursor solution to a "sol" and then a gel. Metal alkoxide precursors or metal salts undergo hydrolysis and condensation reactions in the presence of catalysts and water to form interconnected networks. These networks aggregate to form a colloidal solution called a sol. The colloidal particles in the sols transition to gels by aggregating into an integrated network of nanoparticles or bulk polymerize.[68] Common precursor materials consist of a metal surrounded by organic or inorganic ligands. Alkoxy ligands such as methoxy and ethoxy are among the most common ligands used in sol-gel synthesis.[68–72]

There are three fundamental reactions during the sol-gel process of silicon alkoxides.[69] These are hydrolysis, condensation of silanols, and generation of water and alcohol. The reactions are carried out in the presence of a solvent due to the immiscibility of the water and silanols. The water: silica molar ratio (r) controls to a large extent the nature of the product of the hydrolysis. Equation 2.1 represents the complete hydrolysis and condensation of a tetraalkoxide. In practice, hydrolysis rarely goes to completion, so r > 2 is required.[69]

$$nSi(OR)_4 + 2nH_2O \rightarrow nSiO_2 + 4nROH \qquad (2.1)$$

The hydrolysis and condensation of silica are pH-dependent,[69,71] so the nature of the final material formed depends on the conditions during the sol-gel process. Catalysts are used to enhance the rate of the hydrolysis reaction.[73] The mechanisms of acid and basic catalysis are shown in Figure 2.1. Solvent molecules may also participate in the sol-gel process by reducing the catalytic activity if they hydrogen-bond to hydroxyl ions or hydronium ions of the catalysts, and they can influence the hydrolysis mechanism. Transesterification can occur if the alkoxides are hydrolyzed in alcohols that contain different alkyl groups. Condensation leads to the formation of

siloxane bonds.[69] In multicomponent synthesis, it is possible to hydrolyze a mixed-alkoxide system or sequentially add different alkoxides to partially hydrolyzed precursors.[69]

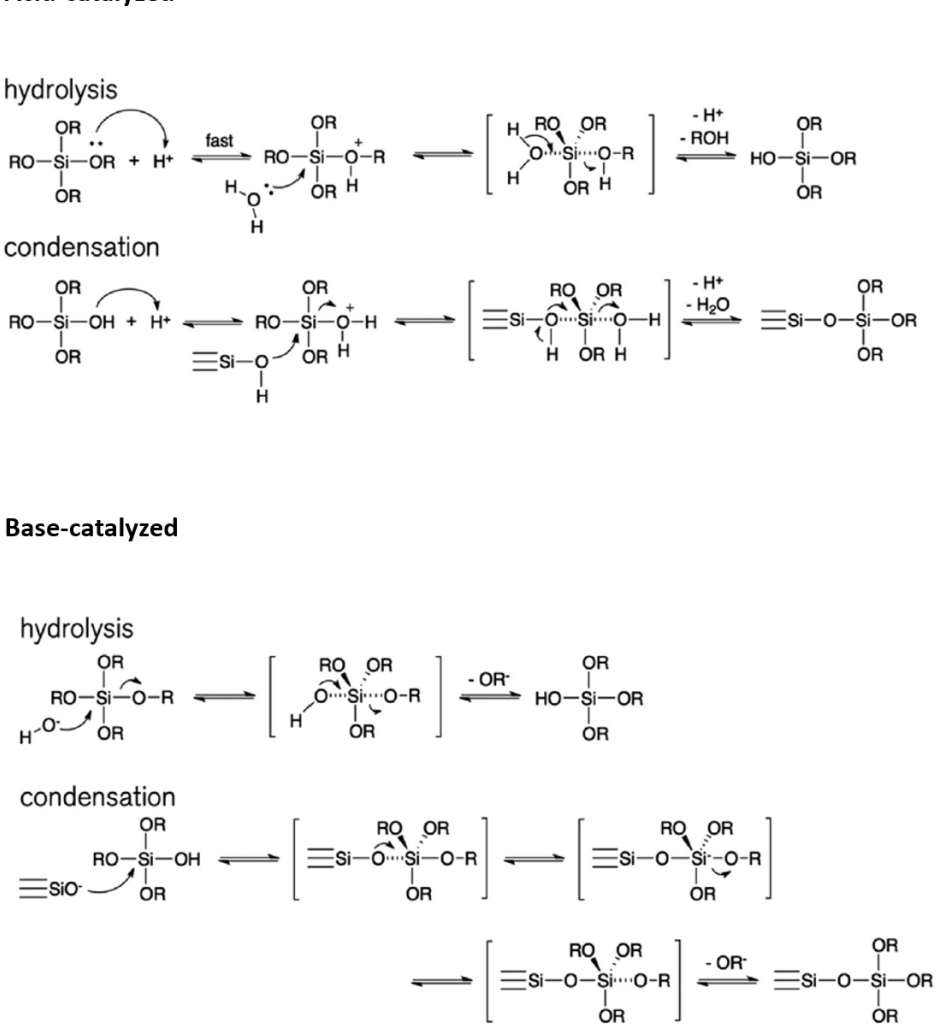

Figure 2.1 The mechanisms of acid and base-catalyzed hydrolysis and condensation of alkoxysilane precursors in sol-gel processing[68]

2.2 Sol-gel film formation

The three main methods of film deposition from sols are dipping, spinning, and spraying. Other methods include electrophoresis and thermophoresis settling.[68,69] The microstructure, as defined by the pore volume, pore size, and surface area, of the deposited film, can be controlled in

sol-gel film deposition methods.[68,69,74] Steps in the deposition of thin films include solution spreading and evaporation (progressive concentration) where the molecules in the liquid state gain enough energy to overcome the surface tension barrier. The deposited films can then be consolidated and stabilized by heat treatment or aging. The films can also be functionalized afterwards.[74]

2.2.1 Dip-coating

This is the easiest method, and it gives the best control of the process conditions.[74] This method is roughly divided into five stages. These are immersion, start-up, deposition, drainage, and withdrawal. In dip coating, up to six forces determine the thickness of the film formed. These are the upward viscous drag on the liquid, gravity, surface tension in the concave meniscus, the inertial force of the boundary liquid arriving at the deposition region, surface tension gradients, and disjoining or conjoining pressure. At a low substrate speed and low sol viscosity (common in sol-gel processing), the film thickness can be expressed by the Landau and Levich relationship shown in Equation 2.2.[69]

$$t = \frac{0.94(\eta u)^{\frac{2}{3}}}{\gamma_{lv}^{\frac{1}{6}}(\rho g)^{\frac{1}{2}}} \qquad (2.2)$$

where η is the liquid viscosity, u is the substrate speed, γ_{lv} is liquid-vapor surface tension, ρ is the density of the liquid and g is the acceleration due to gravity.

2.2.2 Spin-coating

This process takes place in four stages which are deposition, spin-up, spin-off, and evaporation. It also produces uniform thickness films. It is controlled by two forces: the centrifugal force acting radially outward and the viscous force which acts radially inward.[69]

At the initial spin-off, thickness (h) is given in Equation 2.3 as

$$h(t) = \frac{h_o}{\sqrt{1 + \frac{4\rho\omega^2 {h_o}^2 t}{3\eta}}} \qquad (2.3)$$

where h_0 is the initial thickness, ω is the angular velocity, t is the time and ρ is density.

In the end, thickness (h_{final}) is given in Equation 2.4 as

$$h_{final} = (1 - \frac{\rho_{Ao}}{\rho_A})(\frac{3\eta e}{2\rho_{Ao}\omega^2})^{\frac{1}{3}} \qquad (2.4)$$

where ρ_A is the mass of volatile solvents per unit volume, ρ_{A0} is the initial value and e is the evaporation rate which depends on the mass transfer coefficient.[69]

2.2.3 Physical vapor deposition (PVD)

This involves the heating or evaporation of a precursor to achieve a practical vapor pressure where the atoms and molecules can be transported and deposited. In PVD, transport depends on the pressure inside the deposition chamber. The stages of PVD include the adsorption of atoms/molecules on the substrate surface, lateral diffusion of the species on the surface, incorporation of species by the formation of bonds with each other or the surface, nucleation to form aggregates, and the formation of crystallographic structures and microstructures. The surface diffusion step dominates the development of the film structure.[75]

2.3 Characterization of sol-gel materials

To establish the presence of covalently bonded moieties on the surface of bulk catalysts rather than physisorbed species, J-coupling NMR is frequently used.[76] Thin films have low sample mass, so it's difficult to use the same method. The optical structure and optical properties of sol-gel thin films can be characterized using methods such as FTIR, Raman spectroscopy, UV-Vis-NIR, and fluorescence spectroscopy.[77] An IR spectrum reveals vibrations of molecular functional groups. There is a relationship between observed spectral bands and the molecular structure.[77]

Raman spectroscopy provides structural information by probing the vibrations of a molecule through the inelastic scattering of light passing through the sample.[77]

2.3.1 XPS mapping

XPS is a technique used to analyze the chemical state and composition of surfaces. Here, a sample is irradiated by single energy X-ray photons, and photoelectrons are emitted.[78] The binding energy (BE) of the ejected electrons is given in Equation 2.5

$$BE = h\nu - KE - \psi_s \qquad (2.5)$$

where hν is the characteristic energy of an x-ray photon, KE is the kinetic energy of the ejected photoelectrons and ψ_s is the spectrometer work function.

The binding energy observed for different species can be used to identify chemical states since the energy of photoelectrons emitted from a sample is characteristic of each element.[78] XPS can be used to study the distribution of chemical functionalities across a surface. Mapping by serial acquisition helps to measure the distribution of elements and /or their chemical states. Here, the analysis position is fixed, and the specimen surface is moved relative to this position.[79] XPS mapping can generate elemental maps over an entire area, or it can generate functional group maps. These maps can reveal the chemical composition of individual sample regions and variations therein. Haack et al[80] used XPS mapping to create elemental maps of C and Si in a study of corrosion-induced bond failure for an epoxy adhesive applied to electro-galvanized steel.[80] XPS mapping has also been used to study the formation of amine gradients by measuring the N1s XPS peak at different positions on a film.[81,82]

2.3.2 FTIR

An IR spectrum reveals the frequencies of vibrations for the different functional groups found in a sample. IR spectroscopy can be used to identify unknown materials and their

concentration in a sample.[83–85] There are various modes of FTIR sampling such as transmission mode where an IR beam is passed through a sample and impinges on a detector to produce the IR spectrum. For films, reflectance sampling methods are most often used. When the surfaces are smooth and shiny, specular reflectance is the preferred method while diffuse reflectance mode is better suited to rough surfaces.[83]

Perhaps, the easiest and most common method of FTIR sampling is the attenuated total reflectance (ATR) mode. It allows for the measurement of spectra of gases, solids, and liquids without the need for sample preparation. It works by quantifying the changes that happen to an internally reflected infrared beam, once it encounters a sample. Due to the constructive interference between two incoming and outgoing IR beams at the point of total internal reflectance, there is an enhanced amplitude (which is greater than on either side), hence the IR beam goes into the sample. Because of its low penetration depth, ATR is not too sensitive. Only molecules with concentrations > 0.1% can be seen.[83]

Different sampling modes of FTIR have been used to study thin films. Using a Si-ATR plate, the water contact of poly(methyl)methacrylate films was studied by Franses and co-workers.[86] The Higgins group has used FTIR to study the gradient in methyl content of films deposited on a silicon wafer using transmission mode FTIR,[87] and the use of ATR-FTIR sampling mode to study thin films was discussed by Gherardi and co-workers where it was shown that for best results, the sample should be thicker than the ATR sampling depth to prevent reflection by the substrate.[88]

2.3.3 Spectroscopic Ellipsometry

This non-destructive technique is used to measure the thickness of materials. It measures the change in the polarization state of a beam of light when it is reflected from or transmitted

through a sample.[89,90] In a typical experiment, linearly polarized light is incident on a surface and the reflected light is elliptically polarized. The p and s components of the reflected light are different, and the phase difference or amplitude difference in their electric fields can be used to measure the thickness.[90] The reflectivity ratio, ρ is the ratio of the reflectivity for p-polarized light (r_p) to the reflectivity for the s-polarized light (r_s) and it is defined in Equation 2.6.

$$\rho = \frac{r_p}{r_s} \qquad (2.6)$$

ρ is defined by two parameters, the magnitude of the reflectivity ratio (ψ) and its phase (Δ) as

$$\rho = e^{i\Delta} \tan(\psi) \qquad (2.7)$$

In a typical measurement, a selected model and thin-film equation are used to generate ellipsometry data that is then used to quantitatively determine film thickness and refractive index. The generated data is fit to the measured data using a Levenberg-Marquardt algorithm to obtain the best possible fit. The Cauchy relation, a simple dispersion model, is commonly used to describe the refractive index of transparent films in the visible range.[87,90,91] It is expressed in Equation 2.8.

$$n = A + \frac{B}{\lambda^2} + \frac{C}{\lambda^4} \qquad (2.8)$$

Here, A represents the amplitude of the material index while B and C give the shape of the index as a function of wavelength (λ). A typical fit for the thickness measurements made in this dissertation is shown in Figure 2.2.

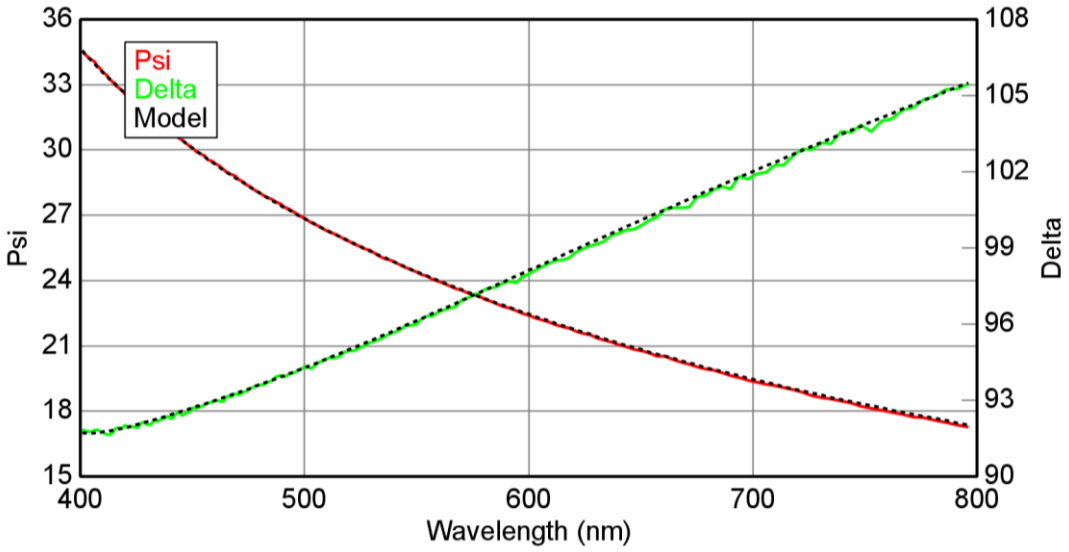

Figure 2.2 Spectroscopic ellipsometry data for a TMOS base-layer coated silicon wafer. The colored lines represent the raw data fit to a model for a single layer transparent film on silicon (black dashed lines)

2.3.4 Static water contact angle (WCA)

The placement of a liquid droplet on a film surface provides the means to probe chemically relevant parameters such as its surface energy. The contact angle (θ) is the angle formed by a liquid at the boundary where liquid, solid, and gas intersect. Measurement of the contact angle is a quick quantitative method to determine the wettability of a surface.[92,93] The static (sessile drop) method is commonly used for smooth surfaces where there is minimal movement in the three-phase boundary of a droplet on a surface. It has a precision of ~ 2° and is not suitable for samples with contact angles < 10° It is based on Young's equation (Equation 2.9) which assumes that the interfacial forces are thermodynamically stable.[94,95] The measurement is carried out by a drop shape analysis which requires the accurate capture of the image of a droplet.[92,95] Figure 2.3 shows the contact angle of a liquid on a solid surface.

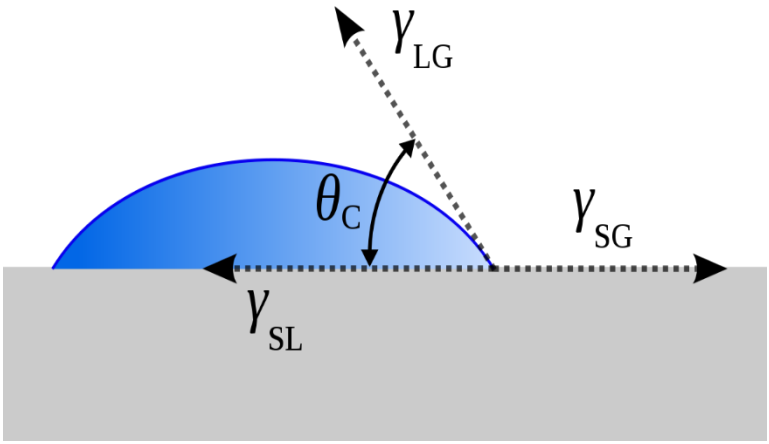

Figure 2.3 The contact angle of a liquid with a solid surface

$$\gamma_{sg} = \gamma_{sl} + \gamma_{lg} cos\theta c \qquad (2.9)$$

where θ_c is the contact angle, γ_{lg} is the surface tension of the liquid, γ_{sl} is the interfacial tension between the liquid and solid, and γ_{sg} is the surface free energy of the solid.[96]

Contact angle measurements have been used to check the quality of monolayers and to monitor the completion of monolayer-forming reactions,[97] to observe the wettability of films produced by the vapor-phase and aqueous phase deposition of various aminosilanes on silica surfaces,[98,99] to measure the hydrophobicity of coatings to improve their water repellency,[100] to monitor the adsorption process of thiol molecules on a gold surface,[101] and to determine the gradient of methyl or hydroxy-terminated thiolates on gold-coated substrates.[102]

2.3.5 Fluorescence spectroscopy

Fluorescence detection, a sensitive analytical technique that was primarily used in biological and chemical sciences, is now being increasingly used in other fields including nanotechnology and heterogeneous catalysis.[44] The physical structure of molecules determines their electronic structure and that in turn determines their fluorescence spectrum and yield. The

fluorescence of dye molecules also depends on the properties of their surroundings. The simple process of protonation or deprotonation of a dye can lead to dramatic, easily observed changes in its spectrum and this allows for the acidity or basicity (or pH) of a solution or sample surface to be determined. For the pH-sensitive dyes, their free and ion-bound forms have different emission and/or excitation spectra. The ratio of either the excitation or emission spectra can be used to track changes in the association equilibrium and determine the concentration of ions. The most common pH-sensitive dyes include fluorescein dyes, seminaphthorhodafluors (SNARF dyes), and pyranine.

A Jablonski diagram shows the processes that can occur when light is absorbed or emitted. In a typical diagram shown in Figure 2.4, upon the absorption of light, a fluorophore is excited from the ground state S_0 to a higher vibrational level in an electronic excited state S_1. In a process called internal conversion, the molecules relax to the lowest vibrational states of the S_1 level. Fluorescence emission occurs by a return to an excited vibrational state of S_0.[103,104] Some molecules with heavy atoms can undergo a spin conversion to the first triplet state T_1 (intersystem crossing from S_1). Emission from the T_1 state is called phosphorescence.[103]

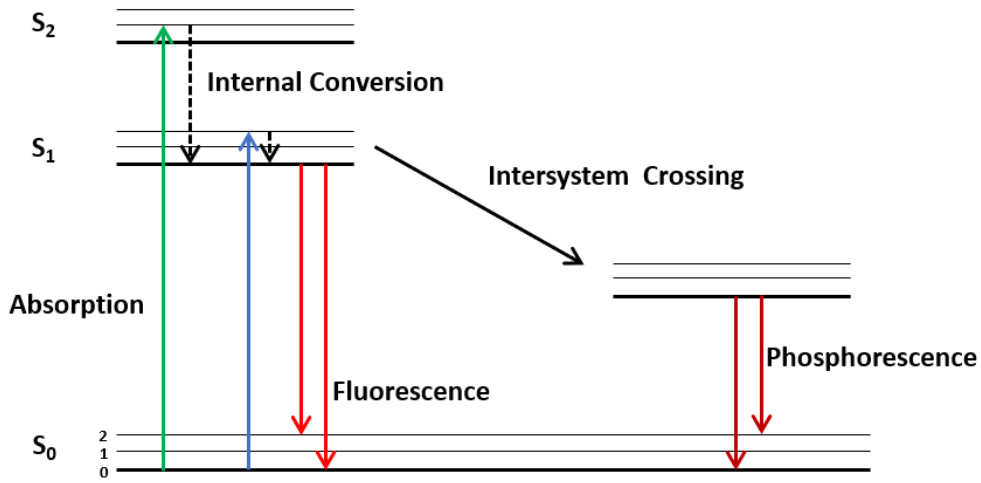

Figure 2.4 Jablonski diagram showing the principles of fluorescence

The emission spectrum is shifted to longer wavelengths relative to the absorption spectrum, and the difference between their maxima is called the Stokes shift. Fluorophores are characterized by their quantum yields and fluorescence lifetimes. A quantum yield is the number of emitted photons per number of absorbed photons. The most intensely fluorescent dyes have very high quantum yields. Fluorescein and rhodamine 6G for example, have quantum yields of ~ 95%. The fluorescence lifetime gives a measure of the time available for a fluorophore to interact with its environment, typically around 0.1 – 20 ns for organic dyes.[103]

2.4 Single-molecule spectroscopy

Single molecule spectroscopy eliminates ensemble averaging of material properties. Characterization methods such as AFM and STM can achieve atomic resolutions, but they cannot do *in situ* imaging of multiple molecules simultaneously, while SEM and TEM experiments are usually done *ex-situ* for the highest resolutions. Also, ellipsometry, x-ray, and neutron scattering can give nanoscale axial information, but laterally they average data over micro to macroscale dimensions. Single molecule fluorescence spectroscopy, on the other hand, can achieve millisecond-resolved dynamics at spatial resolutions of up to 10 ns *in situ* and under ambient conditions. Furthermore, single molecule spectroscopy is a non-invasive method compared to STM and AFM, and it can study beneath surfaces, unlike both techniques.[105,106]

In single molecule experiments, an important goal is to detect single molecules above the background. Sample and microscope component impurities, dark counts from the detector, and Raman scattering can all contribute to the background signal, so appropriate optics are used to reduce the observed volume so that a single fluorophore can be detected.[103]

2.4.1 Excitation and detection methods

Single molecule experiments can be conducted using many optical microscopy techniques including confocal, wide-field fluorescence, and near field optical microscopies. Wide-field microscopy was used for the single-molecule experiments in this dissertation. Wide-field microscopes are used to observe numerous dye molecules in a broadly illuminated area. In wide-field imaging, we can collect images at near video rates with temporal resolutions of up to 30 ms. It can be operated in the epi-illumination or total internal reflection (TIR) mode.[107]

In the epi-illumination technique shown in Figure 2.5, a laser beam is reflected off a dichroic mirror and focused on the back aperture of a microscope objective. The fluorescence emission from the sample is collected through the same objective and residual excitation light is removed.[107] The fluorescence is then detected by an array detector such as a CCD camera.

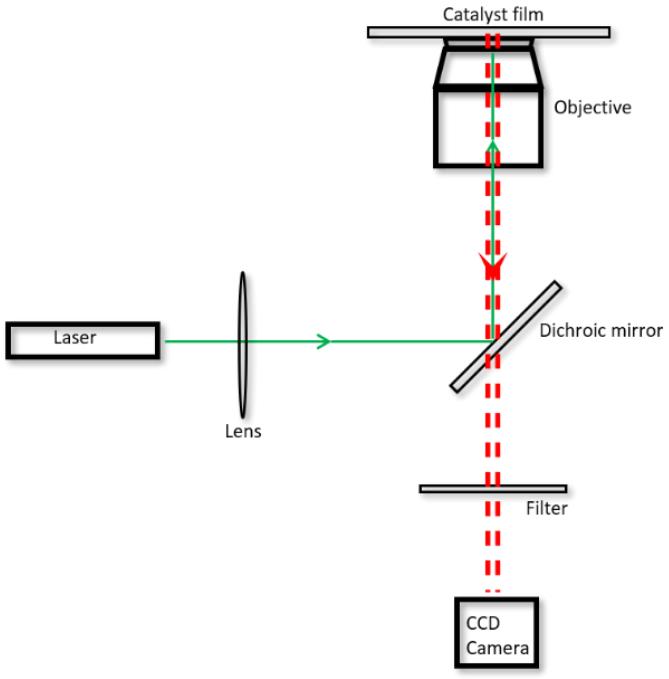

Figure 2.5 Wide-field microscopy in an epi-illumination configuration

The background fluorescence increases for very thick samples or solutions. To reduce this, we use TIR which allows only the surface to be imaged. This setup, as shown in Figure 2.6, is similar to epi-illumination but here, illumination occurs far off the optical axis of the objectives so that the light is incident on the sample at an angle greater than the critical angle.[103]

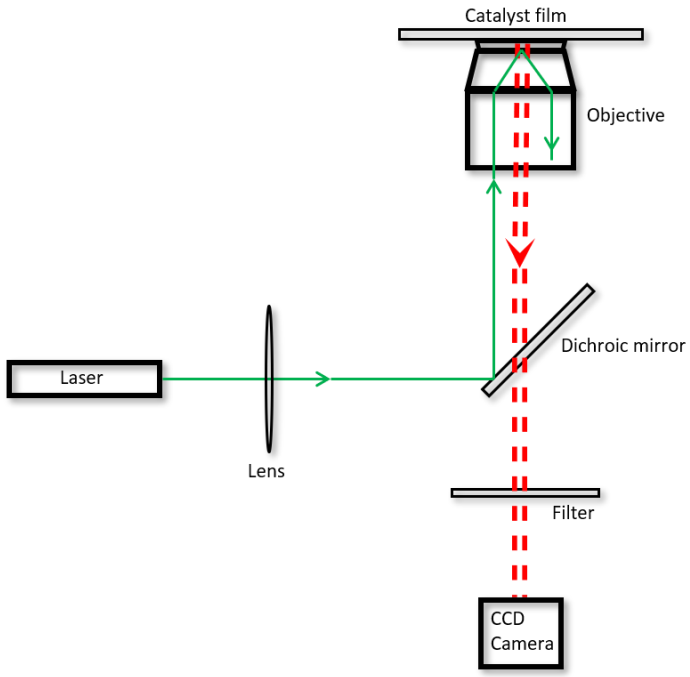

Figure 2.6 Wide-field microscopy in total internal reflection configuration

Images are produced by using the fluorescence produced by the evanescent wave created.[107] The evanescent field intensity I(z) is given as:

$$I_{(z)} = I_{(O)} e^{-\frac{z}{d}} \qquad (2.10)$$

where I(o) is the intensity at the interface, z is the depth of penetration, and d is the exponential decay distance given as:

$$d = \frac{\lambda_o}{2\pi\sqrt{{n_2}^2 sin^2\theta - {n_1}^2}} \qquad (2.11)$$

where λ_o is the extinction wavelength, n_2 and n_1 are the indices of refraction of glass/quartz and the air/liquid respectively and θ is the incident angle.[107]

Diffraction limits the spatial resolution of all conventional forms of far-field optical microscopy, including the single molecule methods employed here. However, it has been known for some time now that even though the optical resolution is limited in single molecule detection, the precision at which a molecule can be located in single molecule imaging experiments can be far better than the diffraction limit. Super localization is the finding of the position of a molecule to better precision than the diffraction limit. Here, spots are spread out over multiple pixels on a camera. The fluorescence intensity as a function of position (pixel) is displayed.[42] The point spread function of the microscope is fit to an approximate Gaussian function.

The center position estimate gives a narrower distribution with a standard deviation, σ called the localization precision.

$$\sigma = \frac{Abbe\ Limit}{\sqrt{N}} \qquad (2.12)$$

where Abbe limit ~ (λ/2NA), N is the total number of detected photons above the background, and NA is the numerical aperture. This method only works when the single molecules are spatially separated such that the point spread functions do not overlap.[42]

Chapter 3 - Single molecule studies of acidity distributions in Mg-Zr-Cs/SiO_2 thin films using C-SNARF-1.

3.1 Introduction

Alkali or alkaline metal oxide supported on silica are commonly used to catalyze aldol condensation reactions.[108,109] They are used to make high-value polymer intermediates,[16,110] and they are superior to the conventional acid catalysts[17] and strong base catalysts.[110] These classes of catalysts have been used to catalyze various reactions including the condensation of methyl propionate[16,109] or propionic acid[111] with formaldehyde, and the condensation of methyl acetate with formaldehyde.[108,112] Among the alkali metals used in these catalysts, various studies have recognized cesium as the best.[109,111] When incorporated in silica, Si-O-Cs species are formed which are medium strength basic sites.[17,112] These medium strength sites, when paired with weak acidic sites, significantly improve the catalyst performance for aldol reactions.[17,20,21] Some studies have suggested that weakly basic centers are the most active for cross-aldol condensation.[113,114]

Conventional total acidity or basicity characterization methods such as CO_2-TPD, NH_3-TPD, titration, and FTIR give important information on the nature and density of active sites,[18,115] but they do not give a distribution of the strength of the sites on catalysts. However, the interaction between these microenvironments and reactants determines the behavior of the catalysts, and this makes studying these individual distributions worthwhile. Single molecule methods have been successfully used to probe the surfaces of different catalytic materials including silica[50] and zeolites,[62] with high temporal and spatial resolution. This technique employs fluorescent probes that exhibit a change in emission characteristics depending on the nature of microenvironments on which they are immobilized. C-SNARF-1 is a common probe that is sensitive to the pH of its local environment. It emits at two different wavelengths centered at 580 and 640 nm. The ratio of the

fluorescent intensities (I_{580}/I_{640}) is a function of pH and can be used as a measure of local acidity. It has been successfully used as a molecular probe for the distribution of acidity in Si and mesoporous Al-Si catalysts. This dye undergoes a rapid protonation-deprotonation equilibrium at a much faster rate than chemical reactions or the temporal resolution of microscopes, and it is most sensitive in the pH range 6-8.[50,116–118]

This work builds on previous efforts to study the acidity distribution in the microenvironment of heterogeneous catalysts. Here, we studied the acidity distribution of the microenvironment in silica-supported cesium catalyst (Mg-Zr-Cs/SiO_2) thin films using C-SNARF-1. These catalyst films mimic the alkali oxide on silica catalysts commonly used for aldol reactions.[17,108,109,112] First, the behavior of the dye in buffer solutions of different pH and on 'dry' catalyst films was measured to obtain its calibration curves. The films were doped with nanomolar levels of the dye, excited, and the emission intensities of each dye molecule in both 580 and 640 nm bands were used to calculate the emission ratio E (I_{580}/I_{640}). These E values were used to construct histograms that represent the local acidity distribution on the films. The emission ratios were found to be dependent on the cesium content of the catalysts; they decreased with increasing cesium loading.

3.2 Instrumentation and Methods

The thickness of the synthesized films was measured using a spectroscopic ellipsometer (α-SE, J.A. Woolam). The films were prepared on a silicon wafer. The ellipsometry data were fit by using the "transparent film on silicon" model. Measurements were made at three different positions on pure silica films and cesium-modified silica films.

The chemical composition of the silica and silica-modified films was determined using XPS. These measurements were performed on a PHI VersaProbe III Scanning XPS Microprobe

with an Al Kα source (1486.6 eV). XPS data were acquired at three different positions on the films. A cesium loading of 6 wt.% was used for the XPS experiments and the sols were prepared using ethanol as the solvent instead of methanol. A 200 μm diameter spot size was employed, along with a 55 eV pass energy, and a 0.1 eV step size. All N(1s) peaks were measured relative to the C(1s) peak at 284.6 eV.

A conventional fluorimeter (Jobin Yvon-SPEX Fluoromax-2) was used to study the behavior of C-SNARF-1 in bulk solutions. These spectra were acquired from solutions in 1cm × 1cm quartz cuvettes. The fluorescence of C-SNARF-1 was also recorded on the wide-field microscope used for the single molecule experiments. These data were recorded by exciting the dye solutions in a PDMS cell placed on top of a coverslip and recording the fluorescence emission in the 580 and 640 spectral channels.

The cesium-modified silica films were imaged on a wide-field epi-fluorescence microscope set-up (Figure 1) that has been described previously.[47,50,119] The laser excitation was provided by a 514 nm laser light. It was elliptically polarized and directed through a spinning optical diffuser, reflected from a dichroic beam splitter (Chroma 555, DCLP). The excitation beam was focused onto the back aperture of a 1.49 NA 100X oil immersion objective (Nikon Apo-TIRF), to excite the C-SNARF-1 molecules doped in the samples. The epifluorescence signal was then collected by the same objective and separated from the excitation light by passing through the same dichroic beam splitter and a 550 nm colored-glass long pass filter. The emission signal was split into two separate spectral bands 640 ± 20 nm and 580 ± 20 nm using an image splitter (Cairn Research Optosplit II) which has a second dichroic beam splitter (Chroma 610, DCLP). The fluorescence spectra in the two bands were detected simultaneously by a CCD camera (Andor iXon DU-897). The videos were taken at 0.5 s exposure time and were 80-100 frames long. The

time interval between each frame was about 600 ms. The videos were analyzed by a LabView program developed in-house. The program was used to locate each diffraction-limited fluorescence spot in the two spectral channels. The spots were fit to 2D Gaussian functions for better spatial resolution by determining the peak amplitude of each spot and its location the spatial resolution of the experiment was resolved to ~50 nm. The ratios (I_{580}/I_{640} = E) of each spot were calculated for thousands of dye molecules and represented as a histogram. This histogram was fit to a Gaussian distribution. The peak of this distribution represents the E value of the dye in these films.[50,119]

3.3 Sample preparation

Cesium-modified microporous silica (SiO_2) thin films were synthesized on microscope coverslips or silicon wafers. The sols were prepared by the hydrolysis of tetramethoxysilane (TMOS) followed by the co-condensation of different metal nitrate solutions. TMOS (0.3g), methanol (7mL), water (0.156 mL), and 0.1 M HCl (60 μL) were mixed in a glass vial for 1h and kept overnight in a desiccator. Aqueous solutions of magnesium, zirconium, and cesium nitrates were then added to the hydrolyzed silica sols, stirred for 1h, and kept overnight before use. TMOS solutions with different cesium loading were prepared by mixing appropriate amounts of the cesium nitrate solution into the pre-hydrolyzed sols. The amount of metal loading used was calculated based on the theoretical yield of silica from the complete hydrolysis and condensation of TMOS. In all sols other than the pure silica sol, the Zr and Mg loadings were maintained at 0.033 wt.% and 0.25 wt.% respectively. They were added to reduce the loss of surface area when cesium is introduced into the catalyst and to increase the number of acid sites.[16] The cesium loading ranged from 2 – 30 wt.%. The sols were then spin-cast on glass microscope coverslips (FisherFinest Premium).

Before spin-coating, the coverslips were cleaned with acetone and deionized water, dried under N_2, and cleaned under air plasma (Harrick Plasma) for 7 min to remove organic contaminants and increase the hydrophilicity of the coverslips.[120] The films were calcined at 500°C for 3h to remove any remaining solvent and hydrochloric acid. The calcined catalyst films were cleaned in air plasma for 3 min to remove luminescent residues before carrying out the single molecule experiments.

3.4 Results and discussion

3.4.1 Film thickness

The deposition of catalyst films on the substrates was confirmed by using spectroscopic ellipsometry. The measurements were done at three different locations on each catalyst films with different cesium loadings to examine the effect of incorporating these metals in the silica framework. The results in Figure 3.1 showed that there is a decrease in film thickness from about 32 nm to 27 nm with increased cesium loading, but the refractive indices of the films remained almost the same (n =1.49) from 0 to 10 wt.% cesium loading suggesting an unchanged material. At the highest cesium loading used, 30 wt.%, the refractive index is about 1.6 which indicates a significant modification of the silicate structure.

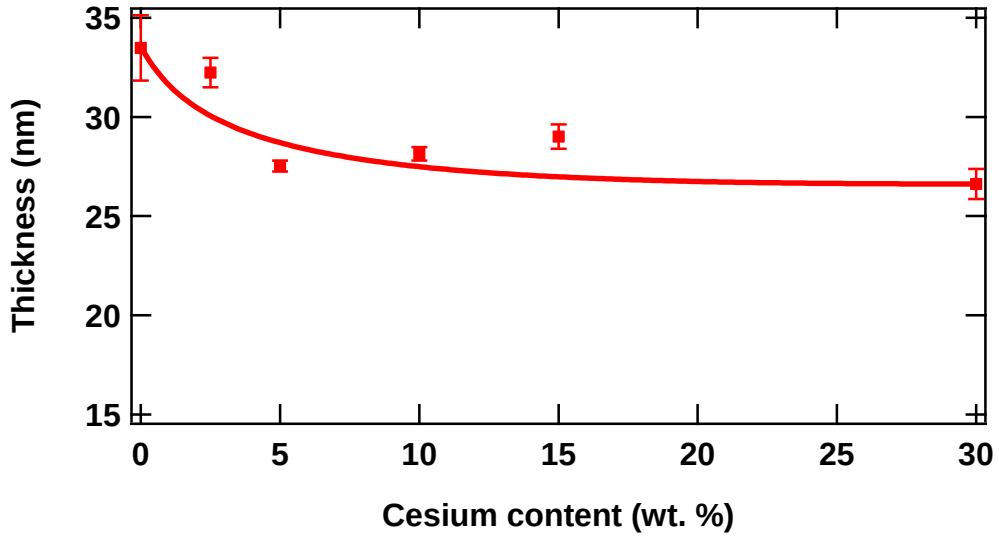

Figure 3.1 Thickness of the Mg-Zr-Cs/SiO_2 films as a function of cesium loading

3.4.2 Film composition

Figure 3.2a shows the XPS survey spectrum for a pristine SiO_2 film and Figure 3.2b shows the spectrum obtained for the Mg-Zr-Cs/SiO_2 films with 6 wt% cesium loading. Si (2p) and O (1s) peaks were observed for both films, while Cs (3d) peaks were present in only the cesium-modified films confirming its successful loading. Magnesium and zirconium were not observed due to their relatively low loadings.

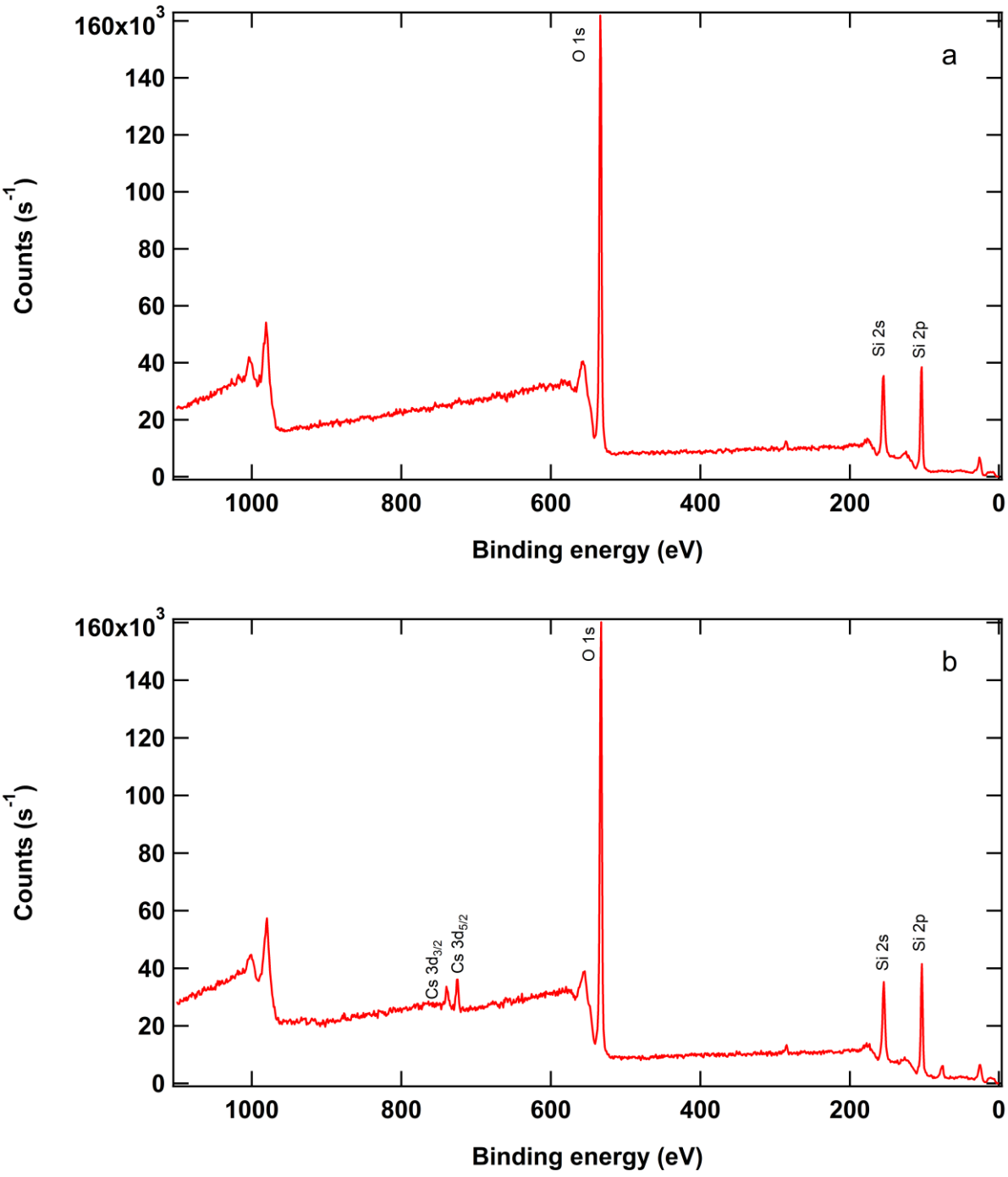

Figure 3.2 (a) XPS survey spectrum of a pristine SiO2 catalyst film (b) Mg-Zr-Cs/SiO_2 catalyst film with 6 wt.% cesium loading

3.4.3 pH Studies of C-SNARF-1 in Aqueous Solutions

C-SNARF-1 is a fluorescent dye that is sensitive to the pH of its surroundings. It changes its shape upon ligand binding, and it is mostly used to determine the presence of H^+ in cells. The protonation equilibria between its basic and acidic forms are shown in Figure 3.3. These forms exhibit different emission maxima centered at around 580 ± 20 nm and 640 ± 20 nm.[50,117,121]

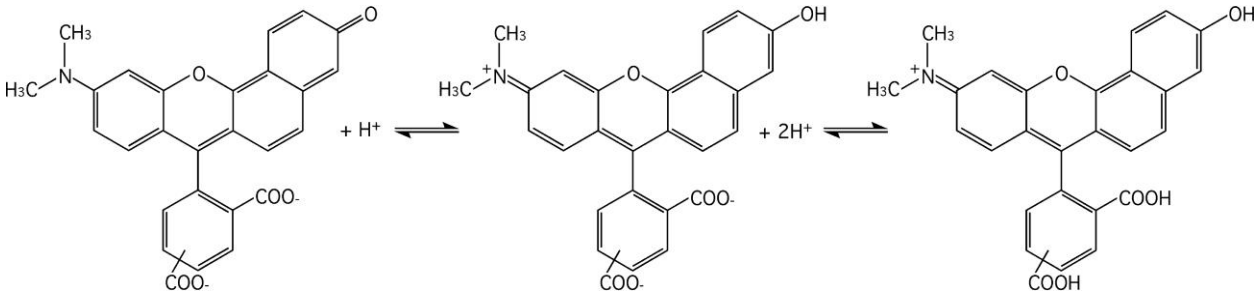

Figure 3.3 Chemical structures of C-SNARF-1 in its protonated and deprotonated forms.

First, the pH response of C-SNARF-1 in phosphate buffer solutions of different pH was studied using a conventional fluorimeter. The results are shown in Figure 3.4. For each spectrum recorded, the areas under the two spectral bands were measured and used to calculate an emission ratio $E = I_{580}/I_{640}$. These ratios were plotted as a function of pH and shown in Figure 3.5. The spectra and emission ratios of C-SNARF-1 in solutions of different pH have been measured previously,[50,122–125] and the results in Figure 3.4 and Figure 3.5 are similar to them. E reduces significantly between pH 4.5 and 8.5, and the response of C-SNARF-1 in this range (acidic - weakly basic) is most important to the present studies. The transition in this range is most likely due to the protonation equilibrium shown in Figure 3.3.

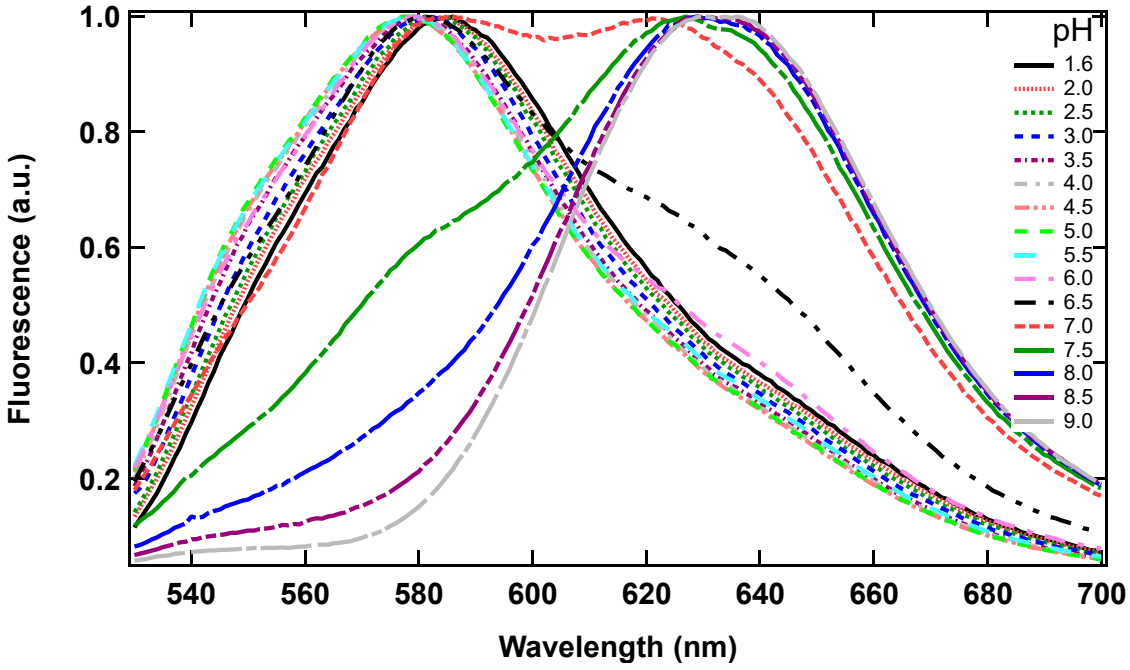

Figure 3.4 Spectral data for C-SNARF-1 in aqueous solutions of pH ranging from 1.6 to 9 recorded on a fluorimeter

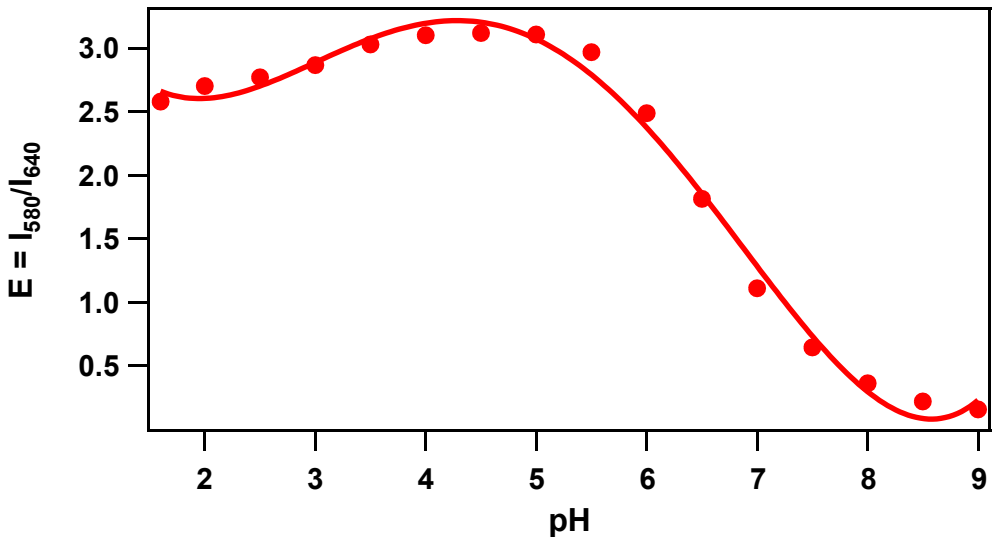

Figure 3.5 Ratio of C-SNARF-1 emission in the 580 and 640 nm spectral bands shown in Figure 3.4

Solution phase pH-dependent emission spectra for C-SNARF-1 were also collected on the wide-field microscope used for the single molecule experiments. The results were analyzed using

the same method by calculating the emission ratios and displayed in Figure 3.6. The trends are similar, but the emission ratios differ slightly, probably because of the difference in the transmission spectra of the fluorimeter and wide-field microscope.[50]

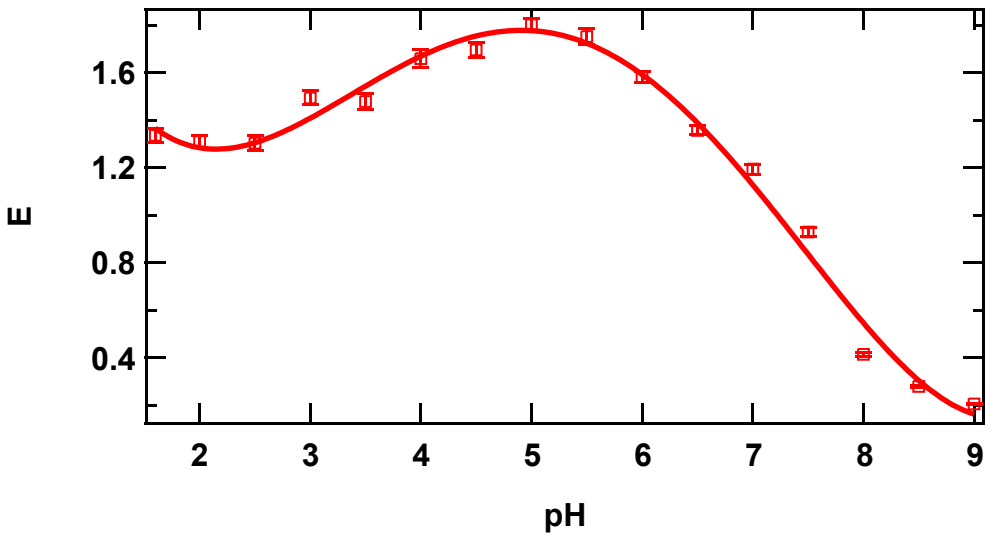

Figure 3.6 Ratio of C-SNARF-1 emission in the 580 and 640 nm spectral bands recorded on a wide-field microscope

3.4.4 Acidity Properties of Mg-Zr-Cs/SiO_2 Films Probed by SM Methods.

C-SNARF-1 shows a different emission characteristic when embedded in catalysts/physiological systems (*in situ*) relative to its behavior in aqueous solutions.[117,121] To calibrate this response, the thin catalyst films were immersed in 50 mM phosphate buffer solutions of different pH for 24h, dried, and loaded with nanometer levels of the dye. These experiments were done to estimate the apparent local pH in cesium-modified silica films. Representative images for videos in the two spectral channels at different pH are shown in Figure 3.7.

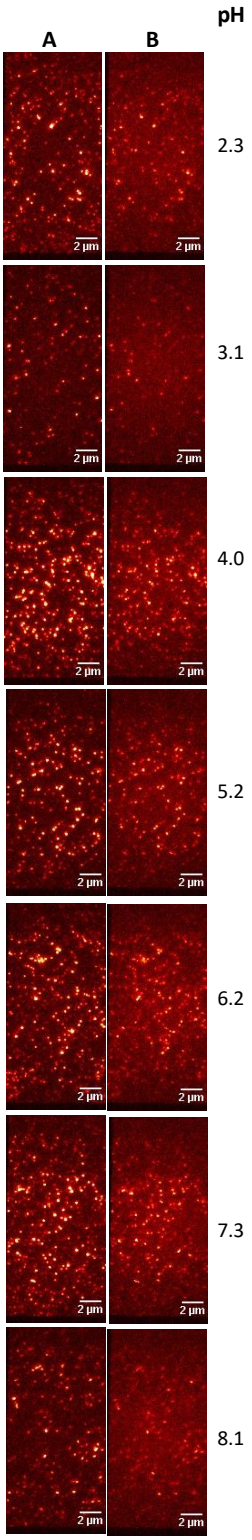

Figure 3.7 Images of C-SNARF-1 in the 580 (A) and 640 (B) nm emission channels recorded at different apparent pH

The emission ratios of C-SNARF-1 in the two spectral channels were collected for thousands of molecules at each pH and used to construct histograms shown in Figure 3.8. E distributions were observed to shift with effective local pH differently than shown for bulk solution data. The median E values of the distribution were plotted as a function of pH and shown in Figure 3.9

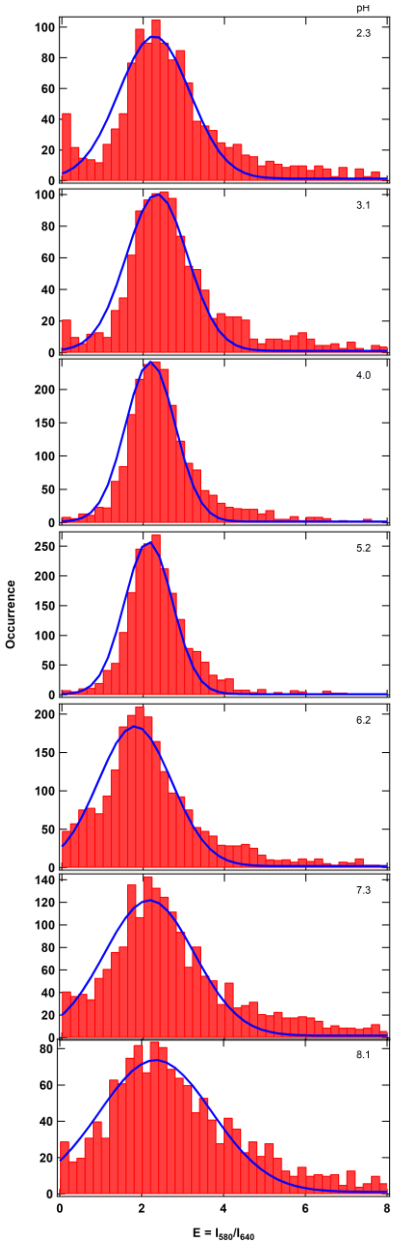

Figure 3.8 Histograms of SM emission ratios, E, obtained from a series of cesium-doped silica thin films treated in solutions of the specified pH.

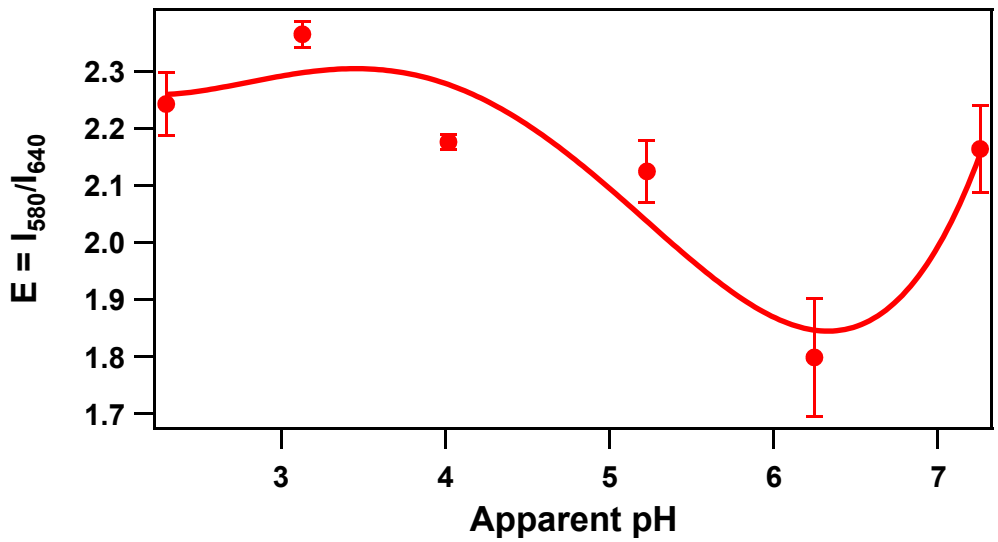

Figure 3.9 Median emission ratios (from the data in Figure 3.8) as a function of the apparent pH

Here, the maximum in the E appears around pH 3, and between pH 6.3 and pH 7, the emission ratio increases rather than reduce as expected. This is probably because of a strong interaction between the dye and cesium, or the degradation of these siloxane bonds in decreasingly acidic solutions. These results indicate that C-SNARF-1 is of limited use in sensing local pH beyond 6.5. Between pH 6-8, the distribution becomes very broad. Previous works have attributed this to the enhanced sensitivity of C-SNARF-1 to changes in pH at this level. Here, it is most likely because of the interaction between the dye and the cesium in the silica films with the surface silanols.

Mg-Zr-Cs/SiO2 composite films with 0 to 20% (weight ratio) of cesium were prepared using the method described above. They were doped with nanomolar levels of C-SNARF-1 and imaged under a wide-field microscope. Representative images at different Cs loading are shown in Figure 3.10.

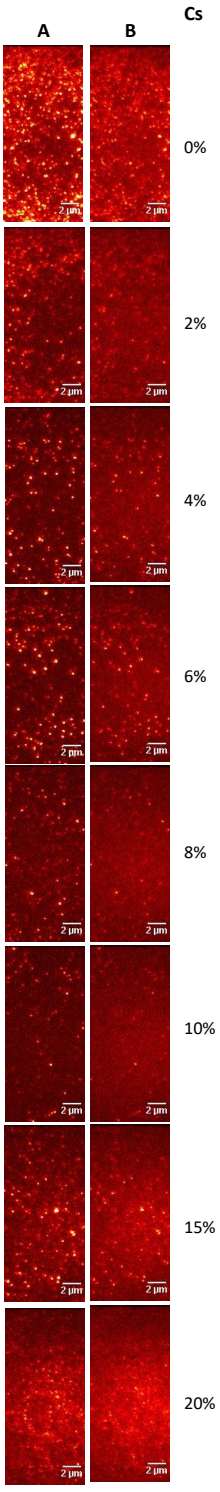

Figure 3.10 Images of C-SNARF-1 in the 580 (A) and 640 (B) nm emission channels obtained from a series of Mg-Zr-Cs/SiO_2 thin films with different cesium loadings.

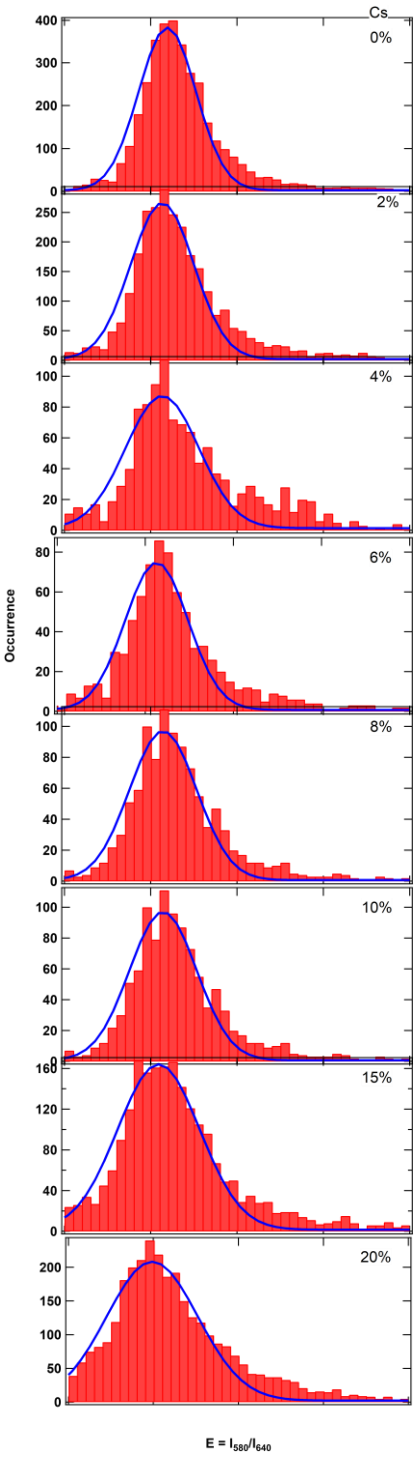

Figure 3.11 Histograms of SM emission ratios, E, obtained from a series of cesium-doped silica thin films with different cesium loading.

The emission ratios of C-SNARF-1 in the two spectral channels were collected for thousands of molecules at each cesium loading and used to construct histograms shown in Figure 3.11. We observed that the relative fluorescence from the 640+20 nm spectral band (A^- form of C-SNARF-1) increases with increasing cesium content from 0-20 wt.%. This trend can be better visualized by plotting the median emission ratio (E) for each distribution as a function of cesium loading, shown in Figure 3.12. E decreases gradually with increasing cesium content.

The distributions have a peak at E ~ 2.35 at the low cesium loading, which compared to the calibration plot in Figure 3.9, suggests the microenvironment of the films has a pH of ~3.2 at that composition. With increasing cesium content, the E reduces to about 1.9, and the calibration plot indicates the pH of films is ≥ 6.0.

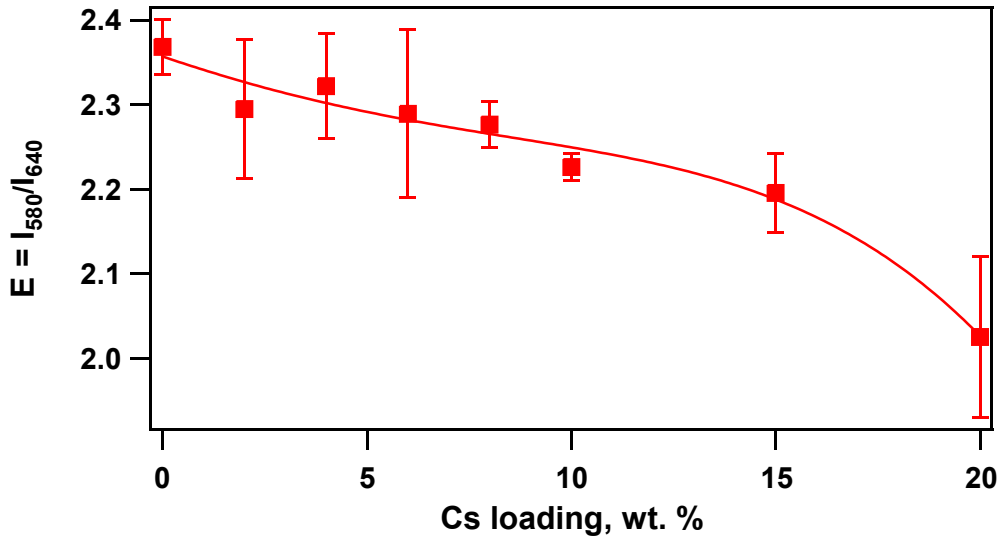

Figure 3.12 Median emission ratios (from the data in Figure 3.11) as a function of cesium content

Figure 3.12 shows a decrease in E with increasing cesium content (high pH) like what was observed in the calibration plot (Figure 3.9). We can conclude that as the cesium content increases, the microenvironmental pH of the catalyst films increase. This is most likely due to a relative

decrease in the density of weakly acidic silanols, and a corresponding increase in the presence of basic Si-O-Cs species.

The histograms in Figure 3.11 may also provide some information on the distribution of the active sites. At low cesium loading, the Gaussian width of the histograms is around 1.0. The distribution becomes increasingly broader at high cesium loading, with widths of around 1.5 at 20% cesium loading. The increase in the gaussian width might be due to measurement noise because of sample–to–sample variation. It is also likely that the broadening distribution is due to the increase in heterogeneity of the films, with the catalysts' microenvironment incorporating acidic and weak basic sites near one another. However, we did not quantify the relative contributions of experimental noise or sample heterogeneity to the increase in the Gaussian width in the present study.

3.5 Conclusions

Mg-Zr-Cs/SiO_2 thin films which represent bifunctional catalysts used to catalyze aldol condensation reactions were synthesized. Single molecule detection methods were used to examine this distribution of acidity on these films with different cesium loading using a C-SNARF-1 probe. This dye was shown to be an effective indicator of local acidity between pH 3 and 6.2. The emission intensity ratios (E) were found to increase with increasing cesium content of the films which were interpreted to indicate a decrease in the local acidity from 0-30% Cs loading. The distributions at higher pH and high Cs loading were seen to be broader than those at low cesium content, and this might be due to the greater film heterogeneity with increasing cesium loading. This work demonstrates the use of single molecule methods to characterize this distribution of local acidity and heterogeneity in bifunctional aldol condensation catalysts. It also shows the limitation of using C-SNARF-1 to track acidity changes at high pH.

Chapter 4 - Single Molecule Spectroscopy Studies of Acid-Base Chemical Gradients using Nile Red as a Probe of Local Surface Acidity

4.1 Introduction

Bifunctional catalysts are frequently found to be superior to their monofunctional analogues, with enhanced catalytic activities and selectivities attributable to cooperativity between the chemically distinct sites on their surfaces.[11] Silica materials incorporating both inorganic and organic functional groups comprise one class of bifunctional materials now being widely explored.[11] Oftentimes, the bifunctionality of these materials derives from the presence of both acidic and basic surface sites. The acidic sites may comprise weakly acidic silanol groups inherent to the silica surface, or more acidic carboxylic, sulfonic, or phosphoric acids may be attached during materials synthesis.[126] Similarly, basic sites may be incorporated through covalent attachment of aminosilanes to the silica matrix. Bifunctional acid/base materials are now being investigated for use in the heterogeneous catalysis of aldol,[24] nitroaldol,[24] Knoevenagel,[127] and Michael reactions.[127] While these materials show tremendous promise, a full understanding of their cooperativity has not yet emerged. Further studies of how the acidic and basic sites on the catalyst surface interact with each other and with chemical reagents are needed to better optimize

catalyst performance. Of course, the interactions that occur between catalyst sites are determined by their spacing and organization, and the development of new means to control and measure these parameters is also warranted.

One method for controlling the spacing between active sites on the surface of a heterogeneous catalyst for use in fundamental investigations is via the preparation of gradient materials.[27,29] The surface of a bifunctional acid/base gradient incorporates high concentrations of acid at one end of the gradient and high concentrations of base at the other. A gradual variation in acid and base site concentrations, and hence their proximity to each other, occurs between the two extremes. Silica thin film gradients are now being explored in the literature and are easily fabricated by a variety of methods.[82] Physical vapor diffusion is perhaps the simplest to implement, relying on the directional diffusion of precursor vapors over a substrate, and their subsequent reaction with its surface.[128,129] By controlling the concentration of precursor present in the solvent-filled deposition reservoir, the distance between the reservoir and the substrate, and the time over which deposition occurs, gradients of controlled surface functionality, incorporating gradual variations in catalyst site spacing and interactions can readily be achieved.

Once gradient materials have been obtained, the density and organization of catalytic sites must be characterized. Classical solution-phase acid/base titrations could be used to determine the density of acidic or basic sites, although the implementation of spatially resolved titrations on gradient surfaces would be challenging. Likewise, zeta potential measurements can be used to obtain related information,[130] with similar challenges in making spatially resolved measurements. One spectroscopic method that provides elemental sensitivity and the ability to spatially resolve variations in the surface chemistry is XPS mapping. While XPS has provided valuable information on the interactions between surface sites in recent studies of acidic/basic silica gradients,[130] the

spatial resolution achieved is usually on the order of tens of micrometers. Atomic force microscopy, and chemical force microscopy in particular, are also well suited to detecting interactions between acidic and basic surface sites, in this case, with nanometer-scale spatial resolution.[131]

As effective alternatives, fluorescence-based single-molecule detection and spectroscopy experiments hold significant promise for probing the properties of bifunctional catalyst surfaces. Fluorescent probe molecules can serve as proxies for the reagents used in catalytic reactions, revealing the relevant molecular level interactions that occur at active sites with nanometer scale spatial resolution, when detected at the single molecule level. Related methods are now being widely employed to achieve a better understanding of catalysis. For example, single molecule methods have been implemented in studies of the connection between the static and dynamic properties of catalysts and their reactivity[52] and to characterize reaction kinetics. [53] They have also been used to study shape-selective catalysis on solid catalysts,[60] the accessibility of Brønsted acid sites on zeolites[59] and agarose gels,[58] transesterification reactions on layered doubled hydroxides,[60] and to explore the thermodynamics of the reversible redox reaction of resorufin on SiO_2 nanospheres.[61] In related work, spectroscopic single molecule detection has been employed to probe the acid/base properties of microporous[116] and mesoporous silica,[132] and aluminosilicate films.[50] The latter studies have employed the very few well-known, pH-sensitive indicator dyes available that are also sufficiently fluorescent to detect at the single molecule level.

Nile Red is a highly solvatochromic dye that is commonly used to characterize the polarity of bulk organic solvents.[133,134] It exhibits a profound bathochromic shift in both its absorption and emission spectra as solvent polarity increases. These spectral shifts are readily quantified and correlated with solvent dielectric properties via Mataga-Lippert theory.[103,135] Nile Red is also

sufficiently fluorescent to allow its detection at the single molecule level,[136] facilitating a variety of studies of materials polarity in local, nanoscale environments within polymer films,[135,137] in organically modified silica films[138] and along silica gradients,[119] in the surfactant-filled pores of mesoporous silica films,[139] and within organic nanotubes.[140] While alternative forms of Nile Red have been synthesized and employed to probe the acid/base properties of small organic molecules and nanomaterials,[140,141] little attention has been paid to the intrinsic acid/base response of commercial Nile Red itself. To our knowledge, only a single publication has reported its absorption and emission characteristics in the presence of an acid.[142] This previous study reported a shift in its absorption maximum from ~ 550 nm in pure ethanol to ~ 640 nm upon addition of H_2SO_4. An isosbestic point was observed at ~ 580 nm. In the same study, the fluorescence quantum yield of the dye was determined to decrease from 0.68 in its unprotonated form to 0.04 when protonated. Modeling studies suggested this response results from protonation of the molecule at the nitrogen atom of its oxazine ring.[142]

In this work, bifunctional acid/base chemical gradients were prepared by vapor phase diffusion of 3-aminopropyl-trimethoxysilane (APTMOS) over uniform silica films supported on glass coverslips. Reaction of APTMOS with the silica film created a stable aminosilane gradient. Gradient formation was verified by spectroscopic ellipsometry measurements of film thickness and sessile drop water contact angle measurements of film wettability. The gradients were subsequently characterized by X-ray photoelectron spectroscopy (XPS). XPS mapping provided a measure of film nitrogen content along the gradient direction. A two-component Gaussian function was used to fit the N(1s) XPS spectra, which incorporate peaks centered at 398.9 eV and 400.5 eV. These were attributed to the unprotonated and protonated forms of the aminosilane nitrogen, respectively. The area under the 400.5 eV peak, relative to total peak area was used to

probe spatial variations in the fraction of protonated amine along the gradient on sub-millimeter distance scales. Two-color spectroscopic single molecule detection experiments were used to probe gradient acid/base and polarity properties with sub-diffraction-limited spatial resolution.[143] Bimodal distributions of Nile Red emission characteristics were observed. These results are consistent with monotonic spatial variations in the interactions between the basic dye and acidic silanol sites along the gradient. An in-depth analysis of the spatially resolved single molecule emission data was used to explore the length scale over which spatial correlations in gradient acidity and basicity occur. The results obtained and their interpretations are certain to be of great value to those working to better understand the unique attributes of bifunctional acid-base catalysts

4.2 Experimental Section

4.2.1 Sample preparation.

Gradient and non-gradient silica films were prepared on glass coverslips (FisherFinest Premium) and on silicon wafers when required (see below). In preparation for gradient deposition, all substrates were first cleaned by rinsing with deionized water and acetone. They were then dried with nitrogen and plasma-cleaned in air for 6 min. A uniform silica base layer was subsequently created by spin-casting a silica sol on the substrate surface. These sols were prepared by mixing tetraethyl orthosilicate (TEOS), spectroscopic grade ethanol, HCl (as a 0.1 M aqueous solution), and deionized water (17.9 M□ cm), in that order, in mole ratios of 1:90:0.02:6, respectively. The mixture was then stirred for 1 h and aged in a desiccator for 24 h prior to use. Base layer films were obtained by dropping 150 µL of the sol onto the substrate, which was then spun at 2500 RPM for 30 s. As a final step, the coated substrates were stored in a desiccator for at least 24 h.

Aminosilane gradient films were prepared by vapor phase deposition of 3-aminopropyl-trimethoxysilane (APTMOS) on the silica base layer.[128] Deposition of APTMOS was carried out

at ambient laboratory temperature (~ 25° C) in a humidity-controlled Plexiglas chamber. Immediately prior to gradient deposition, each silica base layer was cleaned in an air plasma for 3 min. This process also served to activate the base layer by exposing reactive silanol groups. The activated, base-layer-coated substrate was next placed on an elevated platform in the deposition chamber. For vapor deposition purposes, APTMOS was diluted to a 1:10 ratio (by volume) in toluene. Approximately 200 μL of APTMOS:toluene solution was then transferred to an open reservoir that was positioned within the chamber at a horizontal distance of 4 mm from the base-layer-coated substrate. The substrate-reservoir distance was optimized to obtain aminosilane films of the desired thickness at the high-amine end of the gradient.[144] Each substrate was exposed to APTMOS vapor for a period of 6 min during gradient deposition. The films were then transferred to a vacuum desiccator and maintained under dynamic vacuum overnight to remove any loosely bound silanes.

For single-molecule experiments, the gradient films were doped by spin-casting (2500 rpm, 30s) a dilute (0.1 nM) ethanolic solution of Nile Red on their coated surfaces. Dye-doped films were subsequently stored in a desiccator for at least 24 h prior to use. Aminosilane functionalized gradient films were used as-prepared for ellipsometry, water contact angle (WCA), and X-ray photoelectron spectroscopy (XPS) measurements, without loading the dye.

4.2.2 Instrumentation and methods.

Film thickness. TEOS base layer and aminosilane gradient film thicknesses were measured using a spectroscopic ellipsometer α-SE, J. A. Woollam). Films employed in thickness measurements were prepared on silicon wafers. All ellipsometry data were fit using the transparent film on silicon model. No allowance was made for film roughness. Measurements were made at 2 mm intervals along each gradient, starting from the high-amine end. Film thickness

was measured both prior to and after gradient deposition at approximately the same positions. The former measurement gave the base layer thickness, while the latter yielded the gradient film thickness, after subtraction of the value for the base layer. Replicate measurements were made at ~ 1 mm intervals at the high-amine end and at 2 mm intervals at the low-amine end along the direction perpendicular to the gradient at each point.

Static water contact angle. The water wettability of each gradient film was determined by sessile drop WCA measurements. These experiments were carried out on a home-built contact angle goniometer. Measurements were taken at 3 mm intervals along the gradients by depositing 1 μL droplets of 17.9 MΩ cm water at each point and photographing the droplets through a zoom lens. Replicate measurements were made at ~ 9 mm spacings along the direction perpendicular to the gradient at each point. Photographs of the droplets were analyzed using a Plugin for the freely-available ImageJ software.[145]

Elemental composition. The chemical composition of the gradient films was verified by XPS mapping. These measurements were performed on a PHI VersaProbe III Scanning XPS Microprobe with an Al Kα source (1486.6 eV). XPS data were acquired at 1.5 mm intervals starting from the high amine end (closest to the reservoir). A 200 μm diameter spot size was employed, along with a 55 eV pass energy, and a 0.1 eV step size. All N(1s) peaks were measured relative to the C(1s) peak at 284.6 eV.

Single molecule spectroscopic imaging. Dye-doped aminosilane gradient films were imaged on a wide-field epi-fluorescence microscope that has been described previously.[146] Briefly, this microscope is built upon a Nikon TiE inverted light microscope that employs the Nikon Perfect Focus stabilization system. Nile Red fluorescence was excited by 0.5 mW (measured prior to entry into the microscope) of 532 nm laser light derived from a solid-state laser

(Coherent Sapphire, 50 mW). The laser light was focused into a spinning optical diffuser prior to entry into the epi-illumination port of the microscope. It was subsequently collected and reflected from an appropriate dichroic beam splitter (Chroma) and focused into the back aperture of a 100X, 1.49 oil immersion objective (Nikon Apo-TIRF), providing an ~ 15 μm diameter illuminated area in the sample under conventional wide-field illumination. Fluorescence from the dye molecules excited in the sample was collected by the same objective and then separated from the excitation light by passage back through the dichroic beam splitter and a 570 nm longpass filter. The dye emission was next directed into an image splitter (Cairn Research Optosplit II) that divided the signal into separate spectral bands spanning 580 ± 20 nm and 640 ± 20 nm. The image splitter employed a second dichroic beam splitter (Chroma T610lpxr) and 580/40 and 640/40 bandpass filters (Chroma). Fluorescence images in these two spectral bands were simultaneously recorded using an electron-multiplying CCD camera (Andor iXon DU-897). Fluorescence videos were acquired at 2X2 binning using conventional gain only. The videos were 80-100 frames in length. Individual video frames were acquired with a 0.5 s exposure every 0.65 s.

Fluorescence videos were analyzed using spot location/identification software developed in-house in the National Instruments LabView environment. This software has been described previously in more detail.[119,147] The program was used to separate the two spectral channels in each video, to correct for minor image distortion and offset imparted by the image splitter, and to identify, locate, and link fluorescence spots observed in the individual video frames into trajectories showing any motions and intensity or spectral fluctuations exhibited by each molecule. In locating each molecule, the individual fluorescence spots were fit to 2D Gaussian functions, allowing for the location of each molecule to be determined to a sub-diffraction-limited precision of ~ 50 nm.

Ensemble fluorescence spectroscopy. Fluorescence spectra were acquired from dilute solutions of Nile Red using a conventional fluorimeter (Jobin Yvon-SPEX Fluoromax-2). All spectra were acquired from solutions in 1 cm x 1 cm fused silica cuvettes. Ensemble fluorescence data were also acquired on the same microscope used in single molecule studies. In this case, a polydimethylsiloxane (PDMS) cell was attached to a plasma-cleaned coverslip and the coverslip placed on top of the microscope (see above) operating in total internal reflection mode. The sample cell was filled with 150 μL of each of a series of solvent mixtures containing Nile Red at 10 nM concentration. The dye was excited by 532 nm laser light (0.5 mW). Fluorescence videos 20-30 frames in length were acquired with a 0.5 s exposure time every 0.65 s. A new coverslip and PDMS cell were used for each solvent mixture to prevent cross contamination of the solutions. The videos were analyzed using the ImageJ software package. The background-subtracted emission intensities for identical rectangular areas in the two spectral channels were used to calculate the emission ratios (E).

4.3 Results and Discussion

4.3.1 Gradient characterization.

Verification that aminosilane gradients were obtained on the silica-baselayer-coated substrates was accomplished by spectroscopic ellipsometry, static WCA measurements, and by XPS mapping. Figure 4.1a shows ellipsometry data acquired from a representative aminosilane gradient. The data are plotted as a function of position relative to the original location of the deposition reservoir during gradient fabrication. The gradient was measured to be a few molecular layers in thickness (~ 0.5 nm/monolayer)[148] at the high-amine end (7 mm). It rapidly thinned to just less than one monolayer at the low-amine end (19 mm).

Figure 4.1b plots representative WCA data along a similar gradient. The WCA was largest (~ 60°) at the high-amine end, due to the greater hydrophobicity associated with its organic functionality, and smallest (~ 15°) at the low-amine end. These data are consistent with previously reported WCA results for self-assembled monolayers.[149] Together, the ellipsometry and WCA data provide conclusive evidence that the surface has been modified by the aminosilane and that a chemical gradient has been obtained.

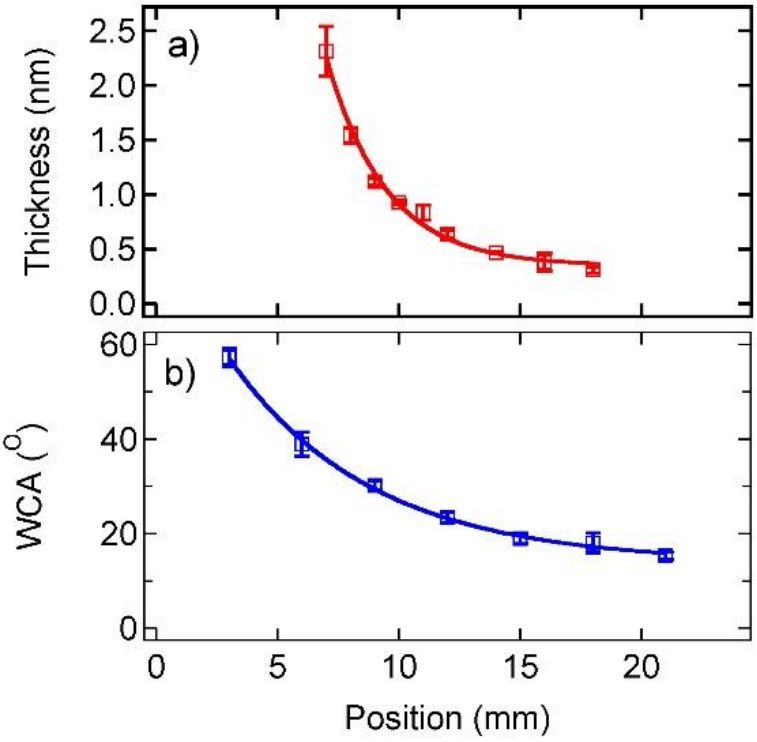

Figure 4.1 a) Thickness of aminosilane gradient as measured by spectroscopic ellipsometry. b) WCA data acquired by static water contact angle methods. Both measurements are plotted as a function of distance along each gradient, relative to the original position The error bars represent the experimental standard deviation obtained for three replicate measurements in each case.

More chemically specific information on aminosilane gradient composition was provided by XPS mapping. Figure 4.2 depicts the results of these studies along a representative gradient, with the raw XPS data shown in Figure 4.2a. The total nitrogen content of the gradient film was

quantified by determining the area under the full N(1s) peak at ~ 400 eV. Importantly, the N(1s) spectra are also sensitive to the protonation state of the nitrogen atom, with unprotonated nitrogen yielding a peak near 398.9 eV and its protonated form found at a higher energy of 400.5 eV.[150] To characterize the protonation state of the amine group, the raw XPS spectra were fit to two-component Gaussian functions (blue lines in Figure 4.2a) and the area under each of these components separately integrated. While the fitting of XPS data usually requires use of a more physically correct Voigt profile,[151] Gaussian functions serve as a suitable approximation in the present studies, given the signal-to-noise level that could be achieved for the thin film gradients. Total film nitrogen is plotted in Figure 4.2b as the full area under each spectrum (i.e., summing both components). These data reveal an approximately ten-fold decrease in film nitrogen content running between the high-amine and low-amine ends. The XPS results are consistent with the film thickness data (Figure 4.1a) although the latter measurements were initiated further down the gradient. XPS data obtained from uniformly coated aminosilane films and uncoated silica base layers are provided in Appendix A. These show the lack of a gradient in the former and the absence of detectable nitrogen in the later, as expected.

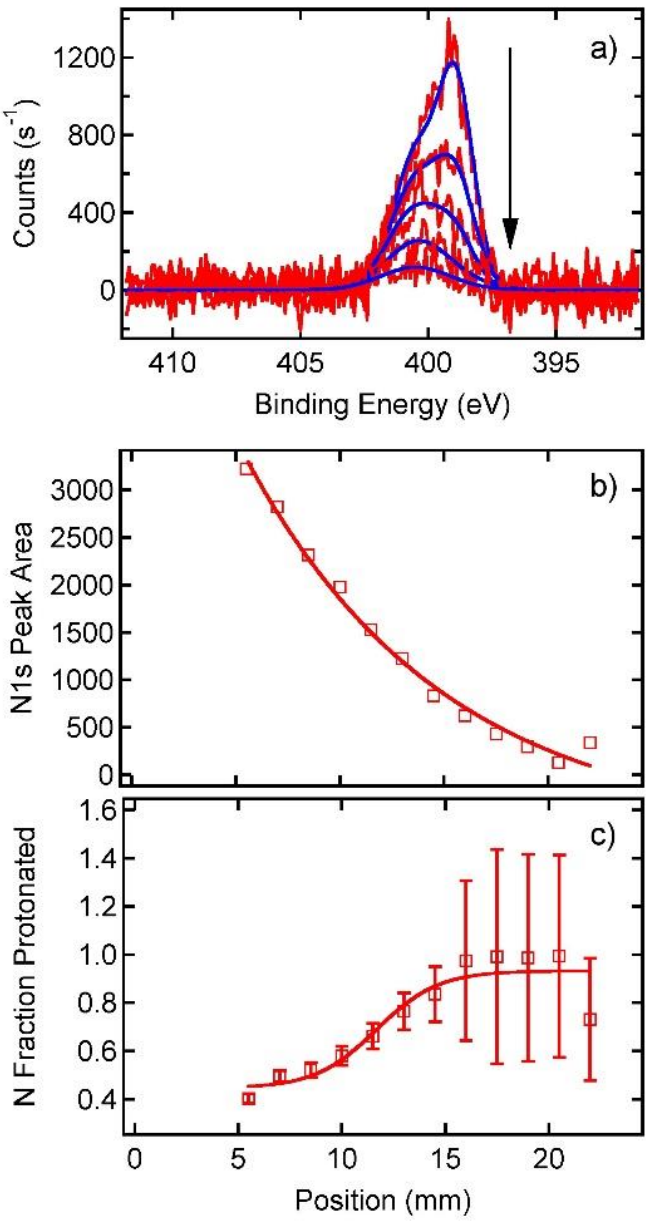

Figure 4.2 a) N1s XPS spectra (red lines) recorded along an aminosilane gradient at 3 mm spacings (see arrow) starting at the high-amine end of the gradient. Each spectrum was fit to a pair of Gaussian functions (blue lines) centered at 398.9 eV and 400.5 eV, which are assigned to the unprotonated and protonated forms of the aminosilane nitrogen, respectively. b) N1s peak area as a function of position along the same gradient. c) Protonated fraction of aminosilane nitrogen as a function of gradient position. The error bars represent estimates of the standard deviation of each value. The error bar at 19 mm is the average of the error bars at 17.5 and 20.5 mm due to weak signal at this point. All data are plotted as a function of distance relative to the approximate original position of the reservoir used to prepare the gradients.

Figure 4.2c plots the degree of amine protonation as a function of position along the gradient, as determined from the XPS data. These results show that nitrogen protonation increases with distance from the high-amine end. This reflects a transition along the gradient from regions having a high density of basic amine sites and a low density of acidic silanols (high-amine end) to those incorporating a low density of amine groups and a high density of silanol sites (low-amine end). Unfortunately, the error bars become large at the low-amine end, due to the low density of basic sites in that region. While these data reveal the presence of a gradient in film acidity/basicity, the spatial resolution achieved was on the order of a millimeter.

4.3.2 Nile Red solution-phase ensemble spectroscopy.

As noted above, Nile Red is well known for its strong solvatochromism.[133] As a result of this sensitivity to the dielectric properties of its surrounding environment, it has been widely employed to characterize the polarity of solvent systems,[133,152] ionic liquids,[153] micelles,[152,154] proteins,[155] and DNA,[156] and has also been used to probe organically-modified silica sols.[134] However, its absorption and emission characteristics are also expected to be sensitive to solution/environment acidity. Previous work in this area has, to our knowledge, been restricted primarily to studies of its spectral shift in ethanol upon addition of a strong acid.[142]

In the present work, the *acid sensitivity* of Nile Red was further explored by monitoring its emission in a series of mixtures of ethyl acetate and acetic acid. The results are shown in Figure 4.3a. Ethyl acetate and acetic acid were chosen for these studies because they have similar dielectric constants, ε, of 6.08 and 6.20, respectively.[157] Little or no polarity-dependent shift in the Nile Red emission spectrum is expected between these two solvents (see below). Instead, any spectral shift that occurs upon addition of acetic acid to an ethyl acetate solution should be due to

acid-base interactions between the acetic acid and the basic dye. Indeed, the data in Figure 4.3a show a rather significant bathochromic shift in the Nile Red emission spectrum as acetic acid is added to the ethyl acetate solution. Its spectrum is peaked at ~ 585 nm in pure ethyl acetate and at ~ 640 nm in pure acetic acid. No isoemissive point was observed along the series of mixtures. The latter observation is expected, as the spectra obtained in these solvents are relatively broad compared to their separation.

In order to better understand how the acid-dependent spectral shifts of Nile Red might be manifested in single molecule studies (see below), solution-phase ensemble fluorescence data were also acquired on the same microscope used in those studies. The results are shown in Figure 4.3b. In this case, the fluorescence in each of two spectral bands (580 ± 20 nm and 640 ± 20 nm) was recorded and used in the calculation of an emission ratio, *E*, as defined in Equation 4.1.[119]

$$E = \frac{I_{640} - I_{580}}{I_{640} + I_{580}} \qquad (4.1)$$

Here, I_{580} and I_{640} represent the fluorescence signal detected in each of the two spectral bands. A large *E* is indicative of relatively red emission and a small *E* value reflects relatively blue emission. The results shown in Figure 4.3b demonstrate that an abrupt bathochromic shift in the Nile Red emission occurs when relatively small amounts of acetic acid (5%) are added to the ethyl acetate. The fluorescence emission also becomes weaker with increasing acid concentration, as reported previously.

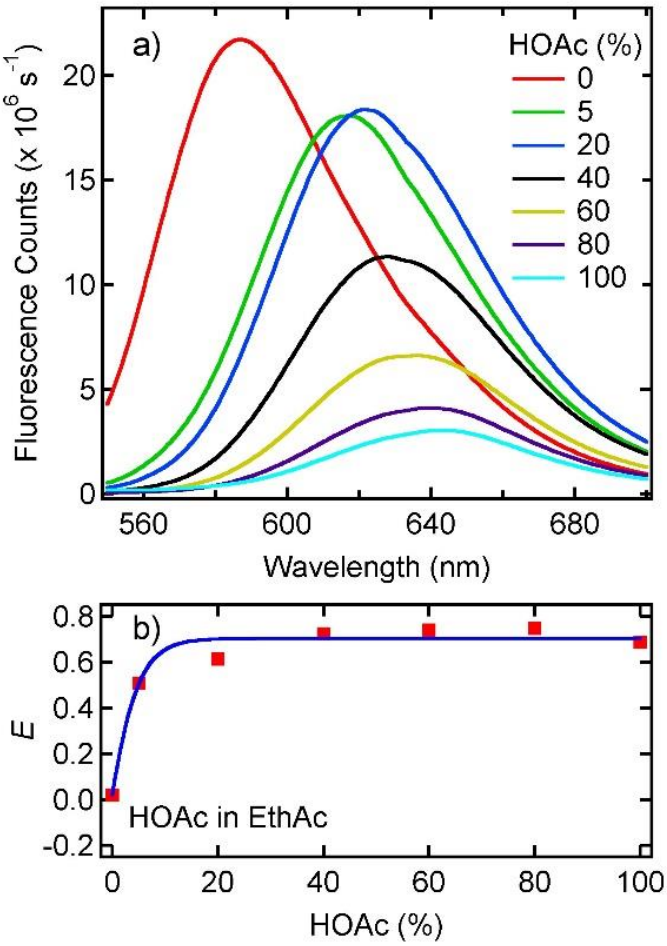

Figure 4.3 Solution phase ensemble fluorescence from Nile Red in mixtures of ethyl acetate (EthAc) and acetic acid (HOAc). a) Fluorescence spectra obtained as a function of HOAc in EthAc using a conventional fluorimeter. b) Ensemble, solution phase E values obtained from Nile Red (10 nM) in a series of HOAc/EthAc mixtures, showing an abrupt change in its emission spectrum with increasing acid concentration. The data in b) were recorded on the same microscope used for single molecule experiments.

The difference in *E* values expected for Nile Red in ethyl acetate and acetic acid, based on solvent polarity alone, may be estimated using previously reported methods, data, and mathematical relations.[119] This calculation is provided in Appendix A. Using the solvent dielectric constants given above, a change in *E* of < 0.01 units is predicted for Nile Red between pure ethyl acetate and pure acetic acid. Importantly, the shift in *E* for Nile Red shown in Figure

4.3b is ~ 0.7 units, approximately one seventy-fold larger, indicating it reflects primarily a change in protonation state, not a change in solvent polarity.

Nile Red fluorescence is certain to exhibit some dependence on gradient polarity along with the protonation effects described above. Unfortunately, it was not possible to identify a suitable solution-phase model upon which to predict the exact contributions of polarity variations along the gradient. Rather, the results of our previous work[119,147] reveal that a change in *E* of ~ 0.8 units across the full length of the gradient could be expected due to polarity effects alone. While the contributions of variable polarity and dye protonation to the measured *E* values along the gradient may be difficult to distinguish, it is expected that the effects of molecular-level acid-base interactions will dominate over the polarity effects of the thin aminosilane films in these studies. Since polarity-dependent spectral shifts are based upon the average dielectric properties of the environment surrounding each molecule,[103,135] they are not expected to be so different in the presence and absence of thin, near-monolayer films.

The response of Nile Red to the presence of acid has been attributed previously to protonation of the dye at the nitrogen heteroatom on its oxazine ring.[142] However, in both the non-aqueous environments described above and along the aminosilane gradients, the local dielectric constant is likely too small to support full transfer of a proton to the dye. Rather, it is expected that Nile Red will interact with acids under these conditions by forming a hydrogen bond,[158] as has been described in previous studies of Nile Red interactions with fluorophenol in nonaqueous media.[159] Therefore, it is expected that interactions between acidic sites (i.e. silanol groups) along the gradient and the dye will involve the sharing of a proton through a hydrogen bond. Figure 4.4 shows a schematic depiction of this interaction. Although complete transfer of a proton is not

expected, the process will be characterized as protonation or deprotonation of the dye for simplicity in this work.

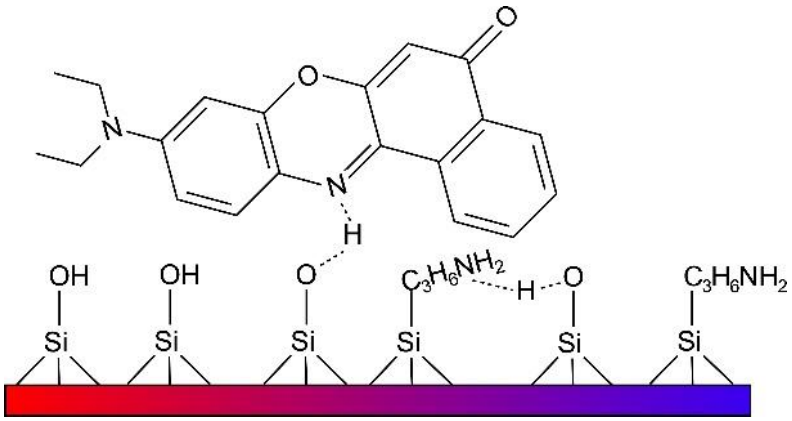

Figure 4.4 Possible hydrogen bonding interactions (dashed lines between atoms) along the aminosilane gradient. These interactions occur between acidic silanol sites and the basic Nile Red dye and also between acidic silanols and basic amine groups on the gradient

4.3.3 Single molecule spectroscopic imaging.

Single molecule detection and spectroscopic imaging using the Nile Red dye provides a valuable means to further characterize the acid/base properties of the aminosilane gradients at much higher spatial resolution than was achieved by XPS. These experiments were performed by recording wide-field fluorescence videos along the length of Nile-Red-doped aminosilane gradients. Videos were acquired simultaneously in two separate spectral bands, spanning 580 ± 20 nm and 640 ± 20 nm, as was done in earlier single molecule studies of silica film polarity.[119,147] Figure 4.5 shows representative fluorescence images obtained at the top (high-amine end) and bottom (low-amine end) of the gradients. These depict the first frame in 50 frame long videos analyzed at each position. Each image incorporates several isolated fluorescent spots attributable to detection of fluorescence from single Nile Red molecules. Assignment of the spots to emission from individual molecules is supported by the extensive "blinking" (i.e., fluorescence intermittency) observed in the original videos

The fluorescence detected from individual molecules in the 580 nm and 640 nm bands varied significantly between individual spots in the data obtained. While many molecules appeared in both images (i.e., 580 nm and 640 nm), others were observed in only one image, emitting too weakly to be visible in the other. These characteristics were also found to vary with distance along each gradient. As shown in Figure 4.5, the molecules were generally brighter in 580 nm images acquired at the high-amine end (10 mm position). At the low-amine end (24 mm), they were frequently brighter in the 640 nm channel. In contrast to the solution-phase studies, no clear evidence of a decrease in quantum yield of emission from the dye was found towards the more-acidic, low-amine end of the gradient. The reason for this difference is unknown at present but may derive from a reduction in the rate of nonradiative decay in the more static environment of the gradient surface, compared to the solution phase. These initial observations provide strong evidence of variations in the local film environment probed by each molecule, whether due to acidity or polarity effects.

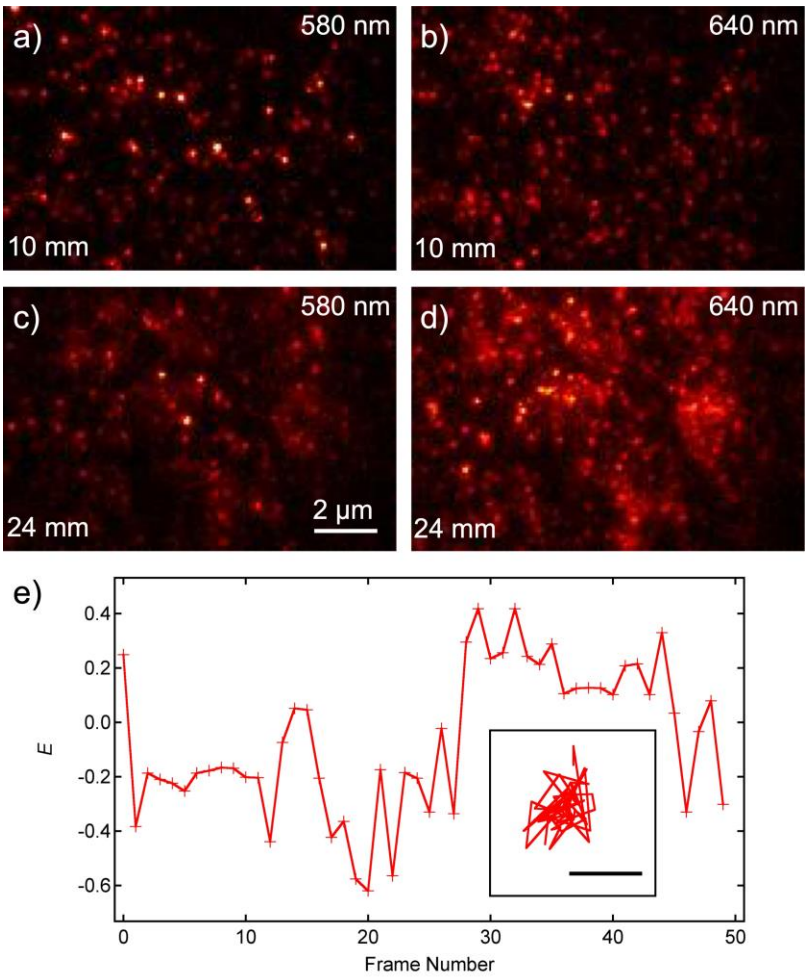

Figure 4.5 a)-d) Representative images of Nile Red on an aminosilane gradient. The color scale in each image depicts fluorescence counts ranging from 0 - 800 counts per pixel above background. e) Example time transient showing uncommon changes in E attributed to abrupt changes in protonation state of the molecule. This molecule was found in a video acquired at the 14 mm position along the gradient (see Figure 4.6). The inset shows the X,Y position of the spot across a 50 frame long video segment. The scale bar is 125 nm in length.

The video data also revealed characteristics of the molecules that help in understanding the spectroscopic results. As noted above, the molecules exhibited extensive fluorescence intermittency. However, the videos revealed little if any variation in the spectral characteristics of the fluorescence as the molecules blinked on and off. The video data also demonstrate that the molecules were largely associated with fixed sites along the gradient, moving little if at all, over

the ~ 30 s length of each video. These observations are generally expected as the films were imaged under a dry nitrogen atmosphere. They suggest that the local environment probed by each molecule changed little over the course of each video.

To better understand the properties of the local environment surrounding each molecule, a more quantitative analysis of the single molecule data was also performed. This involved precisely locating the individual spots in each of the 580 nm or 640 nm video frames, and linking the detected spots into time trajectories. For this purpose, the intensity profile of each spot was fit to a 2D Gaussian function, providing not only the spot location in X and Y, but also the spot amplitude, giving a direct measure of its intensity. The spot intensities were subsequently used to calculate the emission ratio, *E*, (see Eqn. 4.1) for each molecule along its time trajectory. Most such time trajectories revealed few clear variations in *E*, outside the measurement noise. Trajectory data from one rare counter example are shown in Figure 4.5 (bottom). In this figure, *E* is plotted for one molecule across the full length of the video segment in which it was found. These data show three apparent jumps in *E* between values of ~ -0.3 and ~ 0.2 occurring after frames 1, 27, and 44. The inset shows its spatial trajectory, which reveals that the molecule likely remains fixed on the gradient surface. The apparent variations in its location are attributable to the limited precision at which the molecule can be located σ_{xy} = 51 nm). These results indicate the local environment experienced by the molecule was either changing in time or the molecule was hopping on the gradient surface over distances much smaller than the localization precision.

The quantitative assessment of single molecule environments involved acquiring video data at 2 mm spacings along each gradient, beginning at the point from which data collection commenced, 10 mm from the original position of the deposition reservoir during gradient fabrication. This distance corresponds to 6 mm from the edge of the glass substrate. These data

were acquired out to a distance of 24 mm from the reservoir in each case. A total of five videos were collected from each location along the gradient at intervals spanning a 7.5 mm range across the gradient. Each experiment was performed on a total of four different gradients. The emission characteristics of thousands of individual Nile Red molecules were obtained and analyzed in these experiments. As noted above, the *E* values varied little outside measurement noise, so the mean *E* for each molecule along its trajectory was determined in each case and these mean values were then compiled into histograms depicting variations in the local environment. Histograms of the mean *E* values from the single molecules were first prepared for each position along and across each gradient. The histograms obtained from each of the five positions across each gradient were next summed together. Finally, those obtained at the same position along each of the four replicate gradients were subsequently summed. The compiled results are shown in Figure 4.6 and are displayed as a function of position along the gradients.

The distributions shown in Figure 4.6 reveal a general shift in the single molecule emission characteristics from negative *E* values at the high-amine end of the gradients (10 mm) to positive *E* values at the low-amine end (24 mm). As noted above, these results may reflect i) an increase in the polarity of the local environments, or ii) increased protonation of the Nile Red molecules, both occurring as a function of distance along the gradient. While the participation of both effects is likely, it is noteworthy that the distributions shown in Figure 4.6 are very broad compared to those obtained previously in similar studies of silica film polarity.[119,147] Moreover, the distributions shown in Figure 4.6 appear to be bimodal,[119] while monomodal distributions were observed in previous polarity studies, except when Nile Red was concluded to strongly interact with silanol sites on the silica surface.[147] The observation of broad, bimodal distributions in the present studies of acid/base gradients is therefore taken as good evidence of the response of Nile

Red to variations in the acidity properties of the film. While some contributions from variations in gradient polarity are certainly still present, acid/base effects are believed to dominate.

A simpler view of spatial variations in the properties of the local environments probed along the gradients was obtained by fitting the histogram data shown in Figure 4.6a-h to two component Gaussian distributions. A global fitting of these data was performed, with the data fit to distributions peaked at $E = -0.35 \pm 0.15$ (deprotonated Nile Red) and $E = 0.67 \pm 0.22$ (protonated Nile Red), with the error bars representing 95% confidence intervals. Limitations in the apparent quality of the individual fits may arise from the presence of more than two components in the distributions, because the distributions do not follow simple Gaussian statistics, or simply because of the limited number of measurements made. Nevertheless, an initial assessment of the gradient properties was obtained by using the amplitudes of the two components (A^- and A^+) to determine the fractional contributions of the protonated dye at $E = 0.67$ to the overall distribution. This analysis is similar to that performed for the XPS data Figure 4.2c, which plots the fraction of amine groups protonated at each position along the gradient. The results obtained from the single molecule data, calculated as $A^+/(A^+ + A^-)$, are plotted in Figure 4.6i. The plot obtained is remarkably similar to that shown in Figure 4.2c for the XPS experiments. Both show a dominant transition in gradient properties occurring between 10 and 15 mm along the gradient. It is concluded that the single molecule results depict predominantly the effects of a transition from unprotonated Nile Red dispersed on the gradient surface at the basic, high-amine end of the gradient (10 mm) to protonated Nile Red hydrogen bonded to silanol sites on the gradient surface at the acidic, low-amine end (24 mm).

The single molecule results were subsequently used to obtain high-resolution information on any spatial correlations in film properties. This analysis was performed to obtain a better

understanding of the spatial scale over which the acid or base characteristics of the gradient vary. In this analysis, the mean *E* value obtained from each single molecule was compared pairwise to the *E* values obtained from every other single molecule detected in the same video. Simultaneously, the distance between the pairs of molecules being compared was also determined. The latter was determined by taking the difference between the average molecular positions, as determined from their trajectories. Scatter plots depicting the differences in *E* (ΔE) versus the distances between the molecules (Δd) at each position along the gradient were then prepared by compiling all data obtained from each of the five videos acquired across each of the four replicate gradients. These results are shown in Figure 4.7a,b for the 12 mm and 22 mm positions.

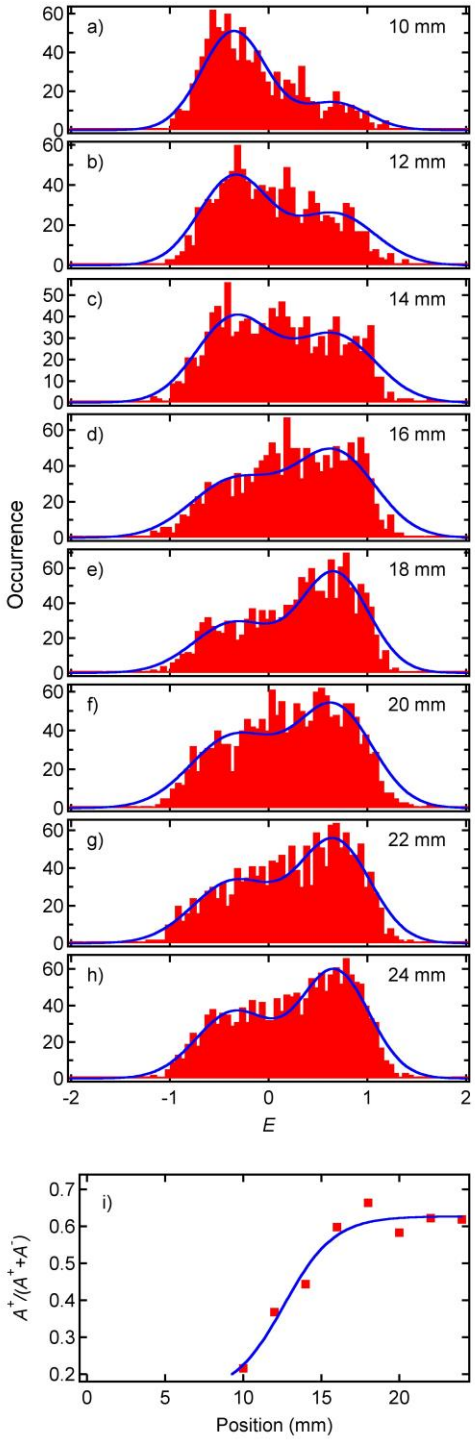

Figure 4.6 a)-h) Histograms depicting the single molecule emission ratio (red bars) as a function of position along the aminosilane gradient films and the fits of these distributions to two component Gaussian distributions (blue lines). i) Fraction emitting at hi high E, attributed to the protonated form of Nile Red (red squares) and a fit to the data (blue line) appended to better show the trend with position along the gradient.

The data shown in Figure 4.7a,b reveal that at large single molecule distances (i.e., $\Delta d > \sim 1$ μm), the E values obtained are completely uncorrelated with each other. However, at small distances (i.e., $\Delta d < \sim 1$ μm), they clearly become correlated, with the range of ΔE values obtained depending on the distance between molecules. To better depict these correlations, the ΔE values were boxcar averaged in 0.025 μm (Δd) wide bins. Figures 4.7c,d plot these results for the 12 mm and 22 mm positions. These results show that the average ΔE is very close to zero for closely spaced single molecules. Its value then increases gradually to a constant value of ~ 0.6 at distances $> \sim 0.5$ μm.

The observation of an average ΔE near zero for closely spaced molecules is clearly biased by the blinking of the molecules. Molecules that blink are interpreted as different molecules in the present analysis. Rather than attempting to deduce which data represent the same molecule counted multiple times and which are produced by different molecules appearing at approximately the same location at different times, the extent to which blinking molecules contribute to the observed correlation in E values was instead assessed by counting the number of molecules observed in each of the 0.025 μm wide bins. These data are plotted in Figure 4.7e,f. The plots show a peak in the number of molecules at $\Delta d = 0$, followed by a drop and then a subsequent rise in their numbers as Δd increases. The peak at $\Delta d = 0$ shows the expected artifact caused by blinking molecules being counted multiple times. Absent this artifact, very few if any molecules would be found at $\Delta d = 0$, assuming random positioning of the molecules. The number of molecules is expected to increase approximately linearly as Δd increases because the probability of finding two molecules at a distance Δd on a two-dimensional surface increases linearly with distance. Note that the apparent scarcity of molecules around $\Delta d = 0.5$ μm derives from a combination of the

artificially large number of molecules at $\Delta d = 0$ and the expected increase in number of molecules with increasing Δd.

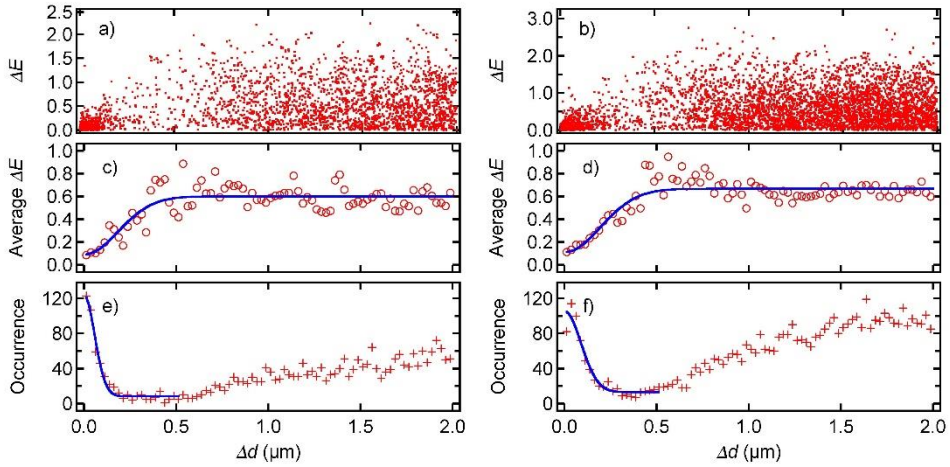

Figure 4.7 Difference in E (ΔE) between pairs of fluorescent spots as a function of their distance from each other Δd. a) Raw data compiled from 5 images acquired at 12 mm and b) at 22 mm along each of four different gradients. c) and d) Mean ΔE values as a function of separation between fluorescent spots. e) and f) Number of measurements along the gradients at the 12 and 22 mm positions. The large population near $\Delta d = 0$ is due to blinking of immobile single molecules. These results reveal a correlation in *E* values over distances of less than ~ 200 nm.

The width of the distribution obtained from blinking molecules (Figure 4.7e,f) near $\Delta d = 0$ reflects the precision at which the individual molecules can be located. A fit of each distribution in this region (see blue lines in Figure 4.7e,f) yield widths consistent with ~ 40 - 70 nm single molecule localization precisions along the gradient. Therefore, blinking alone should cause an apparent correlation in *E* values that decays over distances of ~ 60 - 100 nm. In fact, the correlations in *E* values depicted in Figure 4.7c,d, and at the other positions along the gradient (see Appendix A) all decay over two-to-three-fold larger distances. These results suggest that the acid/base properties of the gradients, as probed by the Nile Red molecules remain correlated over ~ 200 nm. The origins of such correlations are currently unknown, but may reflect the formation

of domains with different densities of amine or silanol groups on the gradient surface, or they may reflect the average distance over which surface bound amine groups can interact with silanol sites, altering their protonation states. They are not expected to derive from the finite localization precision of the single molecule measurements, because of the differences in the observed spatial extents of the artifacts due to blinking molecules in Figure 4.7e,f and the observed decay of the correlation in *E* shown in Figure 4.7c,d.

As a final point, it should be noted that the acid and base strengths expected for the materials investigated are consistent with the interpretations given above. While the pK_a values of protonated organic amines are typically ~ 10.5,[160] surface-bound ammonium groups have been found to be much more acidic, with $pK_a \sim 7$.[131] Likewise, the pK_a of surface silanol groups have been shown to fall in the range of ~ 4.5 - 8.5, with the majority of such sites having $pK_a \sim 8.5$.[161] Finally, while the pK_a of protonated Nile Red is difficult to determine because of its limited water solubility, it is likely somewhat more acidic than the pyridinium ion (pKa ~ 5.2).[157] The results reported in this work suggest that the amine groups should effectively compete for protons at the high-amine end, while at the low-amine end, it is the most acidic silanol sites that interact with the Nile Red molecules.

4.4 Conclusions

In summary, the application of Nile Red in single molecule spectroscopy studies of the local properties of bifunctional acid-base silica film gradients has been demonstrated for the first time. These studies rely upon the demonstrated response of Nile Red to the acidity of its local environment, rather than its usual solvent polarity dependence. The single molecule results were shown to be consistent with XPS mapping data obtained along similar gradients. The results show that the acidity/basicity properties of aminosilane gradients are dominated by the basic amine

groups at the high-amine end of the gradient and by acidic silanol sites at the low-amine end. Based on the XPS data, the fraction of protonated amine groups on the gradient surface was shown to increase running down the gradient as the density of acidic silanol sites increased. Likewise, based on the single molecule results, the fraction of protonated Nile Red molecules was also found to increase from the high- to low-amine ends of the gradient. Using the ability to locate the single molecules with ~ 50 nm precision, spatial correlations in the acidity/basicity properties of the aminosilane gradients were shown to occur over ~ 200 nm length scales. These correlations were concluded to reflect either the appearance of domains on the gradient surface or the distances scales over which amine groups and silanol groups interact with each other in determining surface properties. The methods and results of this study will be useful in gaining a better understanding the nature of bifunctional acid-base silica films used in catalytic chemical reactions such as ubiquitous aldol condensations.

Chapter 5 - Single Molecule Studies of the Aldol Condensation of Nile Red Aldehyde with Silica-bound Acetophenone.

5.1 Introduction

The chemical composition of catalysts, their structure, and sites' accessibility are responsible for their performance in reactions. Various methods exist for the detailed structural characterization of the surfaces of inorganic catalysts including x-ray microscopy, electron microscopy, and scanning probe methods.[67,162,163] but they are not suitable for organic reactants or surfaces. The bulk techniques used for organic surfaces such as mass spectroscopy or chromatography provide sub-millimeter spatial resolution.[164] Some of these methods can be used to study product formation in reactions, but since they are ex-situ, they don't produce crucial dynamic information.[67,163]

Fluorescence spectroscopy has emerged as an alternative or companion technique to existing methods to help link catalytic activity to local catalyst properties. Many techniques such as photoactivated localization microscopy (PALM),[143,165] stochastic optical reconstruction microscopy (STORM),[166,167] and nanometer accuracy by stochastic chemical reactions (NASCA)[164,168] have been used to reconstruct super-resolution images of the surfaces of catalysts with nanometer spatial resolution. One such method involves the use of fluorogenic probe molecules.[52,66,169] These are non-fluorescent dyes that show a dramatic shift in the absorption spectra - with a corresponding change in their quantum yield when they undergo chemical reactions. They switch from non-emissive to emissive states. These methods involve the localization and accumulation of reactant positions over consecutive frames to obtain high-resolution optical images. The catalytic turnovers can be obtained by counting the fluorescent "events" for a selected area on the catalyst during a certain time interval.[55,62,164,168,170]

Often, there are no commercially available fluorogenic reactants to quantify local reaction rates, so "spectator" fluorophores are used.[171] In this case, only the surface of the catalyst can be studied. The fluorophores do not participate in the reaction but can be used to observe physisorbed or chemisorbed species close to the glass-liquid interface. This method involves the use of TIR mode in wide-field microscopy. The appearance of one fluorescence signal indicates a surface binding event which may be the formation of a covalent bond. This method has been successfully used to study many chemical reactions, bridging the gap between the static physical features of the catalysts and their dynamic chemical reactivity.[171–173]

In this study, we explored the use of a fluorescent Nile Red derivate incorporating a reactive aldehyde - 9-diethylamino-5H-benzo[α]phenoxazin-5-one-2-carboxaldehyde (NR-CHO) to study an aldol condensation of the dye with acetophenone-bound silica compounds over amine-functionalized silica catalysts. The aldol condensation of this dye with acetophenone or acetone has been studied using fluorescence ensemble methods.[174] It was observed that there is a blue shift in the emission spectrum of the dye when the aldol addition or condensation products were formed, and this shift depends on the nature of the catalyst used. The fluorescent reactants and products were readily excited by 532 nm laser light, and the change in the fluorescence intensity/emission maximum with time provided a semi-quantitative measurement of the number of products formed.[174]

Here, we first synthesized hybrid silica films with tetramethoxysilane (TMOS) and phenyltrimethoxysilane (PTMOS) precursors and then carried out an acylation reaction on the PTMOS-TMOS to form silica-bound acetophenone. Further, a gradient layer of aminosilane was deposited on the films using a vapor phase deposition method to provide basic sites to catalyze aldol condensation. The surface-bound acetophenone should react with NR-CHO in the presence

of amine groups, providing the means to follow an aldol condensation reaction in-situ with single molecule spectroscopy. Such a capability has not been previously demonstrated in the literature. A scheme of this surface reaction is shown in Figure 5.1.

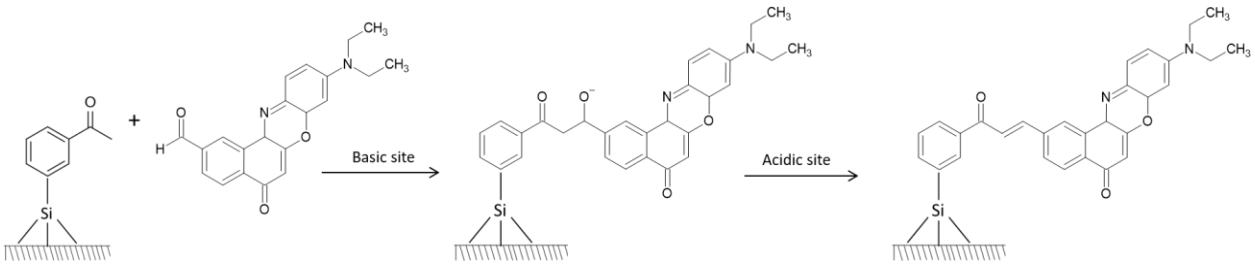

Figure 5.1 A schematic representation of the aldol condensation of surface-bound acetophenone with Nile Red aldehyde (NR-CHO) over silica catalyst films with amine gradients

5.2 Instrumentation

The thickness of the films was measured using spectroscopic ellipsometry as described in Chapter 3.

Fourier transform infrared absorption spectra were recorded in ATR mode using a Cary 630 (Agilent) spectrometer. The spectra were recorded from 4000 to 400 cm^{-1} at a resolution of 4 cm^{-1}. Thick PTMOS-TMOS films (1-1.5 μm) were used for the IR experiments. The films were removed using a clean razor blade and placed on the ATR diamond crystals. The FTIR measurements were repeated after the acylation to confirm the introduction of carbonyl functionality in the silica films.

The aldol reactions were performed on a wide-field epi-fluorescence microscope set-up that has been described previously.[47,50,119] The laser excitation was provided by a 532 nm laser light. It was elliptically polarized and directed through a spinning optical diffuser, reflected from a dichroic beam splitter (Chroma 555, DCLP). The excitation beam was focused onto the back aperture of a 1.49 NA 100X oil immersion objective (Nikon Apo-TIRF) to excite the dye molecules doped in

the samples. The epifluorescence signal was then collected by the same objective and separated from the excitation light by passing through the same dichroic beam splitter and a 550 nm colored-glass long pass filter. The emission signal was split into two separate spectral bands (640 ± 20 nm and 580 ± 20 nm) using an image splitter (Cairn Research Optosplit II) which has a second dichroic beam splitter (Chroma 610, DCLP). The fluorescence spectra in the two bands were detected simultaneously by a CCD camera (Andor iXon DU-897). The videos were taken at 0.5s exposure time and were 100-1080 frames long. The time interval between each frame was about ranged from 600 ms to 10 s.

The dye molecules in the reaction cells were excited, and the fluorescence was collected and split into two spectral bands centered at 580 nm and 640 nm. The videos were analyzed by a LabView program developed in-house. The program was used to locate each diffraction-limited fluorescence spot in the two spectral channels. The spots were fit to 2D Gaussian functions for better spatial resolution by determining the peak amplitude of each spot and its location. The spatial resolution of the experiment was resolved to ~50 nm using this method. The peak amplitudes were recorded as the fluorescence intensities. The change in fluorescence intensity as a function of frame number (time) was used to quantify the number of products formed.

Also, we obtained reactivity maps by localizing the spots and summing over many frames to show all the reaction events that occurred during the entire reaction time using the super-resolution optical fluctuation imaging (SOFI) method in Localizer.[166] This SOFI method uses the statistical analysis of temporal fluctuations in consecutive fluorescent images to provide background-free images with better resolutions.[168] The difference in fluorescence activity at different sections of the films indicate differences in catalytic reactivity, with bright domains corresponding to high catalytic turnovers.[168] In the videos, the fast-moving dye molecules are probably on the surface of

the films, while the immobile ones are strongly adsorbed within the film pores.[67] In the present study, a completed aldol condensation reaction is one in which the emission changes color.[175] This method has been used to study the epoxidation of a yellow fluorescent 4,4-difluoro-4-bora-3a,4a-diaza-s-indacene (BODIPY) dye with *m*-chloroperbenzoic acid (mCPBA) to form a green fluorescent product.[175] This blue shift in emission maximum was attributed to a shortening of the chromophoric unit after the reaction.[175]

5.3 Materials and Methods

A silica base layer containing phenyl groups was synthesized by the hydrolysis and condensation of two organosilane solutions, (TMOS) and phenyltrimethoxysilane (PTMOS). The sols contained 5-60% PTMOS (v/v) and they were spin-cast on microscope coverslips. The coverslips were cleaned with water and acetone followed by cleaning in air plasma for 6 min. The films were aged for at least 24 h before further use. Carbonyl functionality was introduced into the material by an acylation reaction of the surface of the PTMOS-TMOS films with acetyl chloride. First, aluminum chloride and dichloromethane were charged into a modified round bottom flask followed by the dropwise addition of a mixture of acetyl chloride and dichloromethane. The reaction was stirred at 0°C under reflux until all the catalysts had been used up. The TMOS-PTMOS films were then immersed into the reactor and the reaction mixture was stirred for 25 mins. The stirring was stopped, and the films were kept in the solution for 1 h. The films were immersed in a dilute solution of hydrochloric acid and rinsed with ice-cold water to remove the aluminum chloride from the reaction intermediate complex and liberate the ketone. This was followed by three rounds of washing the surface with water and ethanol to remove loosely bound reactants and other surface impurities. They were then dried in a desiccator until further use. An aminosilane gradient was

deposited on the acetophenone-bound silica films by using the directional vapor phase method described in Chapter 4. The films were placed in a vacuum desiccator overnight before further use. A schematic representation of the acylation reaction is shown in Figure 5.2.

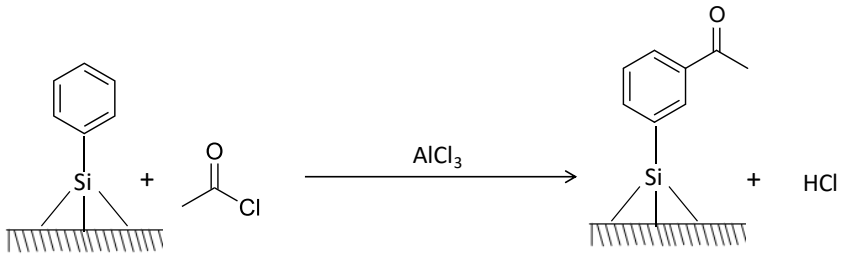

Figure 5.2 Acylation reaction of hydrolyzed PTMOS and acetyl chloride

Hollow glass cylinders with internal diameters of 7.5 mm and 10 mm high were cut from glass tubes. They were rinsed with water and ethanol, sonicated for 10 min, and dried at 40°C. They were subsequently plasma-cleaned for 5 min. The reaction cells were assembled by attaching the cleaned glass cylinders to the coverslips by applying glass glue to the outer base of the tubes. The set-up was allowed to stand for 30 min before further use. 150 μL aliquots of 1-10 nM ethanolic solutions of the Nile Red aldehyde dye were then added to the cells on the wide-field microscope, and the fluorescence emission was collected after excitation.

5.4 Results and discussion

5.4.1 Film thickness

The average thickness of the 10% PTMOS-TMOS films was measured to be 52.6 ± 0.34 nm while the thick 60% PTMOS-TMOS films used for the IR experiments were 1200 ± 250 nm thick. After acylation, the average film thickness of the 10% PTMOS-TMOS and 60% PTMOS-TMOS films remained relatively unchanged at 52.8 ± 0.53 nm and 1175 ± 200 nm respectively. These

measurements were carried out on different portions of the films. They indicate that the films were stable, and the acylation reaction and solvent wash do not remove the thin layers deposited.

5.4.2 Acylation reaction

FTIR spectroscopy was the only method used to verify the success of the acylation reaction in adding a carbonyl functionality to the phenyl groups on the silica surface. One spectrum for the unreacted PTMOS-TMOS film was recorded. Three spectra for the acylated films were recorded as a function of reaction time, and one spectrum of the film reacted in the absence of aluminum chloride was recorded as a control. These are shown in Figures 5.3 and 5.4. In all the spectra, the symmetric stretching vibration of Si-O-Si was seen at around 1040 cm^{-1},[176] while the broad absorption band around 3275 cm^{-1} is due to the OH stretching vibrations.[176] After acylation, a peak at around 1648 cm^{-1} appears. This peak is assigned to carbonyl (C=O) of aromatic ketones.[177] The extent of conversion of the phenyl groups to acetophenone can be seen to depend on the reaction time; the surface functionalization increases with reaction time. In Figure 5.4, the absence of a carbonyl peak at 1648 cm^{-1} for the unreacted PTMOS-TMOS films and those reacted in the absence of $AlCl_3$ give further evidence of the success of the reaction. 1 μm thick films were used for these experiments to ensure the collection of sufficient material required for recording well-defined spectra on the ATR-FTIR spectrometer. For single molecule experiments, considerably thinner films (~ 55 nm) were used, with a reaction time of 1h 35 mins. It was not possible to remove these films to record the spectra, but we can safely expect an even higher degree of surface functionalization compared to the thick films because of the increased surface contact with the reactants and catalysts.

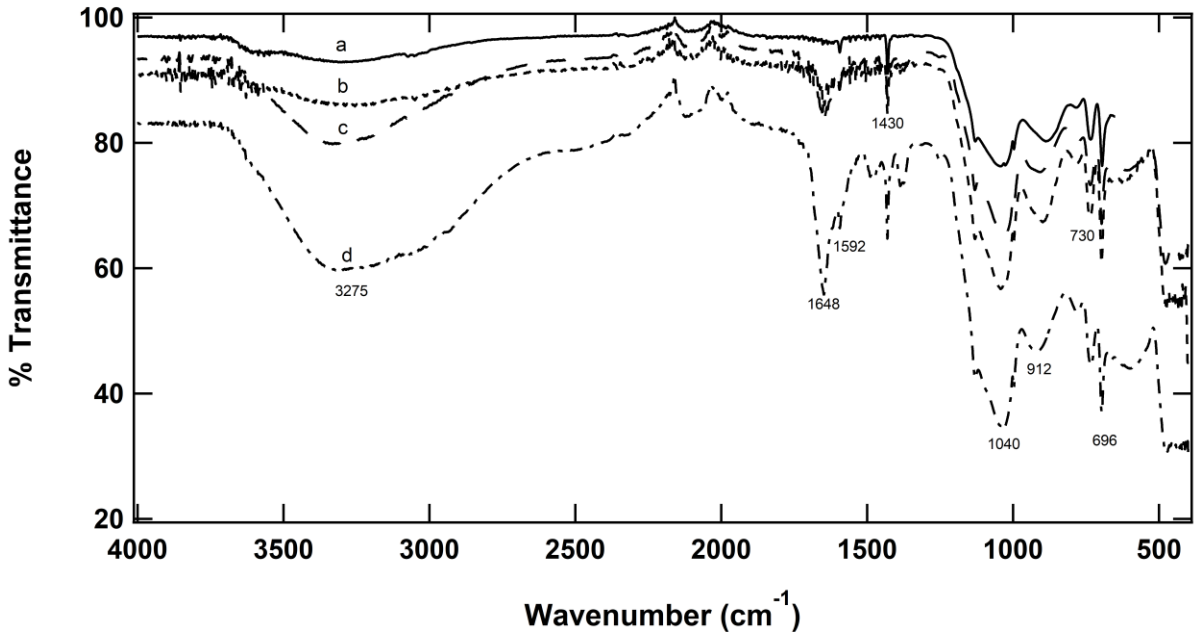

Figure 5.3 FTIR spectra of (a) 60% PTMOS-TMOS film, (b) 60% PTMOS-TMOS film after 35 min acylation, (c) 60% PTMOS-TMOS film after 1h 35 min acylation, and (d) 60% PTMOS-TMOS film after 3h 35 min acylation

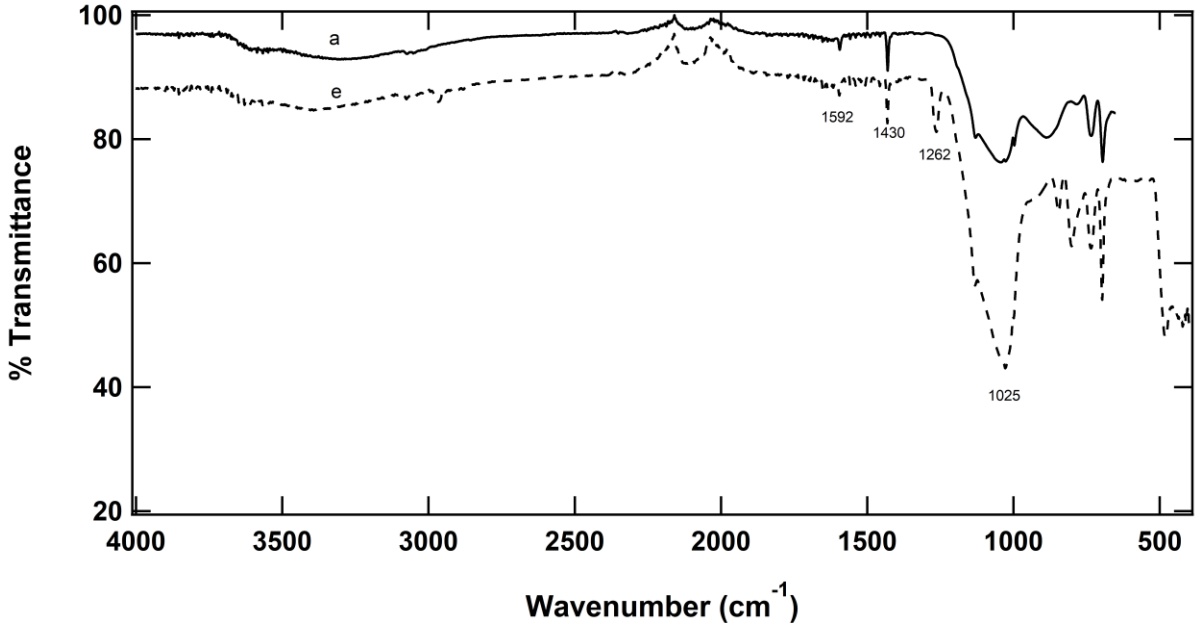

Figure 5.4 FTIR spectra of (a) 60% PTMOS-TMOS film, (e) 60% PTMOS-TMOS film reacted overnight in the absence of aluminum chloride.

5.4.3 Single molecule reactions

First, the substrates were prepared as described above. This was followed by the attachment of the reaction cells. The films had 5-50% PTMOS. In a previous SM study of organometallic reaction mechanisms, the reaction solution was photobleached for 5 minutes to decrease the probability of finding more than one single molecule in a field of view.[178] In this study, before starting the experiments, the PTMOS-TMOS surface was photobleached for ~45s to remove some of the fluorescent impurities remaining on the film surface after synthesis. The acylated film was subsequently excited, and videos were recorded for ~ 1 min to serve as the blank films. HPLC ethanol was then added to the reaction cell, and the fluorescence was collected for 50 minutes. Finally, concentrated NR-CHO was added to the solution in the cell to make a total NR-CHO concentration of ~ 2 nM. The fluorescence videos were recorded for 0.8 - 3 hours. In some of the experiments, the ethanol solution was simply replaced with the desired dye concentration for the aldol condensation reaction.

Based on ensemble experiments, we expect the fluorescence to shift to shorter wavelengths because of aldol condensation product formation.[174] One method of tracking these changes is by following the intensity trajectories of single dye molecules in both spectral bands and measuring the relative decrease or increase in the emission intensities at two different wavelengths as a function of time. Also, fluorescence bursts may indicate the formation of a new product. The starting material for the aldol reaction, NR-CHO, photobleached rapidly, as did its addition or condensation products, hence only short trajectories could be recorded. These trajectories are shown in Figure 5.5. The emission ratio, E is defined as $E = I_{580}/I_{640}$.

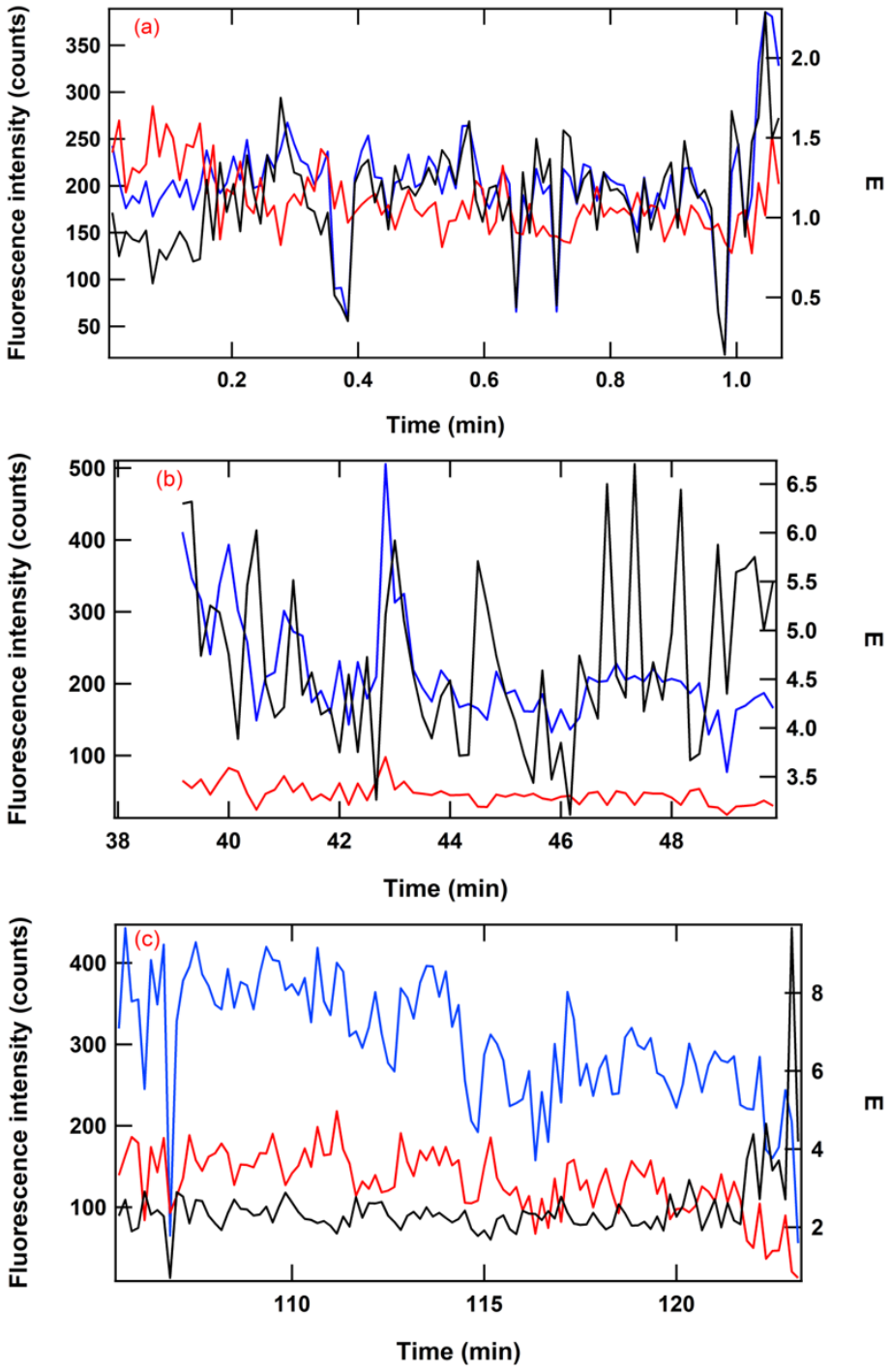

Figure 5.5 Fluorescence intensity trajectories for (a) blank Si-bound acetophenone films (b) Si-bound acetophenone films with ethanol (c) aldol condensation of 2nM NR-CHO with Si-bound acetophenone. The blue lines represent fluorescent intensity from the 580 nm channel, red is from the 640 nm channel and the black lines are the emission ratios (E)

The selected trajectories shown in Figure 5.5a and 5.5c indicate a near-constant fluorescence intensity in both channels for all the recorded videos, while the emission ratio varies significantly in Figure 5.5b. But a visual inspection of the videos shows that the fluorescence intensities in both channels, especially for the aldol reaction, increase as a function of time and then drop off due to photobleaching or diffusion of the reactants/products into the non-excited solution. They also show significant red and blue shifts compared to the starting solutions. These changes were measured by using a qualitative analysis of the fluorescence emissions.

After collecting the videos, the individual dye spots were localized with ~ 50 nm spatial resolution as described in Chapter 4. Then, the total fluorescence events occurring during the three experiments were summed together using SOFI analysis in Localizer. Here, accumulated fluorescence emission images as a function of frame number were produced. The SOFI method accounts for the photobleached fluorescence spots which could not be linked into trajectories, and they produce a "reactivity map." This map shows how the fluorescence intensities change during the reactions as a function of time. These results are shown in Figure 5.6. One pixel = 0.08 μm in all the images, and the brightest spots represent the most fluorescent dye molecules. The three films had aminosilane gradients on them.

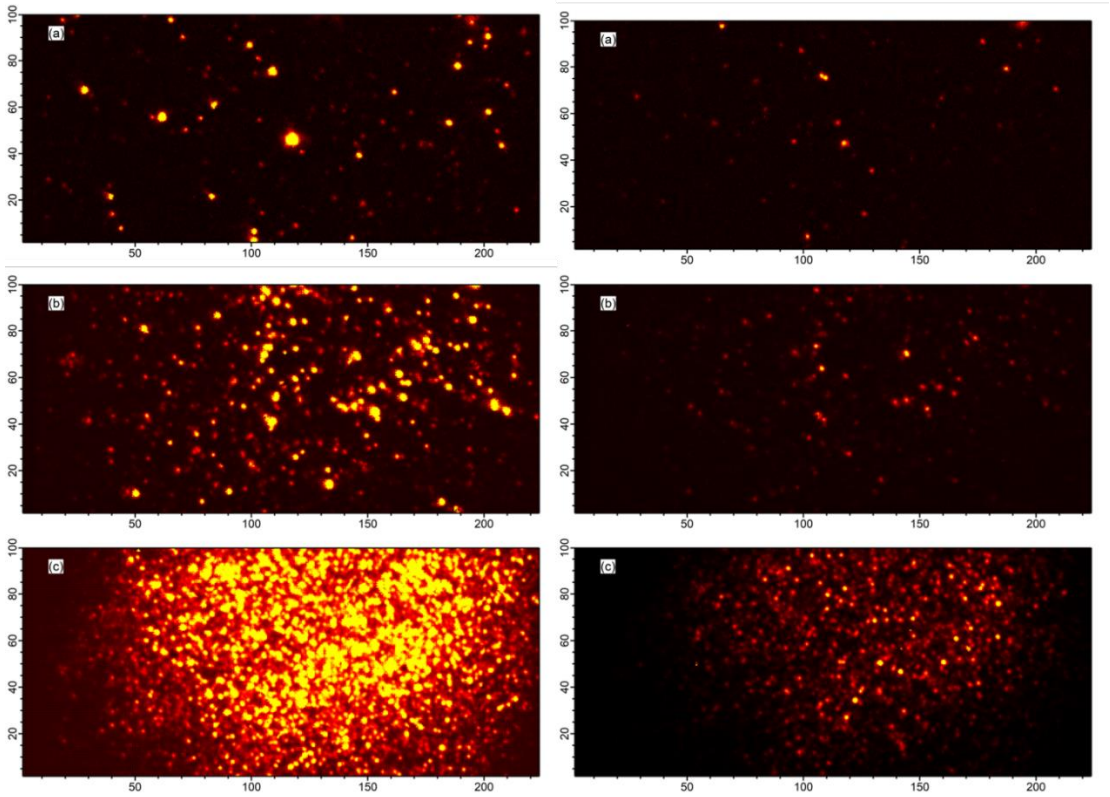

Figure 5.6 Accumulated fluorescence emission images in the 580 nm spectral channel (left) and the 640 nm spectral channel (right) for (a) blank Si-bound acetophenone films (b) Si-bound acetophenone films with ethanol (c) aldol condensation of 2nM NR-CHO with Si-bound acetophenone. The axes are measured in pixels.

On adding the NR-CHO to start the aldol condensation, the fluorescence intensity was found to increase significantly in both spectral bands which is different from what was observed for ensemble fluorescence measurements where the addition/condensation products emitted at shorter wavelengths.[174] Currently, we have not devised a means to measure the relative increase in fluorescence for this two-color imaging study. A qualitative study of the fluorescence intensities as a function of time was carried out, and the results for a 2-hour reaction are shown in Figure 5.7 for the aldol reaction. On introducing the dye, the fluorescent spots in both channels were few. After 30 minutes, the number and intensity of spots in both channels increased significantly, either due to the adsorption of the fluorescent NR-CHO on the surface or the formation of a new species

which emits at slightly different wavelengths. The number of fluorescent events increases with time, and after around 90 mins, fewer fluorescent bursts or shifts were observed which may indicate a decrease in surface reactivity due to a reduction in the number of accessible acetophenones for reaction.

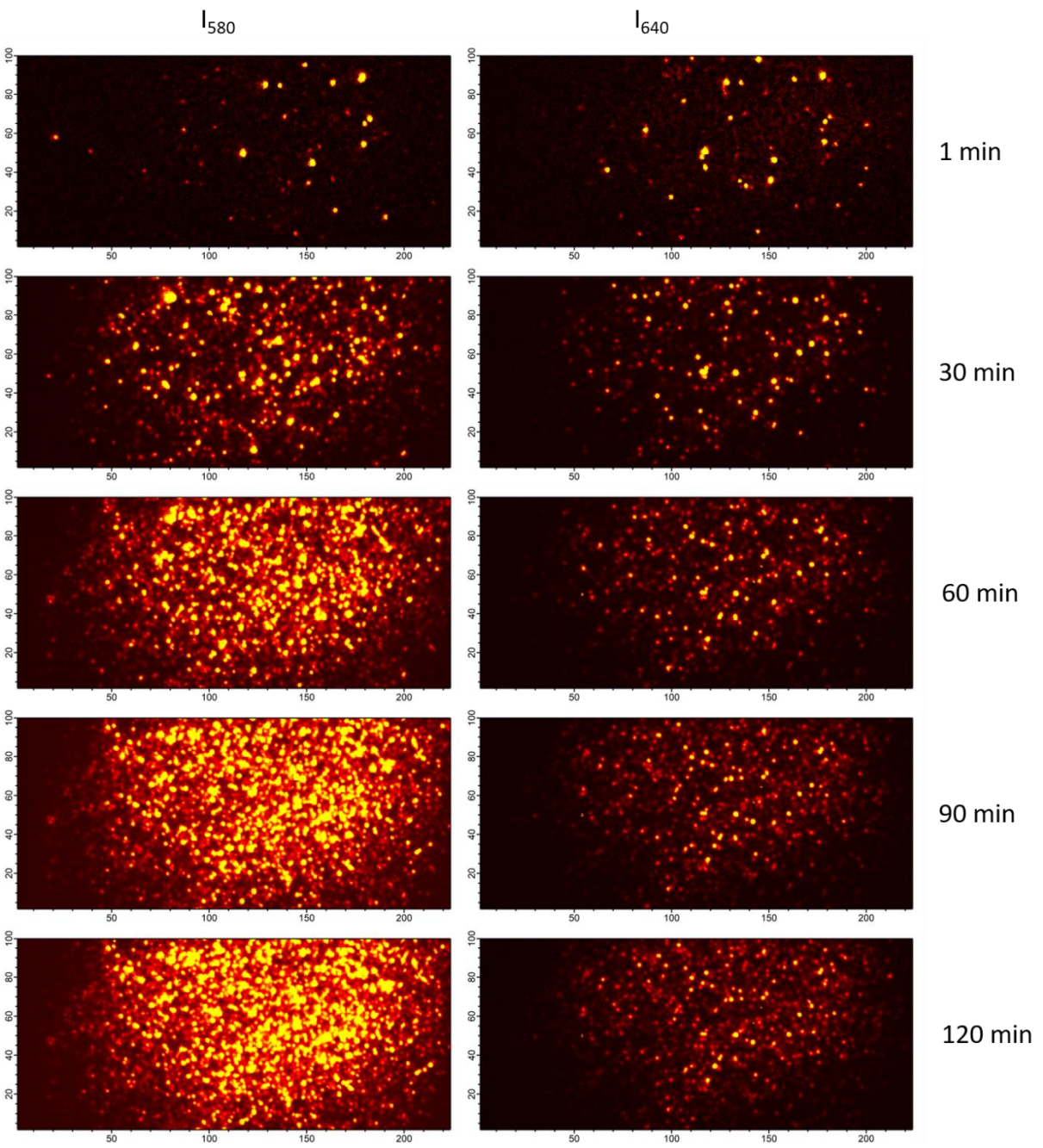

Figure 5.7 Accumulated fluorescence emission images in the 580 nm spectral channel (left) and the 640 nm spectral channel (right) the aldol condensation of 2nM NR-CHO with Si-bound acetophenone as a function of reaction time. The axes are measured in pixels.

A controlled study using 2 nM of a non-reactive dye, NR, was carried out using the same reaction system above. The reactivity maps (Figure 5.8) show fewer fluorescent events compared to NR-

CHO which indicates fewer binding events of NR to the substrates and/or little chemical reactivity. The fluorescence emission is almost constant with time. Also, since the observed fluorescence emission does not significantly increase with time, it is most likely due to surface-adsorbed NR molecules, and the increased fluorescence seen for the aldol reaction in Figure 5.7 is because of new chemical species produced by the aldol reaction.

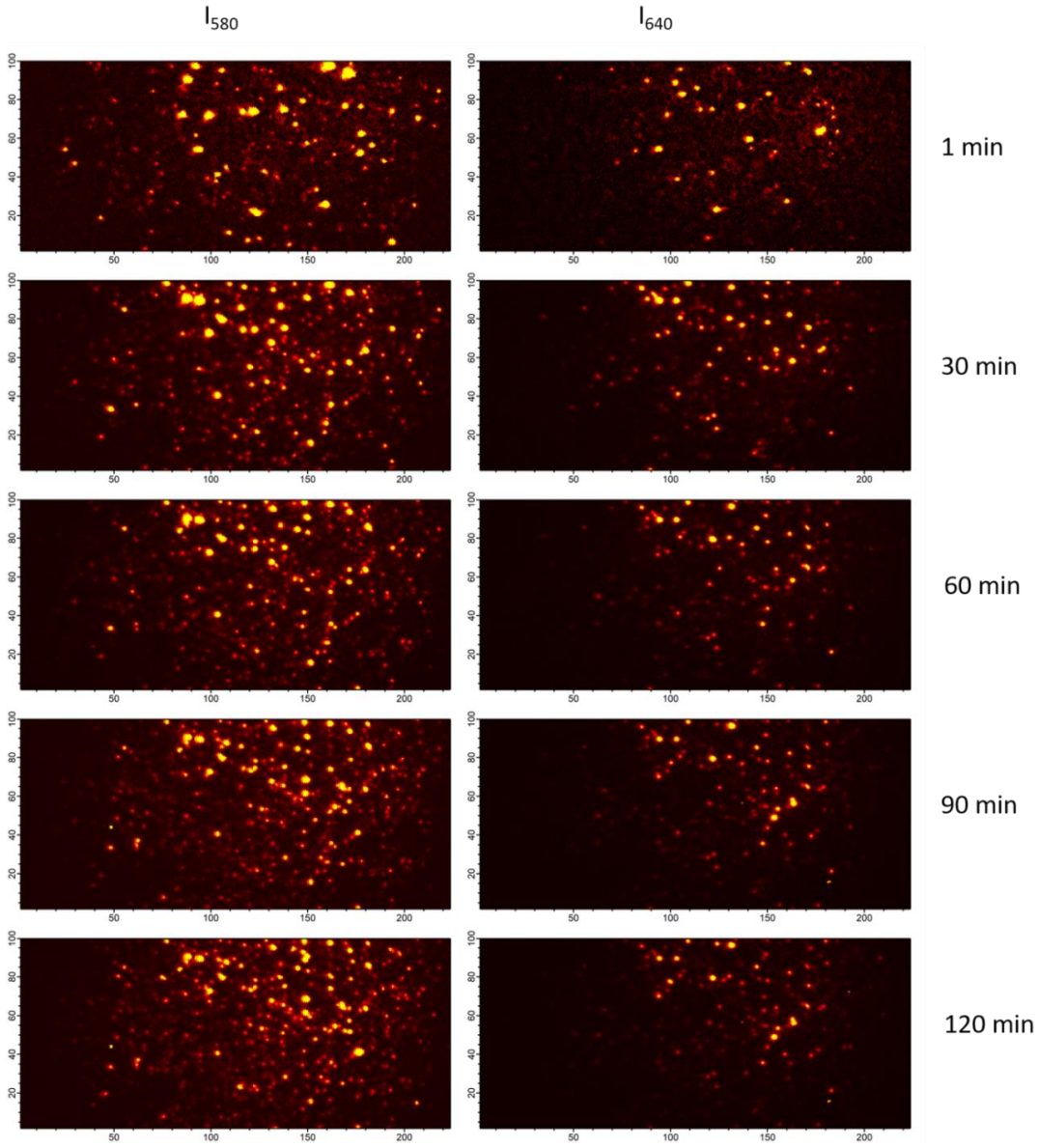

Figure 5.8 Accumulated fluorescence emission images in the 580 nm spectral channel (left) and the 640 nm spectral channel (right) the reaction of 2nM NR with Si-bound acetophenone as a function of reaction time. The axes are measured in pixels.

To observe the effect of dye concentration on the fluorescence activity, these experiments were repeated using 2nM, 5nM, and 10nM NR-CHO. The accumulated reactivity maps for the three NR-CHO concentrations after 1h are shown in Figure 5.9. Here, we observed an increase in the number of fluorescence events for 10 nM NR-CHO relative to 2 nM NR-CHO, while the reactivity was lower for 5 nM NR-CHO. The fluorescence activity should increase with dye concentration, but this was not the case here, probably because of sample-to-sample variations in the thin film preparations.

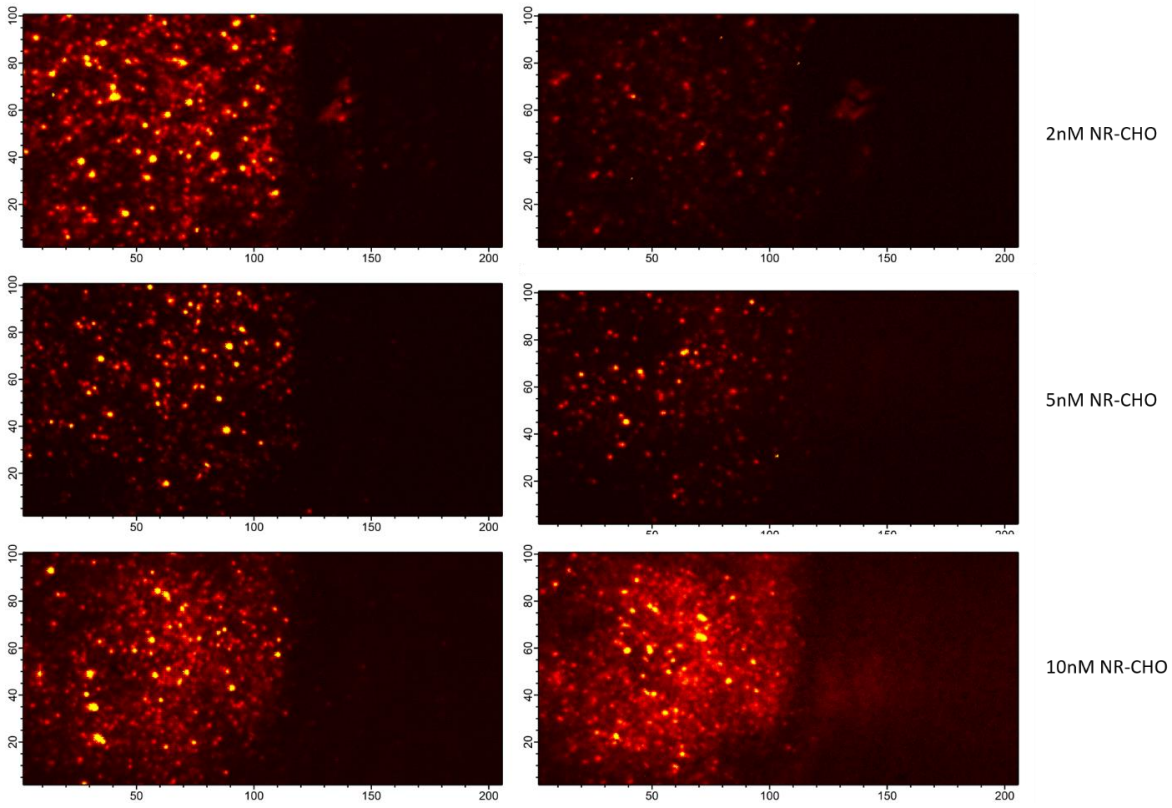

Figure 5.9 Accumulated fluorescence emission images in the 580 nm spectral channel (left) and the 640 nm spectral channel (right) for the aldol condensation different concentrations of NR-CHO with acetophenone after 1hr reaction. The axes are measured in pixels.

Next, we observed the effect of the density of acetophenone on the silica surface on the overall chemical reactivity. The PTMOS loading was increased by a factor of 10 to 50% and the resultant reactivity maps were compared to the 5% PTMOS films (Figure 5.10). It was observed that the

substrates with a higher concentration of reactive silica-bound acetophenone showed higher fluorescence reactivity which gives further evidence that the aldol reactions occurred on the surfaces. The relative fluorescence from the 640 spectral channel was also found to increase significantly with increasing PTMOS loading.

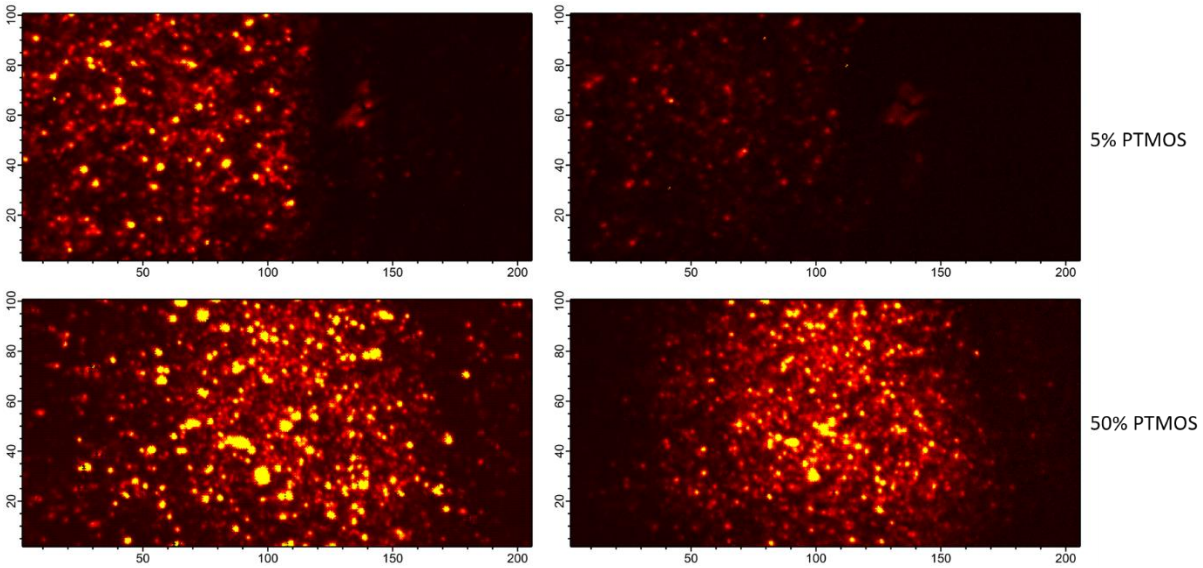

Figure 5.10 Accumulated fluorescence emission images in the 580 nm spectral channel (left) and the 640 nm spectral channel (right) for the aldol condensation of acylated films with different PTMOS loadings and 2nM NR-CHO recorded over 1h. The axes are measured in pixels.

The previous experiments were all carried out at the high-amine end of the substrates. Various studies have shown that aldol condensation reactions are best catalyzed by a combination of medium-strength basic sites and weak acid sites. To study the effect of the relative distributions of amine and weakly acidic silanol sites on the chemical reactivity, we carried out the aldol reactions at the high amine end of the gradient films, the middle section, and the low-amine end dominated by silanols. The high amine end roughly represents mostly basic sites, the middle section represents a mixture of basic and acidic groups, and the low-amine end represents mostly acidic sites. The results shown in Figure 5.11 show that the fluorescence activity (or aldol reactivity) is

highest in the middle section of the films followed by the high-amine end. The low-amine end showed the least reactivity. The amine gradient results are similar to previous works which showed that aldol reactions are best catalyzed by bifunctional catalysts with weak acid and medium strength basic sites.[23,108,112,126,179,180] These videos were recorded on the same gradient films.

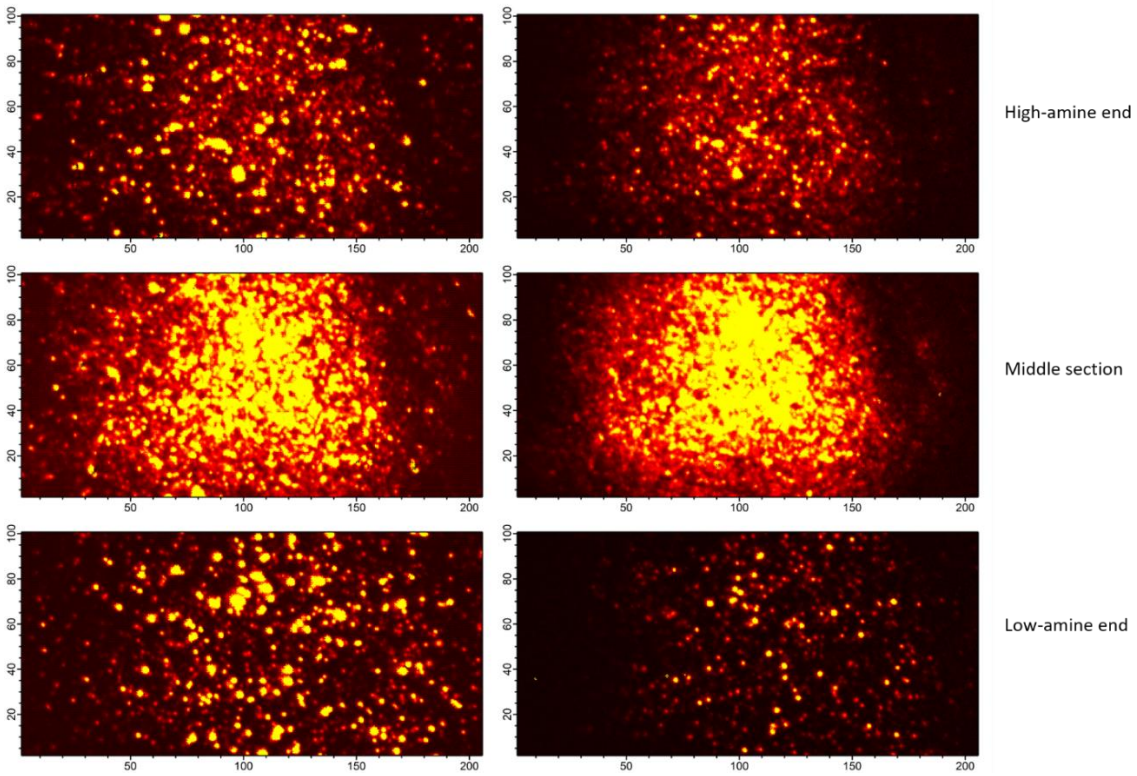

Figure 5.11 Accumulated fluorescence emission images in the 580 nm spectral channel (left) and the 640 nm spectral channel (right) for the aldol condensation of acylated films with 50% PTMOS loadings and 2nM NR-CHO recorded over 1h at different sections of the acid-base gradient. The axes are measured in pixels

A quasi-single molecule analysis was carried out to measure the changes in emission ratio ($E = I_{580}/I_{640}$) for the aldol reactions. Randomly distributed 2x2 pixels were selected as shown in Figure 5.12. This represents a 0.16 x 0.16 μm^2 area.

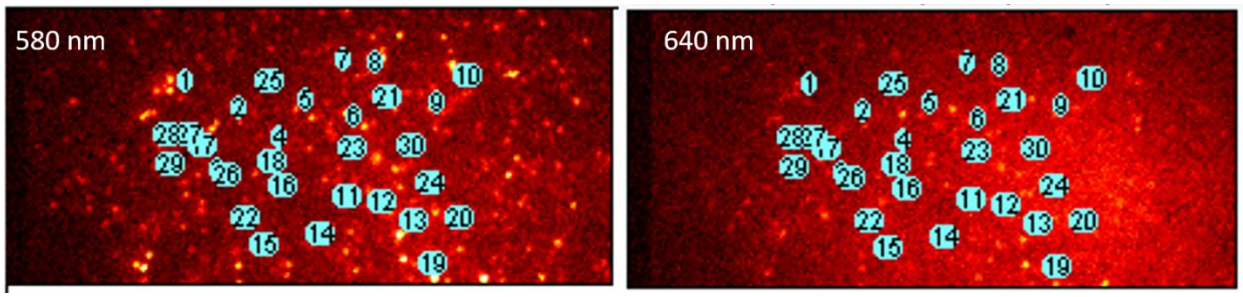

Figure 5.12 A representative image of the randomly selected 2x2 pixels for quantitative analysis.

The E ratios were plotted as functions of time. A representative plot is shown in Figure 5.13. In this work, a single molecule reaction or adsorption event is defined as occurring when there is a shift in E ratio of ≥ 0.2 units or ≤ -0.2. This threshold value was selected by observing the E trajectories for the aldol reaction samples with dye molecules and those without dyes.

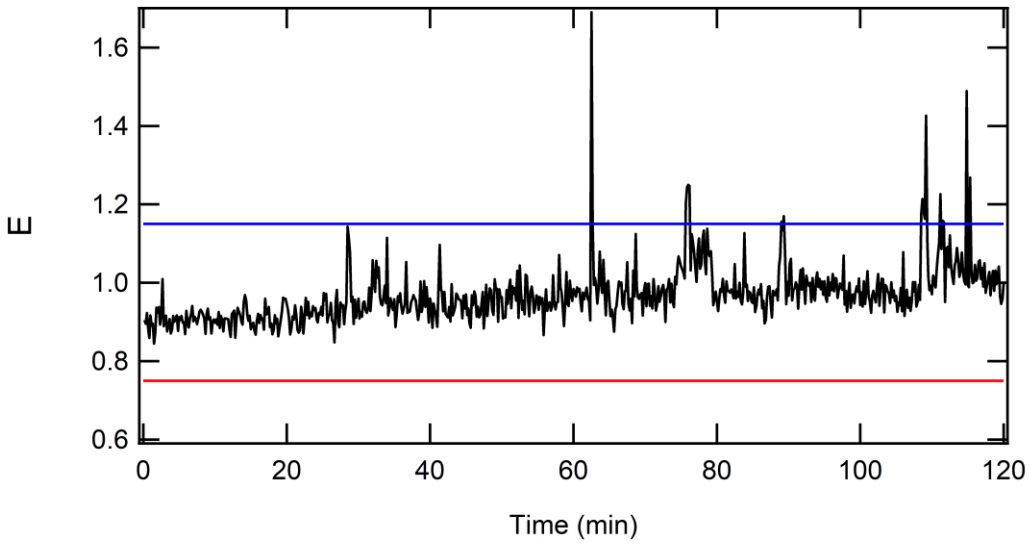

Figure 5.13 A plot of emission ratio vs time for an aldol reaction of acylated 5% PTMOS-TMOS films with acetophenone over amine gradients. The blue line represents the threshold for a shift to shorter wavelengths and the red line is the red shift threshold.

The emission intensities from both spectral channels (I_{580} and I_{640}) used to calculate the E in Figure 5.13, when plotted as functions of reaction time, show a quantized behavior as shown in Figure

5.14 and Figure 5.15. This response is an established fingerprint of the fluorescence from a single molecule. This indicates that there is at least a physical adsorption of NR-CHO molecules on the coverslip.

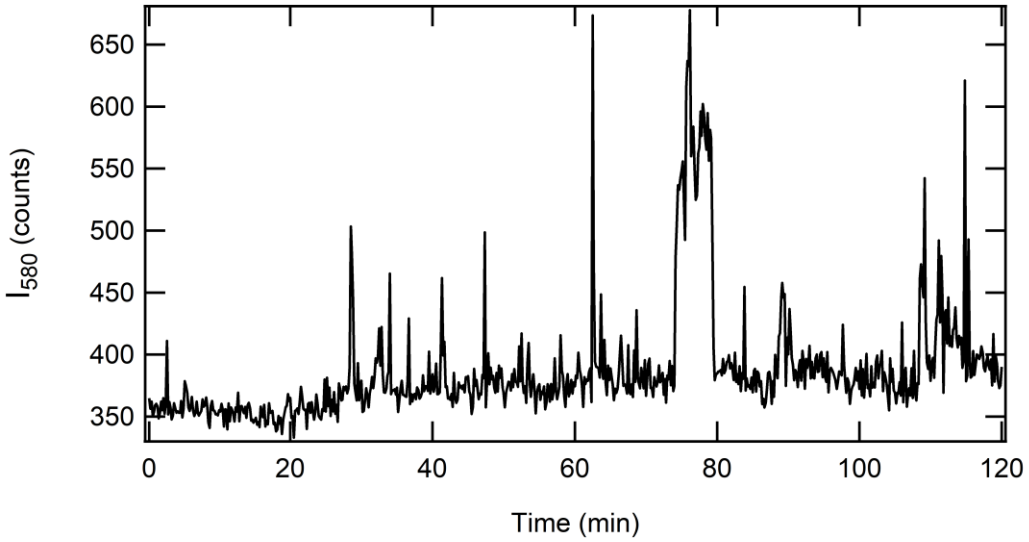

Figure 5.14 NR-CHO emission from 580 nm spectral channel as a function of time

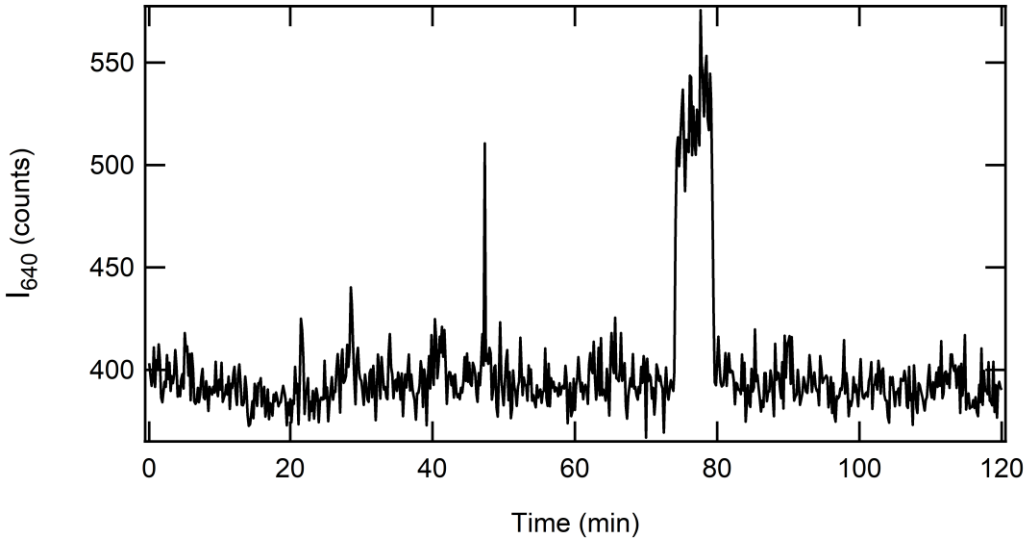

Figure 5.15 NR-CHO emission from 640 nm spectral channel as a function of time

Based on our definition of E, $\Delta E \geq 0.2$ represents an overall blue shift in fluorescence emission, while $\Delta E \leq -0.2$ represents a shift to longer wavelengths. The number of "fluorescence events" for each selected area from Figure 5.12 was manually counted and used to calculate the overall fluorescence reaction rate. For the aldol condensation of NR-CHO with silica-bound acetophenone carried out over amine-functionalized silica films, the reaction rate was 1.15×10^{-13} mol/m^2 s. On the silica films without amine gradients, the reaction rate was 1.3×10^{-14} mol/m^2 s. This indicates that the observed fluorescence shift is likely due to surface adsorption of the dye molecule and/or fluorescence from aldol condensation products. Hence, the overall fluorescence reaction rate can be used as an indicator of reaction rate. In control experiments using a non-reactive Nile Red under the same conditions as the above experiments, a reactivity rate of 2.7×10^{-14} mol/m^2 s was recorded on amine-functionalized films. The rate of reaction on silica films without the amine catalysts was 1.2×10^{-14} mol/m^2 s. In all the experiments, the reactivity rates at each of the 30 2x2 pixel areas were different across a gradient position.

5.5 Conclusions

Silica films incorporating acetophenone were synthesized and used for an aldol condensation reaction with a fluorescent and reactive NR-CHO dye. This reaction was catalyzed by a bifunctional acid-base gradient deposited as films on the substrates. A series of experiments showed that there is an increase in fluorescent intensity and a shift in fluorescent emission when NR-CHO either gets absorbed on the substrate or reacts with the surface acetophenone to form aldol products. However, the extent of reaction or nature of products formed could not be verified in the present study. Rather, reactivity/fluorescent maps were used for a qualitative analysis of the effects of NR-CHO concentration, the density of acetophenone, and the distribution of acidic/basic

sites on the aldol condensation reactions. A quasi-single molecule analysis of the recorded trajectories indicates that the fluorescent dyes may yield quantitative information on aldol reaction rates.

Chapter 6 - General Conclusions and Future Work

This dissertation shows the use of SM methods to probe the local acidity of two types of aldol condensation catalysts and the visualization of an aldol condition reaction at sub-micron resolution.

In chapter 3, the distribution of sites in films was studied using a pH-sensitive dye C-SNARF-1 This study showed that the probed dye can measure the apparent acidity of films between pH 3 and pH 6.2. It also showed that the fluorescence emission ratio of the dye depends on the amount of cesium loading and can thus be used to provide detailed distribution of local acidity on cesium modified silica films.

In chapter 4, a different catalyst system incorporating amine gradients was synthesized. The acidity distributions along the gradient film were studied using a commercial NR dye. The SM results revealed that the acid-base properties of the aminosilane gradients were dominated by the basic amine groups at the high amine end of the film, while the weakly acidic silanol groups dominate at the low amine ends of the films. Single molecule results also showed that the degree of protonation of Nile red molecules increases towards the lower amine end of the bifunctional catalyst films that have the highest amount of weakly acidic silanols.

In chapter 5, an aldol condensation reaction was carried out on a wide-field microscope at room temperature. The reaction of a Nile red aldehyde dye with acetophenone was carried out over the acid-base bifunctional catalyst films synthesized in chapter 4. Preliminary results show a clear dependence of the chemical reactivity on the distribution of acidity on these catalyst films.

Overall, this dissertation has demonstrated the use of an easy SM technique to study the nanoscale properties of catalyst films. This characterization method is intended to serve as a

complementary technique to more common methods of studying active sites such as temperature-programmed desorption methods and XPS.

A limitation in the study of single molecule reactions in bulk solutions is the ability to distinguish among fluorescent solvent/sample impurities, the reactant species. and the products formed Fluorescence from impurities are inevitable even with the best wide-field microscope configurations and meticulous sample preparation. So future works should use fluorogenic dye molecules that can undergo aldol condensation as one of the reactants. These dyes are convenient because they are not fluorescent and only exhibit a shift in the emission maximum when they form aldol addition or condensation products. This reduces the level of uncertainty in distinguishing between products and background fluorescence.

Also, while catalyst gradient films are useful for combinatorial material research and screening, they are not fully suited for single molecule reactions in solutions. This is because the physical limitation of the size of the coverslips used for this experiment limits the number of positions that can be studied along a gradient. Also, the reactions occurring at different points in the gradients cannot be studied simultaneously using the current microscopic method. It would be easier to use a series of catalysts with different amine-loadings. By using these acid-base films with a quantified number of amine groups, we can better correlate chemical reactivity with acidity distribution.

References

1. Langholtz, M. H., Stokes, B. J. & Eaton, L. M. *2016 Billion-Ton Report: Advancing Domestic Resources for a Thriving Bioeconomy*. http://www.osti.gov/servlets/purl/1271651/ (2016) doi:10.2172/1271651.
2. Perlack, R. D. *Biomass as Feedstock for a Bioenergy and Bioproducts Industry: The Technical Feasability of a Billion-Ton Annual Supply*. http://www.osti.gov/servlets/purl/885984-pH60fJ/ (2005) doi:10.2172/885984.
3. White, E. M. Woody biomass for bioenergy and biofuels in the united states- a briefing paper. *USDA For. Serv. - Gen. Tech. Rep. PNW-GTR* **825**, 1–45 (2010).
4. Bohre, A., Dutta, S., Saha, B. & Abu-Omar, M. M. Upgrading Furfurals to Drop-in Biofuels: An Overview. *ACS Sustain. Chem. Eng.* **3**, 1263–1278 (2015).
5. West, R. M., Liu, Z. Y., Peter, M., Gärtner, C. A. & Dumesic, J. A. Carbon–carbon bond formation for biomass-derived furfurals and ketones by aldol condensation in a biphasic system. *J. Mol. Catal. A Chem.* **296**, 18–28 (2008).
6. Chheda, J. N. & Dumesic, J. A. An overview of dehydration, aldol-condensation and hydrogenation processes for production of liquid alkanes from biomass-derived carbohydrates. *Catal. Today* **123**, 59–71 (2007).
7. Faba, L., Díaz, E. & Ordóñez, S. Aqueous-phase furfural-acetone aldol condensation over basic mixed oxides. *Appl. Catal. B Environ.* **113**–**114**, 201–212 (2012).
8. Subrahmanyam, A. V, Thayumanavan, S. & Huber, G. W. C-C Bond Formation Reactions for Biomass-Derived Molecules. *ChemSusChem* **3**, 1158–1162.
9. Sádaba, I., Ojeda, M., Mariscal, R., Richards, R. & Granados, M. L. Mg–Zr mixed oxides for aqueous aldol condensation of furfural with acetone: Effect of preparation method and

activation temperature. *Catal. Today* **167**, 77–84 (2011).

10. Lewis, J. D., Van De Vyver, S. & Román-Leshkov, Y. Acid-Base Pairs in Lewis Acidic Zeolites Promote Direct Aldol Reactions by Soft Enolization. *Angew. Chemie - Int. Ed.* **54**, 9835–9838 (2015).
11. Margelefsky, E. L., Zeidan, R. K. & Davis, M. E. Cooperative catalysis by silica-supported organic functional groups. *Chem. Soc. Rev.* **37**, 1118–1126 (2008).
12. Perrin, C. L. & Chang, K.-L. The Complete Mechanism of an Aldol Condensation. *J. Org. Chem.* **81**, 5631–5636 (2016).
13. Solomons, T. W. G., Fryhle, C. B. & Snyder, S. A. *Organic Chemistry, 12th Edition*. John Wiley and Sons (2016).
14. Faba, L., Díaz, E. & Ordóñez, S. Improvement on the Catalytic Performance of Mg–Zr Mixed Oxides for Furfural–Acetone Aldol Condensation by Supporting on Mesoporous Carbons. *ChemSusChem* **6**, 463–474.
15. Zhao, D., Huo, Q., Feng, J., Chmelka, B. F. & Stucky, G. D. Nonionic Triblock and Star Diblock Copolymer and Oligomeric Surfactant Syntheses of Highly Ordered, Hydrothermally Stable, Mesoporous Silica Structures. *J. Am. Chem. Soc.* **120**, 6024–6037 (1998).
16. Li, B. *et al.* SBA-15 Supported Cesium Catalyst for Methyl Methacrylate Synthesis via Condensation of Methyl Propionate with Formaldehyde. *Ind. Eng. Chem. Res.* **53**, 1386–1395 (2014).
17. Wang, Y. *et al.* Lanthanum and Cesium-Loaded SBA-15 Catalysts for MMA Synthesis by Aldol Condensation of Methyl Propionate and Formaldehyde. *Catal. Letters* **146**, 1808–1819 (2016).

18. He, T., Qu, Y. & Wang, J. Experimental and Theoretical Study for Vapor Phase Aldol Condensation of Methyl Acetate and Formaldehyde over Alkali Metal Oxides Supported on SBA-15. *Ind. Eng. Chem. Res.* **57**, 2773–2787 (2018).

19. Brunelli, N. A., Venkatasubbaiah, K. & Jones, C. W. Cooperative Catalysis with Acid–Base Bifunctional Mesoporous Silica: Impact of Grafting and Co-condensation Synthesis Methods on Material Structure and Catalytic Properties. *Chem. Mater.* **24**, 2433–2443 (2012).

20. Gogate, M. R., Spivey, J. J. & Zoeller, J. R. Synthesis of methyl methacrylate by vapor phase condensation of formaldehyde with propionate derivatives. *Catal. Today* **36**, 243–255 (1997).

21. Li, B. *et al.* Synthesis of Methyl Methacrylate by Aldol Condensation of Methyl Propionate with Formaldehyde Over Acid–Base Bifunctional Catalysts. *Catal. Letters* **143**, 829–839 (2013).

22. Roelofs, J. C. A. A., Lensveld, D. J., van Dillen, A. J. & de Jong, K. P. On the Structure of Activated Hydrotalcites as Solid Base Catalysts for Liquid-Phase Aldol Condensation. *J. Catal.* **203**, 184–192 (2001).

23. Zeidan, R. K. & Davis, M. E. The effect of acid–base pairing on catalysis: An efficient acid–base functionalized catalyst for aldol condensation. *J. Catal.* **247**, 379–383 (2007).

24. Collier, V. E., Ellebracht, N. C., Lindy, G. I., Moschetta, E. G. & Jones, C. W. Kinetic and Mechanistic Examination of Acid-Base Bifunctional Aminosilica Catalysts in Aldol and Nitroaldol Condensations. *ACS Catal.* **6**, 460–468 (2016).

25. Brunelli, N. A., Didas, S. A., Venkatasubbaiah, K. & Jones, C. W. Tuning cooperativity by controlling the linker length of silica-supported amines in catalysis and CO 2 capture.

J. Am. Chem. Soc. **134**, 13950–13953 (2012).

26. Climent, M. J., Corma, A., Iborra, S., Epping, K. & Velty, A. Increasing the basicity and catalytic activity of hydrotalcites by different synthesis procedures. *J. Catal.* **225**, 316–327 (2004).

27. Morgenthaler, S., Zink, C. & Spencer, N. D. Surface-chemical and -morphological gradients. *Soft Matter* **4**, 419–434 (2008).

28. Bhat R.R. and Genzer J. Surface-Bound Soft Matter Gradients. *Langmuir* **24**, 2294–2317 (2008).

29. Genzer, J. Surface-Bound Gradients for Studies of Soft Materials Behavior. *http://dx.doi.org/10.1146/annurev-matsci-070511-155050* **42**, 435–468 (2012).

30. Almodóvar, J. *et al.* Gradients of physical and biochemical cues on polyelectrolyte multilayer films generated via microfluidics. *Lab Chip* **13**, 1562 (2013).

31. Davis, R. L., Jayaraman, S., Chaikin, P. M. & Register, R. A. Creating Controlled Thickness Gradients in Polymer Thin Films via Flowcoating. *Langmuir* **30**, 5637–5644 (2014).

32. Alshehri, A. H. *et al.* Nanoscale Film Thickness Gradients Printed in Open Air by Spatially Varying Chemical Vapor Deposition. *Adv. Funct. Mater.* **31**, 2103271 (2021).

33. Tobias Kraus *et al.* Printing Chemical Gradients. *Langmuir* **21**, 7796–7804 (2005).

34. Khire, V. S., Benoit, D. S. W., Anseth, K. S. & Bowman, C. N. Ultrathin gradient films using thiol-ene polymerizations. *J. Polym. Sci. Part A Polym. Chem.* **44**, 7027–7039 (2006).

35. K. Mougin, A. S. Ham, M. B. Lawrence, E. J. Fernandez, and & A. C. Hillier, ‖. Construction of a Tethered Poly(ethylene glycol) Surface Gradient For Studies of Cell

Adhesion Kinetics. *Langmuir* **21**, 4809–4812 (2005).

36. Rupper, P., Vandenbossche, M., Bernard, L., Hegemann, D. & Heuberger, M. Composition and Stability of Plasma Polymer Films Exhibiting Vertical Chemical Gradients. *Langmuir* **33**, 2340–2352 (2017).

37. Ashraf, K. M., Roy, K., Higgins, D. A. & Collinson, M. M. On the Importance of Silane Infusion Order on theMicroscopic and Macroscopic Properties of Multifunctional Charge Gradients. *ACS Omega* **5**, 21897 (2020).

38. Gell, C. *et al. Handbook of Single Molecule Fluorescence Spectroscopy*. Oxford University Press, New York (2006).

39. Moerner, W. E. & Kador, L. Optical detection and spectroscopy of single molecules in a solid. *Phys. Rev. Lett.* **62**, 2535–2539 (1989).

40. Michalet, X. & Weiss, S. Single-molecule spectroscopy and microscopy. *Comptes rendus - Phys.* **3**, 619–645 (2002).

41. Moerner, W. E. Single-Molecule Spectroscopy, Imaging, and Photocontrol: Foundations for Super-Resolution Microscopy (Nobel Lecture). *Angew. Chemie Int. Ed.* **54**, 8067–8094 (2015).

42. Moerner, W. E., Shechtman, Y. & Wang, Q. Single-molecule spectroscopy and imaging over the decades. *Faraday Discuss.* **184**, 9–37 (2015).

43. Moerner, W. E. A Dozen Years of Single-Molecule Spectroscopy in Physics, Chemistry, and Biophysics. *J. Phys. Chem. B* **106**, 910–928 (2002).

44. Weiss, S. Fluorescence Spectroscopy of Single Biomolecules. *Science (80).* **283**, 1676 (1999).

45. Keeling-Tucker, T. & Brennan, J. D. Fluorescent Probes as Reporters on the Local

Structure and Dynamics in Sol−Gel-Derived Nanocomposite Materials. *Chem. Mater.* **13**, 3331–3351 (2001).

46. Owen, C. S. Comparison of spectrum-shifting intracellular pH probes 5′(and 6′)-carboxy-10-dimethylamino-3-hydroxyspiro[7H-benzo[c]xanthene-7, 1′(3′H)-isobenzofuran]-3′-one and 2′,7′-biscarboxyethyl-5(and 6)-carboxyfluorescein. *Anal. Biochem.* **204**, 65–72 (1992).

47. Higgins, D. A., Park, S. C., Tran-Ba, K.-H. & Ito, T. Single-Molecule Investigations of Morphology and Mass Transport Dynamics in Nanostructured Materials. *Annu. Rev. Anal. Chem.* **8**, 193–217 (2015).

48. Ye, F. *et al.* Fluorescence Spectroscopy Studies of Silica Film Polarity Gradients Prepared by Infusion-Withdrawal Dip-Coating. *Chem. Mater.* **22**, 2970–2978 (2010).

49. Higgins, D. A., Collinson, M. M., Saroja, G. & Bardo, A. M. Single-Molecule Spectroscopic Studies of Nanoscale Heterogeneity in Organically Modified Silicate Thin Films. *Chem. Mater.* **14**, 3734–3745 (2002).

50. Sun, X., Xie, J., Xu, J., Higgins, D. A. & Hohn, K. L. Single-molecule studies of acidity distributions in mesoporous aluminosilicate thin films. *Langmuir* **31**, 5667–5676 (2015).

51. Roeffaers, M.B.J. *et al.* Super-Resolution Reactivity Mapping of Nanostructured Catalyst Particles. *Angew. Chemie Int. Ed.* **48**, 9285–9289 (2009).

52. Chen, P., Kong, J. S., Xu, W. & Yeh, Y.-T. E. Single-molecule nanocatalysis reveals heterogeneous reaction pathways and catalytic dynamics. *Nat. Mater.* **7**, 992–997 (2008).

53. Zhang, Y., Song, P., Fu, Q., Ruan, M. & Xu, W. Single-molecule chemical reaction reveals molecular reaction kinetics and dynamics. *Nat. Commun.* **5**, 1–8 (2014).

54. Roeffaers, M. B. J. *et al.* Single-Molecule Fluorescence Spectroscopy in (Bio)Catalysis.

Proc. Natl. Acad. Sci. U. S. A. **104**, 12603–12610 (2007).

55. Xu, W., Kong, J. S. & Chen, P. Single-Molecule Kinetic Theory of Heterogeneous and Enzyme Catalysis. *J. Phys. Chem. C* **113**, 2393–2405 (2009).

56. Roeffaers, M. B. J. *et al.* Fluorescence microscopy: Bridging the phase gap in catalysis. *Catal. Today* **126**, 44–54 (2007).

57. Karwacki, L., Stavitski, E., Kox, M. H. F., Kornatowski, J. & Weckhuysen, B. M. On the intergrowth structure of zeolite crystals as revealed by wide field and confocal fluorescence microscopy of the template removal processes. in *Studies in Surface Science and Catalysis* vol. 174 757–763 (2008).

58. Brasselet, S. & Moerner, W. E. Fluorescence Behavior of Single-Molecule pH-Sensors. *Single Mol.* **1**, 17–24.

59. Ristanović, Z., Kubarev, A. V., Hofkens, J., Roeffaers, M. B. J. & Weckhuysen, B. M. Single Molecule Nanospectroscopy Visualizes Proton-Transfer Processes within a Zeolite Crystal. *J. Am. Chem. Soc.* **138**, 13586–13596 (2016).

60. Uji-i, H. *et al.* Spatially resolved observation of crystal-face-dependent catalysis by single turnover counting. *Nature* **439**, 572–576 (2006).

61. Liu, X., Chen, T., Jain, P. K. & Xu, W. Revealing the Thermodynamic Properties of Elementary Chemical Reactions at the Single-Molecule Level. *J. Phys. Chem. B* **123**, 6253–6259 (2019).

62. Ristanović, Z. *et al.* Quantitative 3D Fluorescence Imaging of Single Catalytic Turnovers Reveals Spatiotemporal Gradients in Reactivity of Zeolite H-ZSM-5 Crystals upon Steaming. *J. Am. Chem. Soc.* **137**, 6559–6568 (2015).

63. Buurmans, I. L. C. *et al.* Catalytic activity in individual cracking catalyst particles imaged

throughout different life stages by selective staining. *Nat. Chem.* **3**, 862–868 (2011).

64. Buurmans, I. L. C. *et al.* Staining of fluid-catalytic cracking catalysts: Localising Brønsted acidity within a single catalyst particle. *Chem. Eur. J.* **18**, 1094–1102 (2012).

65. Decan, M. R., Impellizzeri, S., Marin, M. L. & Scaiano, J. C. Copper nanoparticle heterogeneous catalytic 'click' cycloaddition confirmed by single-molecule spectroscopy. *Nat. Commun.* **5**, 4612 (2014).

66. Tachikawa, T., Yamashita, S. & Majima, T. Evidence for Crystal-Face-Dependent TiO2 Photocatalysis from Single-Molecule Imaging and Kinetic Analysis. *J. Am. Chem. Soc.* **133**, 7197–7205 (2011).

67. Roeffaers, M. B. J. *et al.* Space- and time-resolved visualization of acid catalysis in ZSM-5 crystals by fluorescence microscopy. *Angew. Chem. Int. Ed. Engl.* **46**, 1706–1710 (2007).

68. Nisticò, R., Scalarone, D. & Magnacca, G. Sol-gel chemistry, templating and spin-coating deposition: A combined approach to control in a simple way the porosity of inorganic thin films/coatings. *Microporous and Mesoporous Materials* vol. 248 18–29 (Elsevier, 2017).

69. Brinker, C. J. & Scherer, G. W. Sol-Gel Science: The Physics and Chemistry of Sol-Gel Processing. Academic Press (2013) .

70. The Sol-Gel Handbook. Levy, D. and Zayat, M., Ed. Wiley-VCH (2015).

71. Nishio, K. & Tsuchiya, T. Sol-Gel Processing of Thin Films with Metal Salts in: Handbook of Sol-Gel Science and Technology. Springer (2004).

72. Schubert, U. Chemistry and Fundamentals of the Sol-Gel Process in:The Sol-Gel Handbook. Wiley-VCH (2015).

73. Hench, L. L. & West, J. K. The sol-gel process. *Chem. Rev.* **90**, 33–72 (2002).

74. Grosso, D., Boissière, C. & Faustini, M. Thin Film Deposition Techniques in: The Sol-Gel Handbook. Wiley-VCH (2015)

75. Wang, Z. L., Liu, Y. & Zhang, Z. Handbook of nanophase and nanostructured materials. Kluwer Academic Publishers (2003).

76. Babonneau, F. & Bonhomme, C. Solid-State NMR Characterization of Sol-Gel Materials: Recent Advances, in: The Sol-Gel Handbook. Wiley-VCH (2015)

77. Almeida, R. M. & Xu, J. Characterization of Sol-Gel Materials by Optical Spectroscopy Methods, in: The Sol-Gel Handbook. Wiley-VCH (2015)

78. Baer, D. R. & Thevuthasan, S. Characterization of Thin Films and Coatings. in *Handbook of Deposition Technologies for Films and Coatings* 749–864 Elsevier Inc., (2010).

79. X-Ray Photoelectron Spectroscopy | X-Ray Photoelectron Spectroscopy Imaging | Thermo Fisher Scientific - US. https://www.thermofisher.com/us/en/home/materials-science/learning-center/surface-analysis/xps-imaging.html.

80. Haack, L. P., DeBolt, M. A., Kaberline, S. L., Devries, J. E. & Dickie, R. A. XPS mapping technique for the identification of adhesion loss mechanisms. *Surf. Interface Anal.* **20**, 115–120 (1993).

81. Bautista-Gomez, J., Forzano, A. V., Austin, J. M., Collinson, M. M. & Higgins, D. A. Vapor-Phase Plotting of Organosilane Chemical Gradients. *Langmuir* **34**, 9665–9672 (2018).

82. Collinson, M. M. & Higgins, D. A. Organosilane Chemical Gradients: Progress, Properties, and Promise. *Langmuir* **33**, 13719–13732 (2017).

83. Smith, B. C. Fundamentals of Fourier Transform Infrared Spectroscopy. CRC Press, (2011).

84. Thermo Nicolet Corporation. *Introduction to Fourier Transform Infrared Spectrometry*. (2001).

85. Khan, S. A. *et al.* Fourier transform infrared spectroscopy: Fundamentals and application in functional groups and nanomaterials characterization. in *Handbook of Materials Characterization* 317–344 Springer International Publishing, (2018).

86. Sutandar, P., Ahn, D. J. & Franses, E. I. FTIR ATR Analysis for Microstructure and Water Uptake in Poly(methyl methacrylate) Spin Cast and Langmuir-Blodgett Thin Films. *Macromolecules* **27**, 7316–7328 (1994).

87. Cui, C., Kirkeminde, A., Kannan, B., Collinson, M. M. & Higgins, D. A. Spatiotemporal Evolution of Fixed and Mobile Dopant Populations in Silica Thin-Film Gradients as Revealed by Single Molecule Tracking. *J. Phys. Chem. C* **115**, 728–736 (2011).

88. Laroche, G., Fitremann, J. & Gherardi, N. FTIR-ATR spectroscopy in thin film studies: The importance of sampling depth and deposition substrate. *Appl. Surf. Sci.* **273**, 632–637 (2013).

89. Tompkins, H. G. & Irene, E. A. *Handbook of Ellipsometry* Elsevier Inc., (2005).

90. Woollam, J. A. & Spectroscopic Ellipsometers, C. *CompleteEASE ® Data Acquisition and Analysis Software for Software Manual*. www.jawoollam.com.

91. Langereis, E. *et al.* In situ spectroscopic ellipsometry as a versatile tool for studying atomic layer deposition. *J. Phys. D. Appl. Phys.* **42**, 73001 (2009).

92. Huhtamäki, T., Tian, X., Korhonen, J. T. & Ras, R. H. A. Surface-wetting characterization using contact-angle measurements. *Nat. Protoc.* **13**, 1521–1538 (2018).

93. Miyama, M., Yang, Y., Yasuda, T., Okuno, T. & Yasuda, H. K. Static and dynamic contact angles of water on polymeric surfaces. *Langmuir* **13**, 5494–5503 (1997).

94. Contact Angle | Measurements | Biolin Scientific. https://www.biolinscientific.com/measurements/contact-angle.

95. Nagy, N. Contact Angle Determination on Hydrophilic and Superhydrophilic Surfaces by Using r-?-Type Capillary Bridges. *Langmuir* **35**, 5202–5212 (2019).

96. Static contact angle | KRÜSS Scientific. https://www.kruss-scientific.com/en-US/know-how/glossary/static-contact-angle.

97. Tillman, N., Ulman, A., Schildkraut, J. S. & Penner, T. L. Incorporation of Phenoxy Groups in Self-Assembled Monolayers of Trichlorosilane Derivatives: Effects on Film Thickness, Wettability, and Molecular Orientation. *J. Am. Chem. Soc.* **110**, 6136–6144 (1988).

98. Yadav, A. R., Sriram, R., Carter, J. A. & Miller, B. L. Comparative study of solution-phase and vapor-phase deposition of aminosilanes on silicon dioxide surfaces. *Mater. Sci. Eng. C* **35**, 283–290 (2014).

99. Zhang, F. *et al.* Chemical vapor deposition of three aminosilanes on silicon dioxide: Surface characterization, stability, effects of silane concentration, and cyanine dye adsorption. *Langmuir* **26**, 14648–14654 (2010).

100. Dhere, S. L. *et al.* Transparent water repellent silica films by sol-gel process. *Appl. Surf. Sci.* **256**, 3624–3629 (2010).

101. Yu, X., Wang, Z., Jiang, Y. & Zhang, X. Surface gradient material: From superhydrophobicity to superhydrophilicity. *Langmuir* **22**, 4483–4486 (2006).

102. Morgenthaler, S., Lee, S., Zürcher, S. & Spencer, N. D. A Simple, Reproducible Approach to the Preparation of Surface-Chemical Gradients. *Langmuir* **19**, 10459–10463 (2003).

103. Lakowicz, J. R. Principles of fluorescence spectroscopy. (Springer, 2006).

104. Sauer, M., Hofkens, J. & Enderlein, J. Handbook of Fluorescence Spectroscopy and Imaging: From Single Molecules to Ensembles. Wiley-VCH (2011).

105. Basché, T., Moerner, W. E., Orrit, M. & Wild, U. P. Single-Molecule Optical Detection, Imaging and Spectroscopy. VCH (1997)

106. Eli, B., YounJoon, J. & Robert, S. Theory of single-molecule spectroscopy: beyond the ensemble average. *Annu. Rev. Phys. Chem.* **55**, 457–507 (2004).

107. Moerner, W. E. & Fromm, D. P. Methods of single-molecule fluorescence spectroscopy and microscopy. *Review of Scientific Instruments* vol. 74 3597–3620 (2003).

108. Yan, J. *et al.* Vapor phase condensation of methyl acetate with formaldehyde to preparing methyl acrylate over cesium supported SBA-15 catalyst. *J. Ind. Eng. Chem.* **25**, 344–351 (2015).

109. Ai, M. Formation of methyl methacrylate by condensation of methyl propionate with formaldehyde over silica-supported cesium hydroxide catalysts. *Appl. Catal. A Gen.* **288**, 211–215 (2005).

110. Tai, J. & Davis, R. J. Synthesis of methacrylic acid by aldol condensation of propionic acid with formaldehyde over acid–base bifunctional catalysts. *Catal. Today* **123**, 42–49 (2007).

111. Bailey, O. H., Montag, R. A. & Yoo, J. S. Methacrylic acid synthesis: I. Condensation of propionic acid with formaldehyde over alkali metal cation on silica catalysts. *Appl. Catal. A Gen.* **88**, 163–177 (1992).

112. Wang, Y. *et al.* Preparation of Cs-La-Sb/SiO2 catalyst and its performance for the synthesis of methyl acrylate by aldol condensation. *RSC Adv.* **5**, 32826–32834 (2015).

113. Ai, M. Formation of Acrylaldehyde by Vapor-Phase Aldol Condensation II. Phosphate Catalysts. *Bull. Chem. Soc. Jpn.* **64**, 1346–1350 (1991).

114. Ai, M. Formation of Acrylaldehyde by Vapor-Phase Aldol Condensation I. Basic Oxide Catalysts. *Bull. Chem. Soc. Jpn.* **64**, 1342–1345 (1991).

115. Dumitriu, E. *et al.* Influence of the acid–base properties of solid catalysts derived from hydrotalcite-like compounds on the condensation of formaldehyde and acetaldehyde. *Appl. Catal. A Gen.* **178**, 145–157 (1999).

116. Fu, Y., Collinson, M. M. & Higgins, D. A. Single-Molecule Spectroscopy Studies of Microenvironmental Acidity in Silicate Thin Films. *J. Am. Chem. Soc.* **3**, 13838–13845 (2004).

117. van Erp, P. E. *et al.* Ratiometric measurement of intracellular pH in cultured human keratinocytes using carboxy-SNARF-1 and flow cytometry. *Cytometry* **12**, 127–133 (1991).

118. Whitaker, J. E., Haugland, R. P. & Prendergast, F. G. Spectral and photophysical studies of benzo[c]xanthene dyes: Dual emission pH sensors. *Anal. Biochem.* **194**, 330–345 (1991).

119. Giri, D., Hanks, C. N., Collinson, M. M. & Higgins, D. A. Single-Molecule Spectroscopic Imaging Studies of Polarity Gradients Prepared by Infusion-Withdrawal Dip-Coating. *J. Phys. Chem. C* **118**, 6423–6433 (2014).

120. Lee, M.-H., Min, B. K., Son, J. S. & Kwon, T.-Y. Influence of Different Post-Plasma Treatment Storage Conditions on the Shear Bond Strength of Veneering Porcelain to Zirconia. *Materials (Basel).* **9**, (2016).

121. Owen, C. S., Carango, P., Grammer, S., Bobyock, S. & Leeper, D. B. pH-dependent

intracellular quenching of the indicator carboxy-SNARF-1. *J. Fluoresc.* **2**, 75–81 (1992).

122. Yassine, M., Salmon, J. M., Vigo, J. & Viallet, P. C-SNARF-1 as a pHi fluoroprobe: Discrepancies between conventional and intracellular data do not result from protein interactions. *J. Photochem. Photobiol. B Biol.* **37**, 18–25 (1997).

123. Cheng, J., Soetjipto, C., Hoffmann, M. R. & Colussi, A. J. Confocal Fluorescence Microscopy of the Morphology and Composition of Interstitial Fluids in Freezing Electrolyte Solutions. *J. Phys. Chem. Lett.* **1**, 374–378 (2009).

124. Blank, P. S. *et al.* Cytosolic pH measurements in single cardiac myocytes using carboxy-seminaphthorhodafluor-1. *Am. J. Physiol. - Hear. Circ. Physiol.* **263**, (1992).

125. Ribou, A. C., Vigo, J. & Salmon, J. M. C-SNARF-1 as a fluorescent probe for pH measurements in living cells: Two-wavelength-ratio method versus whole-spectral-resolution method. *J. Chem. Educ.* **79**, 1471–1474 (2002).

126. Zeidan, R. K., Hwang, S. J. & Davis, M. E. Multifunctional heterogeneous catalysts: SBA-15-containing primary amines and sulfonic acids. *Angew. Chemie - Int. Ed.* **45**, 6332–6335 (2006).

127. John D. Bass, Andrew Solovyov, Andrew J. Pascall, and & Katz, A. Acid−Base Bifunctional and Dielectric Outer-Sphere Effects in Heterogeneous Catalysis: A Comparative Investigation of Model Primary Amine Catalysts. *J. Am. Chem. Soc.* **128**, 3737–3747 (2006).

128. Chaudhury, M. K. & Whitesides, G. M. How to Make Water Run Uphill. *Science (80-.).* **256**, 1539–1541 (1992).

129. Jan Genzer, Kirill Efimenko, and & Fischer, D. A. Formation Mechanisms and Properties of Semifluorinated Molecular Gradients on Silica Surfaces. *Langmuir* **22**,

8532–8541 (2006).

130. Ashraf, K. M., Giri, D., Wynne, K. J., Higgins, D. A. & Collinson, M. M. Cooperative Effects in Aligned and Opposed Multicomponent Charge Gradients Containing Strongly Acidic, Weakly Acidic, and Basic Functional Groups. *Langmuir* **32**, 3836–3847 (2016).

131. E. W. van der Vegte and Hadziioannou, G. Acid−Base Properties and the Chemical Imaging of Surface-Bound Functional Groups Studied with Scanning Force Microscopy. *J. Phys. Chem. B* **101**, 9563–9569 (1997).

132. Xie, J. *et al.* Exploring Microenvironment Acidity Inside the Solvent-Filled Pores of Mesoporous Silica Thin Films via Single-Molecule Spectroscopy. *J. Phys. Chem. C* **123**, 20333–20341 (2019).

133. Deye, J. F., Berger, T. A. & Anderson, A. G. Nile Red as a Solvatochromic Dye for Measuring Solvent Strength in Normal Liquids and Mixtures of Normal Liquids with Supercritical and Near Critical Fluids. *Anal. Chem.* **62**, 615–622 (1990).

134. Lobnik, A. & Wolfbeis, O. S. Probing the Polarity of Sol-Gels and Ormosils via the Absorption of Nile Red. *J. Sol-Gel Sci. Technol.* **20**, 303–311 (2001).

135. Chelsea, M. H., Erin A. R., Jorge, P.C. & Phillip, J. R. Measuring the spatial distribution of dielectric constants in polymers through quasi-single molecule microscopy. *J. Phys. Chem. B* **117**, 7106–7112 (2013).

136. Dickson, R. M. *et al.* Single molecules solvated in pores of polyacrylamide gels. *Mol. Cryst. Liq. Cryst.* **291**, 31–39 (1996).

137. Yanwen Hou, Angela M. Bardo, Cruz Martinez, and Higgins, D. A. Characterization of Molecular Scale Environments in Polymer Films by Single Molecule Spectroscopy. *J. Phys. Chem. B* **104**, 212–219 (1999).

138. Bardo, A. M., Collinson, M. M. & Higgins, D. A. Nanoscale properties and matrix-dopant interactions in dye-doped organically modified silicate thin films. *Chem. Mater.* **13**, 2713–2721 (2001).

139. Kumarasinghe, R., Ito, T. & Higgins, D. A. Nanoconfinement and Mass Transport in Silica Mesopores: the Role of Charge at the Single Molecule and Single Pore Levels. *Anal. Chem.* **92**, 1416–1423 (2019).

140. Xu, H. *et al.* Spectroscopic imaging studies of nanoscale polarity and mass transport phenomena in self-assembled organic nanotubes. *Phys. Chem. Chem. Phys.* **19**, 20040–20048 (2017).

141. Sebők-Nagy, K., Miskolczy, Z. & Biczók, L. Interaction of 2-Hydroxy-substituted Nile Red Fluorescent Probe with Organic Nitrogen Compounds. *Photochem. Photobiol.* **81**, 1212 (2005).

142. Selivanov, N. I., Samsonova, L. G., Artyukhov, V. Y. & Kopylova, T. N. Theoretical and experimental investigations of photophysics of the nile red molecule and its protonated structures. *Russ. Phys. J. 2011 545* **54**, 601–606 (2011).

143. Chen, T. *et al.* Optical Super-Resolution Imaging of Surface Reactions. *Chem. Rev.* **117**, 7510–7537 (2017).

144. Li, Z., Ashraf, K. M., Collinson, M. M. & Higgins, D. A. Single Molecule Catch and Release: Potential-Dependent Plasmid DNA Adsorption along Chemically Graded Electrode Surfaces. *Langmuir* **33**, 8651–8662 (2017).

145. Stalder, A. F. *et al.* Low-bond axisymmetric drop shape analysis for surface tension and contact angle measurements of sessile drops. *Colloids Surfaces A Physicochem. Eng. Asp.* **364**, 72–81 (2010).

146. Ba, K. H. T., Everett, T. A., Ito, T. & Higgins, D. A. Trajectory angle determination in one dimensional single molecule tracking data by orthogonal regression analysis. *Phys. Chem. Chem. Phys.* **13**, 1827–1835 (2011).

147. Kumarasinghe, R., Higgins, E. D., Ito, T. & Higgins, D. A. Spectroscopic and Polarization-Dependent Single-Molecule Tracking Reveal the One-Dimensional Diffusion Pathways in Surfactant-Templated Mesoporous Silica. *J. Phys. Chem. C* **120**, 715–723 (2015).

148. Zhu, M., Lerum, M. Z. & Chen, W. How To Prepare Reproducible, Homogeneous, and Hydrolytically Stable Aminosilane-Derived Layers on Silica. *Langmuir* **28**, 416–423 (2011).

149. Zeng, X., Xu, G., Gao, Y. & An, Y. Surface Wettability of (3-Aminopropyl)triethoxysilane Self-Assembled Monolayers. *J. Phys. Chem. B* **115**, 450–454 (2010).

150. Moses, P. R. *et al.* X-ray Photoelectron Spectroscopy of Alkylamine-Silanes Bound to Metal Oxide Electrodes. *Anal. Chem.* **50**, 576–585 (1978).

151. Sherwood, P. M. A. The use and misuse of curve fitting in the analysis of core X-ray photoelectron spectroscopic data. *Surf. Interface Anal.* **51**, 589–610 (2019).

152. Stuart, M. C. A., Pas, J. C. van de & Engberts, J. B. F. N. The use of Nile Red to monitor the aggregation behavior in ternary surfactant–water–organic solvent systems. *J. Phys. Org. Chem.* **18**, 929–934 (2005).

153. Carmichael, A. J. & Seddon, K. R. Polarity study of some 1-alkyl-3-methylimidazolium ambient-temperature ionic liquids with the solvatochromic dye, Nile Red. *J. Phys. Org. Chem.* **13**, 591–595 (2000).

154. Datta, A., Mandal, D., Pal, S. K. & Bhattacharyya, K. Intramolecular charge transfer processes in confined systems. Nile red in reverse micelles. *J. Phys. Chem. B* **101**, 10221–10225 (1997).

155. Sackett, D. L. & Wolff, J. Nile red as a polarity-sensitive fluorescent probe of hydrophobic protein surfaces. *Anal. Biochem.* **167**, 228–234 (1987).

156. Li, Z., Kumarasinghe, R., Collinson, M. M. & Higgins, D. A. Probing the Local Dielectric Constant of Plasmid DNA in Solution and Adsorbed on Chemically Graded Aminosilane Surfaces. *J. Phys. Chem. B* **122**, 2307–2313 (2018).

157. *Handbook of Chemistry and Physics*: 82nd ed. Lide, D.R, Ed. CRC Press, Boca Raton (2001).

158. Riddick, J. A. Acid-Base Titrations in Nonaqueous Solvents. *Anal. Chem.* **30**, 793–805 (2002).

159. Kolling, O. W. Red Shift for Solvatochromic Indicators as a Measure of Solvent Basicity in Polar Aprotic Media. *Anal. Chem.* **48**, 884–886 (1976).

160. Hall, H.K. Jr. Correlation of the Base Strengths of Amines1. *J. Am. Chem. Soc.* **79**, 5441–5444 (2002).

161. Ong, S., Zhao, X. & Eisenthal, K. B. Polarization of water molecules at a charged interface: second harmonic studies of the silica/water interface. *Chem. Phys. Lett.* **191**, 327–335 (1992).

162. Kox, M.H.F., Stavitsky, E. and Weckhuysen, B.M. Nonuniform catalytic behavior of zeolite crystals as revealed by in situ optical microspectroscopy. *Angew. Chem. Int. Ed. Engl.* **46**, 3652–3655 (2007).

163. Zürner, A., Kirstein, J., Döblinger, M., Bräuchle, C. & Bein, T. Visualizing single-

molecule diffusion in mesoporous materials. *Nat. 2007 4507170* **450**, 705–708 (2007).

164. Cremer, G. De, Sels, B. F., Vos, D. E. De, Hofkens, J. & Roeffaers, M. B. J. NASCA Microscopy: Super-Resolution Mapping of Chemical Reaction Centers. in 245–261 (2011). doi:10.1007/4243_2011_33.

165. Descloux, A. C. *et al.* Experimental Combination of Super-Resolution Optical Fluctuation Imaging with Structured Illumination Microscopy for Large Fields-of-View. *ACS Photonics* **8**, 2440–2449 (2021).

166. Dedecker, P., Duwe, S., Neely, R.K. & Zhang, J. Localizer: fast, accurate, open-source, and modular software package for superresolution microscopy. *J. Biomed. Opt.* **17**, 126008 (2012).

167. Klevanski, M. *et al.* Automated highly multiplexed super-resolution imaging of protein nano-architecture in cells and tissues. *Nat. Commun. 2020 111* **11**, 1–11 (2020).

168. Z, R. *et al.* High-resolution single-molecule fluorescence imaging of zeolite aggregates within real-life fluid catalytic cracking particles. *Angew. Chem. Int. Ed. Engl.* **54**, 1836–1840 (2015).

169. Tachikawa, T. & Majima, T. Single-molecule, single-particle approaches for exploring the structure and kinetics of nanocatalysts. *Langmuir* **28**, 8933–8944 (2012).

170. Zhou, X., Xu, W., Liu, G., Panda, D. & Chen, P. Size-dependent catalytic activity and dynamics of gold nanoparticles at the single-molecule level. *J. Am. Chem. Soc.* **132**, 138–147 (2010).

171. Canham, S. M. *et al.* Toward the Single-Molecule Investigation of Organometallic Reaction Mechanisms: Single-Molecule Imaging of Fluorophore-Tagged Palladium(II) Complexes. *Organometallics* **27**, 2172–2175 (2008).

172. Esfandiari, N. M. *et al.* Single-Molecule Imaging of Platinum Ligand Exchange Reaction Reveals Reactivity Distribution. *J. Am. Chem. Soc.* **132**, 15167–15169 (2010).

173. Esfandiari, N. M., Wang, Y., McIntire, T. M. & Blum, S. A. Real-Time Imaging of Platinum−Sulfur Ligand Exchange Reactions at the Single-Molecule Level via a General Chemical Technique. *Organometallics* **30**, 2901–2907 (2011).

174. Bautista-Gomez, J. *et al.* Fluorescence spectroscopy studies of crossed aldol reactions: A reactive Nile red dye reveals catalyst-dependent product formation. *Catal. Sci. Technol.* **10**, 5579–5592 (2020).

175. Rybina, A. *et al.* Distinguishing Alternative Reaction Pathways by Single-Molecule Fluorescence Spectroscopy. *Angew. Chemie Int. Ed.* **52**, 6322–6325 (2013).

176. Arkles, B. & Larson, G. L. Silicon compounds : silanes and silicones. (2013).

177. The Carbonyl Group, Part I: Introduction. https://www.spectroscopyonline.com/view/carbonyl-group-part-i-introduction.

178. Canham, S. M. *et al.* Toward the Single-Molecule Investigation of Organometallic Reaction Mechanisms: Single-Molecule Imaging of Fluorophore-Tagged Palladium(II) Complexes. *Organometallics* **27**, 2172–2176 (2008).

179. Margelefsky, E. L., Zeidan, R. K., Dufaud, V. & Davis, M. E. Organized surface functional groups: Cooperative catalysis via thiol/sulfonic acid pairing. *J. Am. Chem. Soc.* **129**, 13691–13697 (2007).

180. Dufaud, V. & Davis, M. E. Design of Heterogeneous Catalysts via Multiple Active Site Positioning in Organic−Inorganic Hybrid Materials. *J. Am. Chem. Soc.* **125**, 9403–9414 (2003).

Appendix A - Supplementary Information

A description of how the *E* values for Nile Red in ethyl acetate and acetic acid solution were predicted is provided. Also included are XPS data from uniform (nongradient) aminosilane and silica films, along with single molecule spectroscopic data acquired from Nile Red dispersed on a uniform silica film. The full set of ΔE results (see Figure 4.7) obtained along the entire length of the aminosilane gradient samples are also provided.

A.1 Estimation of E values for Nile Red in ethyl acetate and acetic acid.

The *E* values expected for Nile Red in different solvent media are approximately related to the dielectric constant, ε, of the solvent, as defined in Equation A.1:[119]

$$E = K\left(\frac{\varepsilon - 1}{2\varepsilon + 1}\right) + C \quad \text{(A.1)}$$

In this empirical relationship, *K* and *C* are constants that must be determined by experimental measurement of *E* using a series of solvent mixtures having different dielectric constants. Due to the approximate and phenomenological nature of this equation, the ε values employed in determining *K* and *C* have been estimated under the assumption of a simple linear relationship between the composition of a solvent mixture and its dielectric constant. Here, the data presented in a previous manuscript were used as a means to estimate *K* and *C* at 3.48 ± 0.13 and -0.92 ± 0.04, respectively, from a series of ethanol/hexane mixtures. Using ε values for ethyl acetate and acetic acid of 6.08 and 6.20,[157] in Equation A.1, a difference in *E* of < 0.01 units is predicted for these two solvents. Note that the values of *E* predicted for ethyl acetate and acetic acid using the K and C values given above are far from the values observed in Figure 4.3 due to the different intermolecular interactions that occur in different solvents in general, and the participation of hydrogen bonding in the presence of acetic acid, in particular.

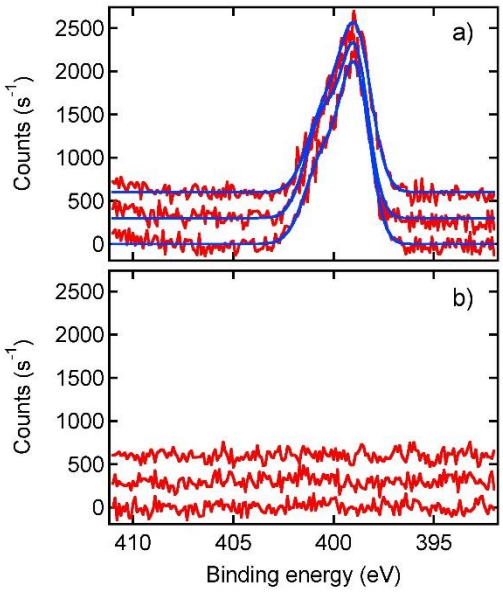

Figure A.1. a) XPS spectra (red lines) of N1s peaks recorded on a uniform aminosilane film at ~ 8.5 mm spacings, beginning ~ 1.5 mm from the film edge. Each spectrum was fit to a pair of Gaussian functions (blue lines) centered at binding energies of 398.9 eV and 400.5 eV, which are assigned to the unprotonated and protonated forms of the aminosilane nitrogen, respectively. b) N1s spectra obtained from a silica baselayer in the absence of an aminosilane film at ~ 8.5 mm spacings, beginning ~ 1.5 mm from the film edge. The background-subtracted spectra in each series have been offset from zero to allow for better visualization.

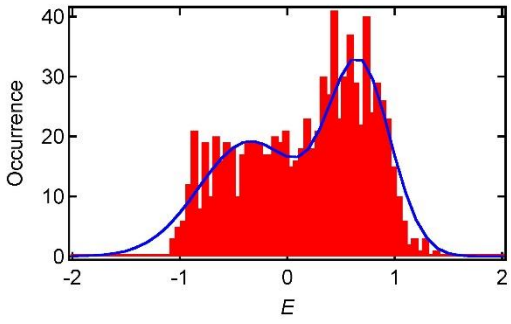

Figure A.2. Histogram depicting the single molecule emission ratio (red bars) on a uniform silica film and its fit to a two component Gaussian distribution (blue line).

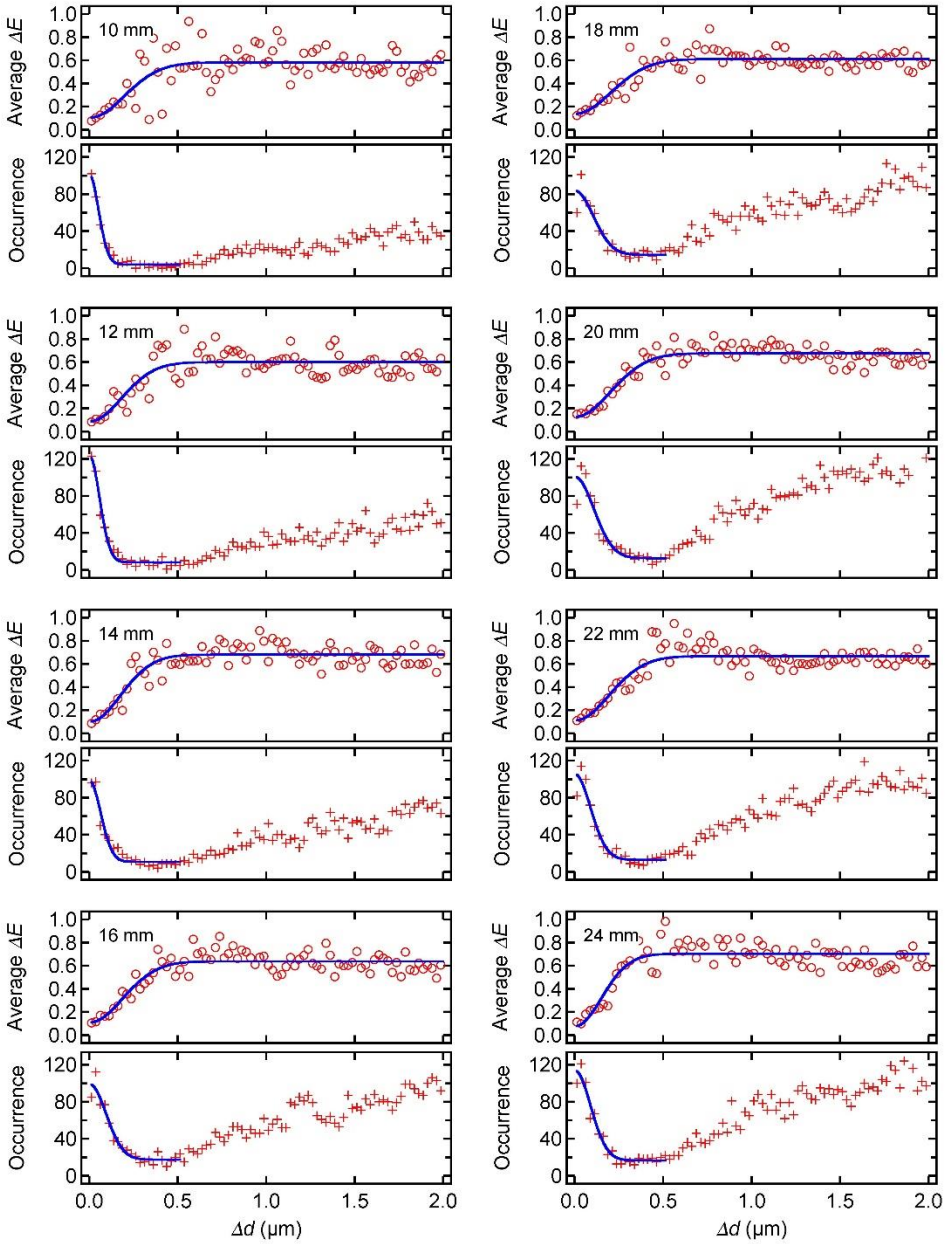

Figure A.3. In pairs: difference in E (ΔE) between pairs of fluorescent spots and number of measurements as a function of their distance from each other, along the full gradient length. The large population near $\Delta d = 0$ is due to blinking of immobile single molecules. These results reveal a correlation in E values over distances of less than ~ 200 nm.